RICE UNIVERSITY

Optical, Electrical and Thermal Properties of Plasmonic Nanojunctions and Carbon Nanotube Fibers

Shusen Liao

A THESIS SUBMITTED
IN PARTIAL FULFILLMENT OF THE
REQUIREMENTS FOR THE DEGREE

Doctor of Philosophy

APPROVED, THESIS COMMITTEE

Douglas Natelson, Chair
Professor of Physics and Astronomy

Peter Nordlander
Professor of Physics and Astronomy

Geoff Wehmeyer
Assistant Professor of Mechanical Engineering

HOUSTON, TEXAS
July 2025

ABSTRACT

Optical, Electrical and Thermal Properties of Plasmonic Nanojunctions and Carbon Nanotube Fibers

by

Shusen Liao

Plasmonic nanowires and nanojunctions with sub-nanometer gaps can be fabricated on chip in large scale and have exhibited potentials in applications in high sensitivity spectroscopy, single molecule, photoelectric and thermoelectric devices, and nanoscale light source in recent years. This thesis reviews the plasmonic behavior in plasmonic nanowires and nanojunctions and focuses on surface enhanced Raman spectroscopy (SERS) by remote excitation and nanojunction electroluminescence (EL) in magnetic field. Another project about probing the variation in the Seebeck coefficient in carbon nanotube fibers (CNTFs) using the photothermoelectric (PTE) effect is also discussed.

In Chapter 1, I will introduce some basic concepts including plasmons, Raman spectroscopy, thermoelectric effects and carbon nanotubes (CNTs). In Chapter 2, I will focus on the plasmonic and thermoelectric behaviors of metallic nanowire and nanojunction systems, including photothermoelectric effect, plasmonic heating, SERS, open circuit photovoltage (OCPV) and EL.

In Chapter 3, I will discuss the remote excitation SERS in plasmonic molecular junctions. Surface plasmon polaritons (SPPs) are excited at nearby gratings,

propagate to the junction, and couple to the local nanogap plasmon modes. Like direct excitation, remote excitation of the nanogap can generate both SERS emission and OCPV. We compare the SERS intensity and the OCPV in both direct and remote illumination configurations. SERS spectra obtained by remote excitation are much more stable than those obtained through direct excitation when the photon count rates are comparable. By statistical analysis of 33 devices, the coupling efficiency of remote excitation is calculated to be around 10%, consistent with the simulated energy flow.

In Chapter 4, I will discuss the large magnetic field dependent electroluminescence in nonmagnetic plasmonic nanojunctions. We experimentally find that EL spectra of planar nonmagnetic plasmonic nanojunctions are quite sensitive to an external magnetic field, with changes in total emission at specific wavelengths up to tens of percent under the external magnetic field of a few Tesla, exceeding simple classical expectations by more than two orders of magnitude. The linear and circular polarization analysis of the emitted spectra shows profound changes that are asymmetric with external field direction. The dramatic changes in polarized spectra under external field indicates that the LSPRs can be modified by the external field. The inferred plasmonic DOS and effective temperatures of hot carrier under different external magnetic field are different, which further indicates the magnetic field dependent LSPRs. A quantum-corrected model (QCM) simulation is performed to compare with the experimental results.

In chapter 5, we develop a method to probe the variation of the Seebeck coefficient along CNTFs using the PTE effect. The photovoltage is measured as a function of position, and the laser induced temperature profile is obtained by a robust steady state thermal model. The Seebeck coefficient as a function of position along the fiber can be obtained from the measured, spatially mapped photovoltage and the temperature profile. We observe a correlation between the variation of the Seebeck coefficient and the shift of Raman modes, both related to the doping level and Fermi energy. We find the Seebeck coefficient fluctuation in the pristine fiber is due to the non-uniformity of the doping level and the Fermi energy. With an established model to correlate the thermoelectric response and the Fermi energy, our PTE-based method can probe the Fermi energy fluctuation along the fiber with the resolution better than 1 meV, which is far beyond the capability of the commercial Raman spectroscopy. This study shows a non-destructive method to quantify the uniformity of CNTFs at the micrometer scale, key for fabricating more uniform and higher quality CNTFs and generalizable to other conducting fiber systems.

In Chapter 6, we will discuss possible follow-up research based on these projects. The details of the optical measurement setups in Natelson lab are introduced in Appendices.

Acknowledgments

First, I would like to thank my advisor, Prof. Douglas Natelson. He provides me valuable guidance during the past years. His advice and encouragement not only help me in research, but also support me in daily life. I also thank Prof. Peter Nordlander and Prof. Geoff Wehmeyer for joining my defense committee and provide insightful comments and suggestions.

I would like to thank all collaborators for the projects. Without them, the thesis cannot be finished. First, I want to thank Qian Ye and Dr. Keith Sanders and Prof. Alessandro Alabastri for their hard work and wonderful simulation results for the remote excitation Raman project. I also thank Dr. Yingru Song, Dr. Lauren W. Taylor, Dr. Oliver S. Dewey, Shengjie Yu, Prof. Matteo Pasquali, Prof. Junichiro Kono and Prof. Geoff Wehmeyer for the device fabrication, modeling and supporting measurements for the CNT related project. Finally, I thank Jaime Abad Arredondo, Prof. Antonio Isaac Fernandez Dominguez and Prof. Francisco J. Garcia-Vidal for the modeling and simulation for the magnetic field dependent plasmonic light emission project.

I want to thank Yunxuan Zhu for teaching me device fabrication, measurement setup, data analysis hand by hand. I also want to thank Dr. Jiawei Yang, Dr. Liyang Chen, Renjie Luo, Dr. Dale Lowder, Tanner Legvold, Ken Ssennyimba, Kexin Xie, Yuxin Wan, Gage Eichman and Dr. Mahdiyeh Abbasi for their help in the lab. I want to thank Welch Foundation, Carbon Hub, NSF for the funding supports. I want to thank applied physics program for giving me the chance to study, do research and live at Rice university.

At last, I'd like to thank my family for their support from thousands of miles away in China and my friends in Houston. It would be much easier to overcome the difficulties in life and research with their help.

Contents

List of Figures

Chapter 1

Introduction

In this chapter, I will introduce the structure of the thesis and have an introduction and brief discussion about background and basic knowledge and concepts related to the following chapters to help the readers have a better understanding. **There can be some further revision of this thesis based on the new progress of the project discussed in chapter 4. The newest version of the thesis will be uploaded at https://natelson.rice.edu/team.html**

1.1. Structure of the thesis

In chapter 1, I will discuss the background and basic knowledge and concepts related to the following chapters. In chapter 2, I will introduce plasmonic and thermoelectric properties in metallic nanowire and nanojunction system, which is

helpful to understand the following chapters. In chapter 3, 4 and 5, I will discuss in detail about three individual research projects including experiment setup, device fabrication, measured data, data analysis and modeling. In chapter 6, I will summarize the thesis and discuss the potential future projects. In the appendix, I will describe more details for these projects and experimental optical setups in Natelson's lab.

1.2. Plasmon

Plasmons are the collective oscillations of free electrons with respect to the positive ions in a metal. The oscillations can be driven by external time-varying electromagnetic field, such as light and electron beams. In the free electron model, the bulk plasmon frequency ω_b can be estimated as[1]:

$$\omega_b = \sqrt{\frac{ne^2}{m\epsilon_0}} \quad (1-1)$$

where n is the conduction electron density; e is the electron charge; m is the electron mass; ϵ_0 is permittivity of free space. When the frequency of the external field matches the plasmon frequency, plasmon resonances occurs. At this resonance condition, plasmons are strongly excited, leading to enhanced absorption and scattering of electromagnetic energy by the metal. In this thesis, we focus on the plasmons at nanoscale, especially I will introduce localized surface plasmons (LSPs) and surface plasmon polaritons (SPP) supported by metallic nanostructures. Ref.[1] discusses the fundamental concepts, physics, properties, and application of

plasmonics including LSPs and SPPs in great detail, which can be very helpful for the readers of the thesis.

1.2.1. Localized surface plasmons (LSPs)

When the size of metal is comparable to or smaller than the wavelength of the excitation light, the plasmons are confined in nanoscale. A Schematic of the LSPs is shown in Figure 1-1A. Different from bulk metals, the plasmon resonance frequency depends on the size, shape, and dielectric environment of the nanostructure.[2,3] One important effect of the LSPs is the giant electric field enhancement near the surface of the nanostructure compared to the field of the incident radiation, as shown in Figure 1-1B. One important application of the enhanced electric field is surface enhanced Raman spectroscopy, which will be discussed in detail latter.

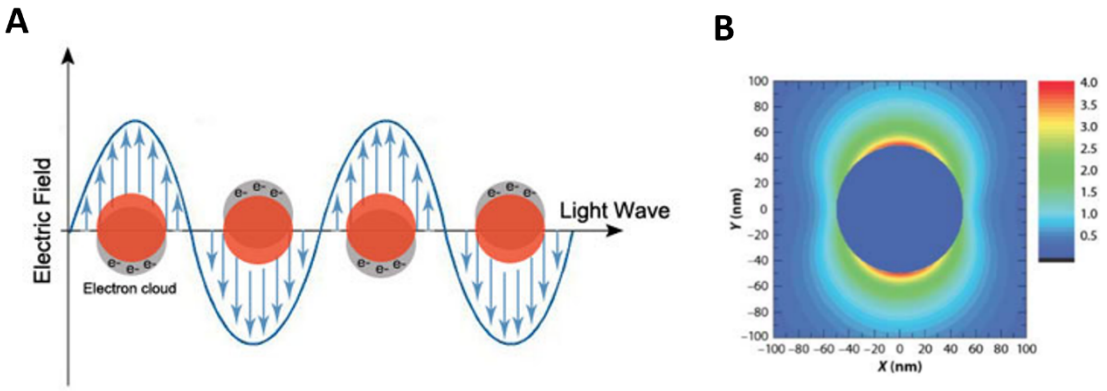

Figure 1-1: (A)[4] LSP and (B)[5] Electric field enhancement around a sphere nanoparticle

Bright modes and dark modes: in complicated plasmonic nanostructures, such as coupled nanoparticles, and asymmetric geometries, the LSPs can be usually categorized into bright modes and dark modes.[6–10] Bright modes are modes that strongly couple to light, so they can absorb and scatter electromagnetic radiation efficiently. In other words, they can radiate energy into the far-field. Usually, the dipole-like oscillations are bright modes. Dark modes are modes that have weak or no direct coupling to far-field radiation. As a result, the dark modes are non-radiative or weakly radiative. Dark modes can be excited by symmetry breaking, near-field excitation and electron beam excitation.[1,6,10–14] They are also usually higher-order multipoles, out of phase oscillations or hybridized modes.[1,15] An example of bright mode and dark mode is shown in Figure 1-2.

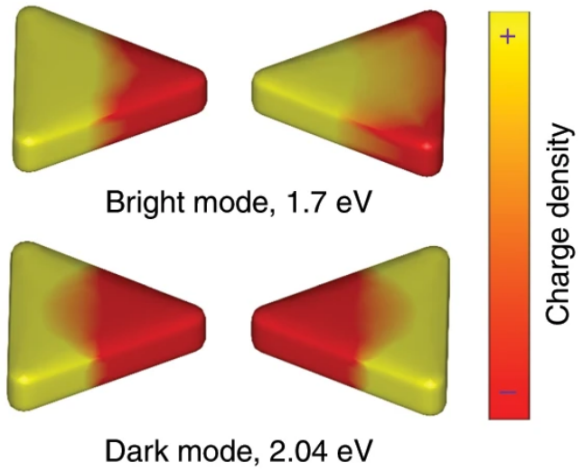

Figure 1-2:[14] An example of bright and dark plasmon modes in a dimer system.

Plasmon hybridization: plasmon response in metallic nanostructures can be viewed as the collection of plasmons arising from simpler geometries to form an interacting system.[15] LSPs in the complex system are determined by the electromagnetic interaction between modes of the simpler geometries. This is called plasmon hybridization.[15] The result is a splitting into a bonding (lower energy) and an antibonding (higher energy) plasmon mode. The bonding modes are often bright and the antibonding modes are often dark. The idea of plasmon hybridization is similar to how atomic orbitals mix to form bonding and antibonding molecular orbitals. Figure 1-3 shows an example of the plasmon hybridization between a sphere and a cavity to form a nanoshell.

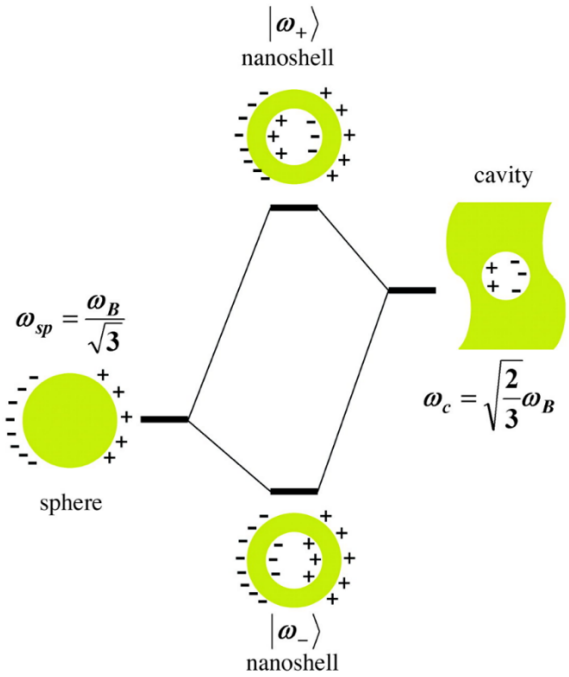

Figure 1-3:[15] An example of plasmon hybridization.

LSP excitation and relaxation and hot carrier dynamics: the review article Ref.[16] discusses the LSP excitation and relaxation dynamics in detail. Figure 1-4 illustrates the process of the LSP excitation and relaxation in a metallic nanoparticle:[16] at time $t = 0s$, LSPs are excited by the incident light, and the excited LSPs redirect the Poynting vector of the light towards to the nanoparticle (Figure 1-4a). This produces an antenna effect resulting in light collection from an area that is larger than its physical size.[16–18] In the first 1-100 fs, LSPs can be damped radiatively via emission of photons, or non-radiatively via Landau damping.[19] The ratio between the two decay mechanism is determined by whether the plasmon modes are bright or dark.[16,20] During the Landau damping process, the plasmons are transferred into electron-hole pairs (Figure 1-4b). The distribution of the carriers depends on the plasmon energy, the particle size, the symmetry of the plasmon modes, and the electronic structure and electronic density of states of the material.[16,21] In $t = 100fs - 1ps$, the carriers form a Fermi-Dirac like distribution with a large effective electron temperature T_{eff} by electron-electron scattering (Figure 1-4c).[16,22,23] Ref.[21] introduces $N_e(\varepsilon)$ as the number of hot electrons generated per each plasmon excited in the system that have an energy (measured with respect to the Fermi level) larger than a certain threshold ε. It can be written as:

$$N_e(\varepsilon) = \hbar\omega_p \sum_{\varepsilon_f \geq \varepsilon} \Gamma_e(\varepsilon_f, \omega_p)/P_{absorb} \quad (1-2)$$

where ω_p is the plasmon frequency; $\Gamma_e(\varepsilon_f, \omega_p)$ is the probability per unit time of exciting a hot electron in state f, which can be calculated using the Fermi's golden rule. Plasmon induced hot carriers have wide application in photocatalysis[24–27] and photovoltaic devices.[28–32] In $t = 100ps - 10ns$, the energy of the hot carriers is transferred to the lattice and the surroundings through electron-phonon and phonon-phonon interactions (Figure 1-4d). The hot electron-hole pairs can also recombine and emit photons with broad energy range.[33]

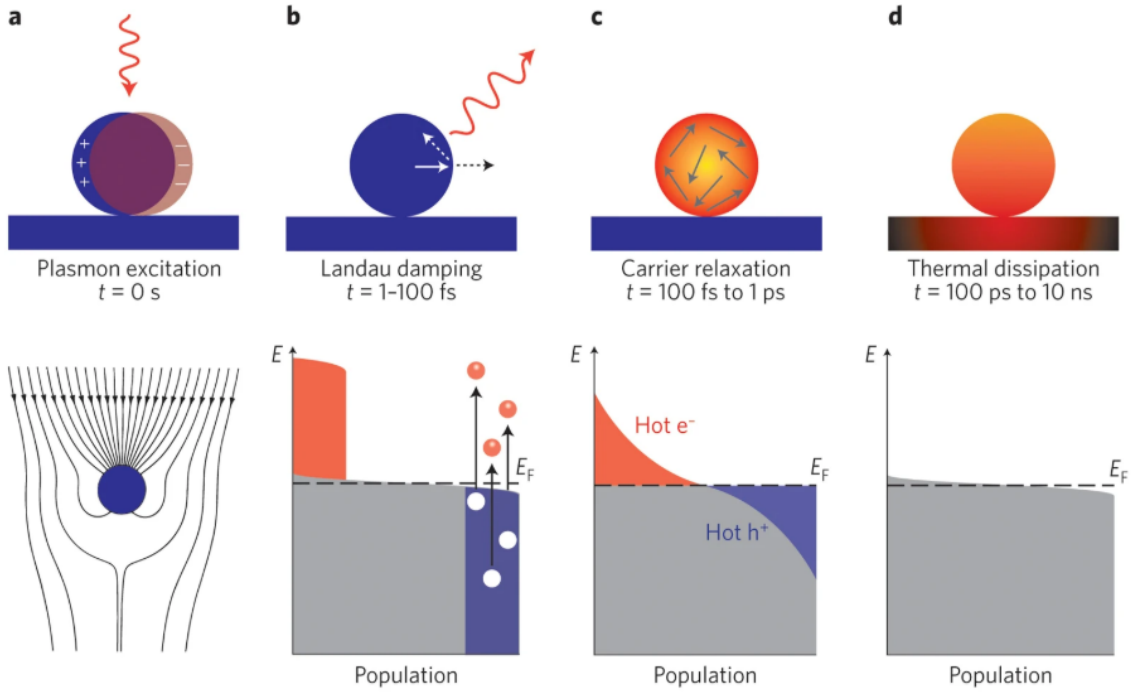

Figure 1-4:[16] **Schematic of plasmon excitation (a), damping (b) and hot carrier dynamics (b-d) in a metallic nanoparticle.**

1.2.1. Surface plasmon polaritons (SPPs)

Unlike LSPs, surface plasmon polaritons (SPPs) are electromagnetic waves that travel along a metal-dielectric interface, as shown in Figure 1-5. SPPs have shorter wavelength than the light in vacuum at the same frequency, so SPPs have a larger momentum and local field intensity.[1] Hence SPPs have potential applications in subwavelength optics,[34–37] and near-field optics.[38,39] The wave vector of the SPP excitation k_{SPP} can be expressed by:[1]

$$k_{SPP} = \frac{\omega}{c}\sqrt{\frac{\varepsilon_m \varepsilon_d}{\varepsilon_m + \varepsilon_d}} \quad (1-3)$$

where ω is the angular frequency; c is the speed of light in vacuum; ε_m and ε_d are relative permittivity of the metal and dielectric.

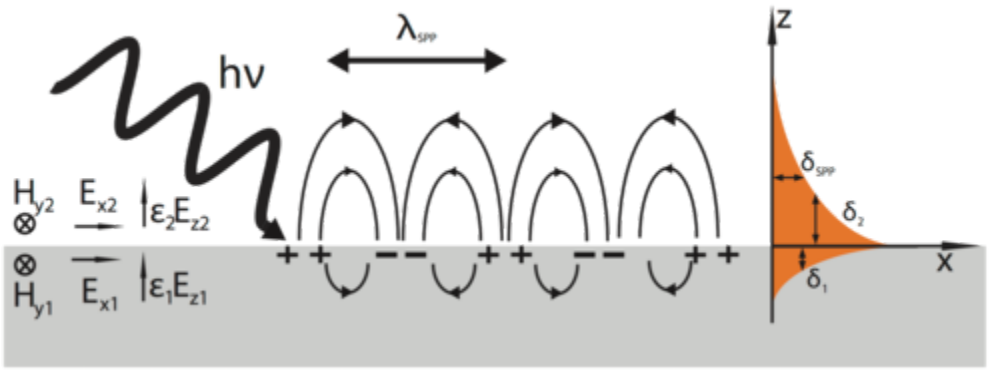

Figure 1-5:[40] Schematic of SPPs at the metal-dielectric interface.

SPPs can be excited both electrically and optically. For electrical excitation, high energy electrons are injected into the metal, and the component of the scattering

vector parallel to the surface results in the formation of SPPs.[41,42] Optical excitation is more widely used in experiments, including prism coupling,[37,43,44] grating coupling,[37,43,44] and fiber and waveguide coupling.[37,45–47] Since the mismatch of the momentum of the free-space photon and the same frequency SPPs, the free-space light cannot directly couple with an SPP.[1] Prisms and gratings can be used to match the wave vectors. In prism coupling, a prism can be place against (Kretschmann configuration, Figure 1-6a) or very close (Otto configuration, Figure 1-6c) the metal. The light passes through the metal in Kretschmann configuration to excite SPPs, and in the Otto configuration, it is the evanescent field that tunnel across the gap to excite SPPs. The parallel wave vector k_x can be written as:

$$k_x = \frac{\omega}{c} n_{prism} \sin(\theta_{sp}) \quad (1-4)$$

where n_{prism} is the refractive index of the prism, and θ_{sp} is the incidence angle. To match the wave vectors, $k_x = k_{SPP}$ is needed.[1] SPPs can also be generated by grating coupling (Figure 1-6e), where gratings are used to match the wave vectors:[1,43,44]

$$k_{SPP} = k_0 \sin(\theta_{sp}) + n\frac{2\pi}{\Lambda} \quad (1-5)$$

where k_0 is the free-space wavevector; n is the diffraction order; Λ is the grating period. SPPs can be also excited using Kretschmann configuration-like waveguides[37,45] (Figure 1-6b), scanning near-field optical microscope[37,48,49] (SNOM, Figure 1-6d) and surface features[37,50] (Figure 1-6f).

SPPs can lose energy due to absorption and scattering during their propagation along the metal surface. The imaginary part of the wave vector k_x'' can be introduced to describe the energy loss:[51]

$$k_x'' = \frac{\omega}{c}\left(\frac{\varepsilon_m'\varepsilon_d}{\varepsilon_m' + \varepsilon_d}\right)^{3/2}\frac{\varepsilon_m''}{2{\varepsilon_m'}^2} \quad (1-6)$$

where ε_m' and ε_m'' are real and imaginary parts of the dielectric function of the metal. The intensity decreases by a factor of exp $(-2k_x''x)$ when the SPP propagates the distance x. The propagation length L_{spp} which is defined as the distance for the SPP intensity to decay by a factor of 1/e can be expressed as:[1]

$$L_{spp} = \frac{1}{2k_x''} \quad (1-7)$$

similarly, the penetration depth z_i of the SPP electric field into the metal or the dielectric can be written as:[1]

$$z_i = \frac{\lambda}{2\pi}\sqrt{\frac{|\varepsilon_m'| + \varepsilon_d}{\varepsilon_i^2}} \quad (1-8)$$

where λ is the wavelength of the photon in free-space. i can be the dielectric or the metal. The penetration depth in the metal is usually much smaller than that in the dielectric, considering the value of ε_d and ε_m.

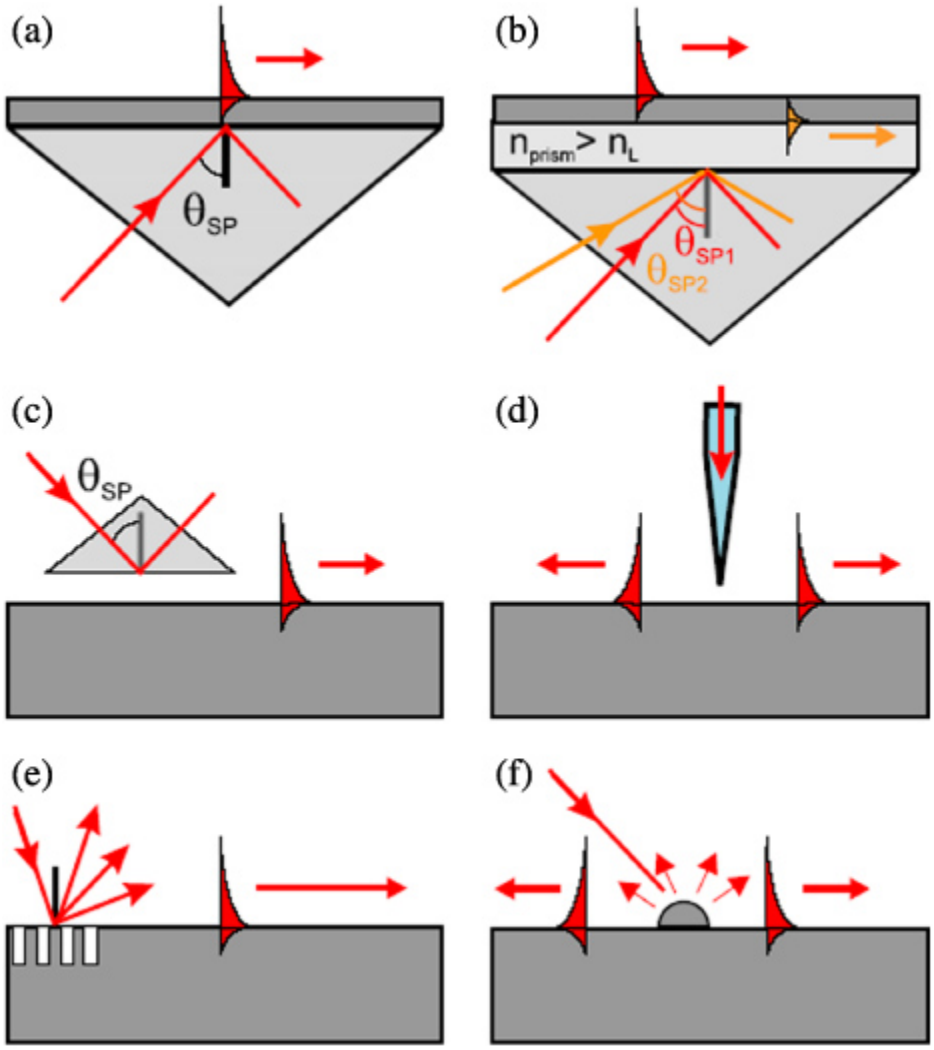

Figure 1-6:[37]A summary of optical excitation of SPPs: (a) Kretschmann configuration. (b) Two-layer Kretschmann configuration (waveguide). (c) Otto configuration. (d) SPP Excitation with an SNOM probe. (e) Diffraction on a grating and (f) Diffraction on surface features.

1.3. Raman spectroscopy and surface enhanced Raman spectroscopy (SERS)

Raman scattering is the inelastic scattering of light by matter and was first discovered by the Indian physicist C. V. Raman and his student K. S. Krishnan.[52] The scheme of Raman scattering is shown in Figure 1-7. In Raman scattering, the incoming light can interact with molecular motions (vibrations, rotations) that alter the polarizability tensor of the molecule. The incident photon can either gain or lose energy in the interaction. When the photon energy decreases in the interaction, it is called Stokes scattering; when the photon energy increases, it is called Anti- Stokes scattering; when the interaction is elastic scattering and the photon energy remains the same, it is called Rayleigh scattering. The Raman scattering cross section is usually small, so the intensity of Stokes and Anti-Stokes scattering is much smaller than Rayleigh scattering. According to the photon energy shift, Raman scattering can be used to determine the vibrational modes of the molecules, as described in the following equation:

$$\Delta\nu = \left(\frac{1}{\lambda_{in}} - \frac{1}{\lambda_{sc}}\right) \quad (1-9)$$

where $\Delta\nu$ is the Raman shift in wavenumber, λ_{in} is the wavelength of incoming excitation light, and λ_{sc} is the wavelength of the scattering light. The energy scale of Raman scattering is usually in meV, with the fact that 8000 cm^{-1}~1 eV. Raman spectroscopy provides a fingerprint of molecule systems and Raman spectroscopy is

a powerful tool for molecule identification in chemistry, biology and other related fields.[53–58] However, the intensity of Raman spectroscopy can be low, especially when the number of the molecules is small due to the small scattering cross section. One solution to this problem is surface enhanced Raman spectroscopy (SERS). [59–62]

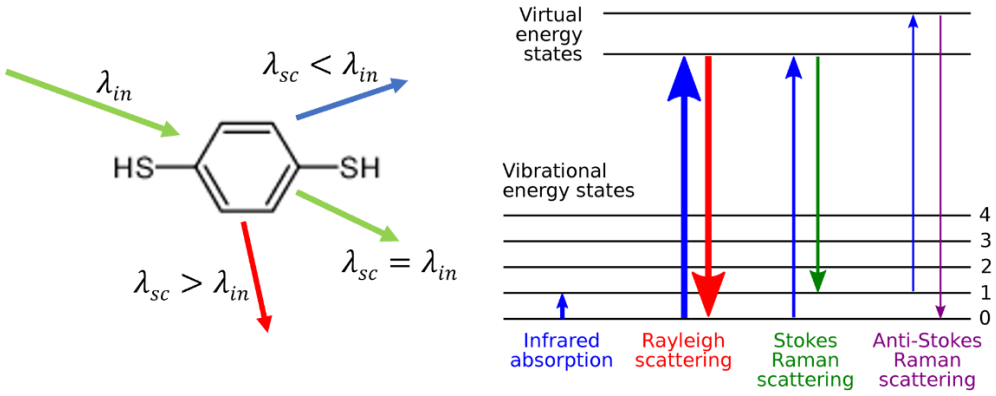

Figure 1-7:[63] Scheme of Raman scattering

SERS occurs when the molecules are adsorbed on rough metal surfaces and nanostructures. Electromagnetic theory can explain one major mechanism of SERS and is widely accepted: in classical view, Raman scattering can be considered as a molecule dipole $\boldsymbol{p}(\omega_R)$ oscillating at Raman frequency ω_R in the presence of an external electric field $\boldsymbol{E}(\omega_L)$ with the laser frequency ω_L:[64–67]

$$\boldsymbol{p}(\omega_R) = \hat{\alpha}_R(\omega_R, \omega_L)\, \boldsymbol{E}(\omega_L) \quad (1-10)$$

where $\hat{\alpha}_R(\omega_R, \omega_L)$ is the Raman polarizability tensor of the molecule. The radiated power P_{Raman} is: [64,65]

$$P_{Raman} = \frac{\omega_R^4}{12\pi\varepsilon_0 c^4}|\boldsymbol{p}(\omega_R)|^2 \propto |\boldsymbol{E}(\omega_L)|^2 \quad (1-11)$$

where ε_0 is the permittivity constant in vacuum, and c is the speed of light. The local intensity enhancement can be defined as:

$$M_{Loc}(\omega_L) = \frac{|E_{Loc}(\omega_L)|^2}{|E(\omega_L)|^2} \quad (1-12)$$

Besides the radiation enhanced by the local field, the radiation can be also influenced by re-radiation. The radiated light of the molecule can be back-scattered and influence the radiation.[66] Similarly, the re-radiation enhancement can be written as:

$$M_{Loc}(\omega_R) = \frac{|E_{Loc}(\omega_R)|^2}{|E(\omega_R)|^2} \quad (1-13)$$

Consider both the local field and re-radiation enhancements, the SERS power P_{SERS}^{Em} based on electromagnetic theory is:[65,66]

$$P_{SERS}^{Em} = M_{Loc}(\omega_L)M_{Loc}(\omega_R)P_{Raman} \quad (1-14)$$

We can define $G_{SERS}^{Em} = M_{Loc}(\omega_L)M_{Loc}(\omega_R)$ as the enhancement factor. Generally speaking, Raman mode energy is much smaller than the incident photon energy, so $\omega_L \approx \omega_R$ and $M_{Loc}(\omega_L) \approx M_{Loc}(\omega_R)$. Then the enhancement factor G_{SERS}^{Em} is approximately to be g^4 where $g = \frac{E_{Loc}(\omega_R)}{E(\omega_R)}$ is the electric field enhancement factor.

The electric field enhancement in SERS is caused by LSP resonances (LSPRs), as shown in Figure 1-1B. As discussed previously, the incident light can excite local surface plasmons with metallic nanostructures. When the plasmon frequency matches the light frequency, LSPRs can occur. As a result, hot spots where the local electric field E is dramatically enhanced are generated.

Additionally, chemical theory that is related with charge transfer and resonant Raman scattering can also contribute to SERS enhancement.[68–70] The chemical enhancement can be defined as:[64,65,71]

$$G_{SERS}^{Chem} = \frac{\sigma_k^{ads}}{\sigma_k^{free}} \quad (1-15)$$

σ_k^{ads} and σ_k^{free} are the Raman cross-sections of the k-th vibrational mode of the adsorbed and the free molecule. Figure 1-8 summarizes the mechanism of SERS.

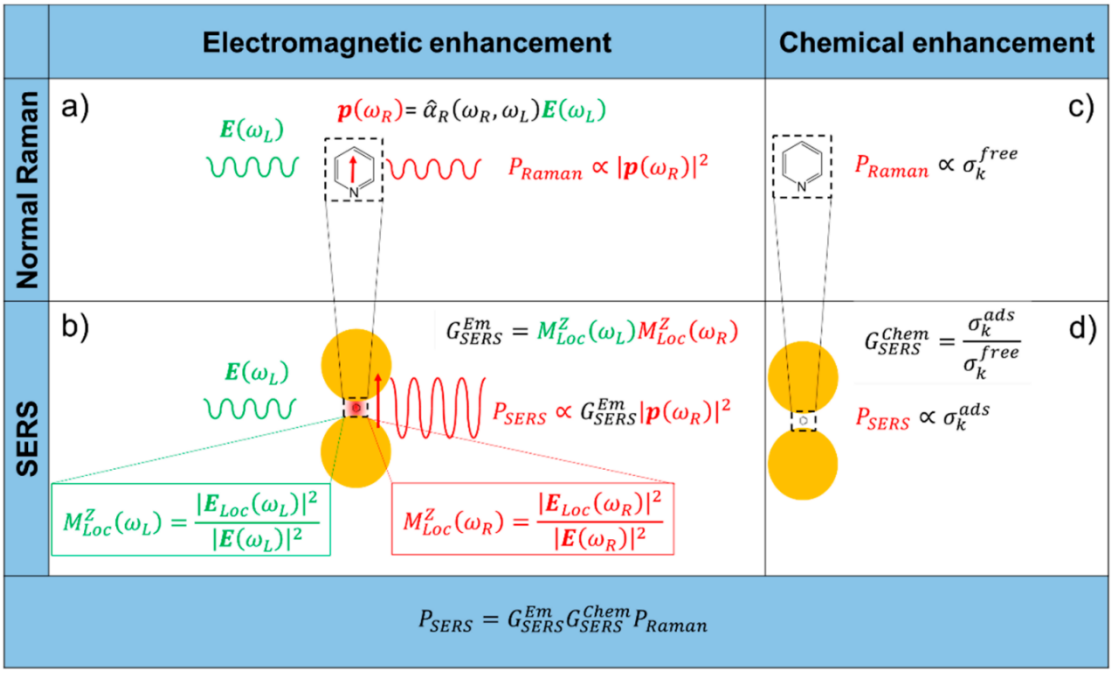

Figure 1-8:[64] **Summary of the mechanism of SERS in terms of electromagnetic and chemical theory.**

The steady state vibrational population of a particular Raman mode in terms of the vibrational effective temperature can be calculated by the ratio between Anti-Stokes and Stokes intensity:[72]

$$\frac{I_{AS}}{I_S} = \frac{\sigma_{AS} \cdot \rho_{AS}(\omega_{ph})}{\sigma_S \cdot \rho_S(\omega_{ph})} \cdot \frac{(\omega_0 + \omega_{ph})^3}{(\omega_0 - \omega_{ph})^3} \exp\left(-\frac{\hbar\omega_{ph}}{k_B T_{eff,vib}}\right) \quad (1-16)$$

where I_{AS} and I_S represent Anti-Stokes and Stokes intensity; ω_0 and ω_{ph} are the frequencies of laser and the Raman mode; σ_{AS} and σ_S are the Anti-Stokes and Stokes scattering cross sections; ρ_{AS} and ρ_S are the Raman enhancements due to LSPRs of

Anti-Stokes and Stokes modes; k_B is Boltzmann constant and $T_{eff,vib}$ is the vibrational effective temperature.

SERS has been reported in many plasmonically active metal nanostructure environments, for example, nanoparticles,[73] structured nanofilms[74] and the nanoscale tip in scanned probe microscopes.[75] In experiments, the SERS enhancement can exceed 10^{10}, which means it reaches the single molecule detection threshold.[76–78] Because of its high sensitivity, SERS is widely used for many chemical and biological applications,[60,79,80] such as in-situ monitoring of chemical reactions[81].

1.4. Thermoelectric effect

Thermoelectric effects are the direct conversion of temperature gradients to voltage and vice versa. Thermoelectricity arises due to the movement of charge carriers within a material as a result of a thermal gradient. Thermoelectric effects can be widely used for active cooling and energy harvesting.[82–84] Thermoelectric effects includes the Seebeck effect, the Peltier effect, and the Thomson effect.

1.4.1. Seebeck effect

The Seebeck effect, discovered by Thomas Johann Seebeck in 1821, describes the voltage generation caused by a temperature gradient. Illustrated in Figure 1-9, if there is a temperature gradient along a metal strip, the charge carriers (electrons) in the metal will move from the hot side to the cold side and form a diffusion current. In

the steady state, there should be no net current in the system, so there must be a voltage to counter the thermal diffusion of the electrons. The voltage V can be written as:

$$\nabla V = -S\nabla T \quad (1-17)$$

where S is the seebeck coefficient and ∇T is the temperature gradient.

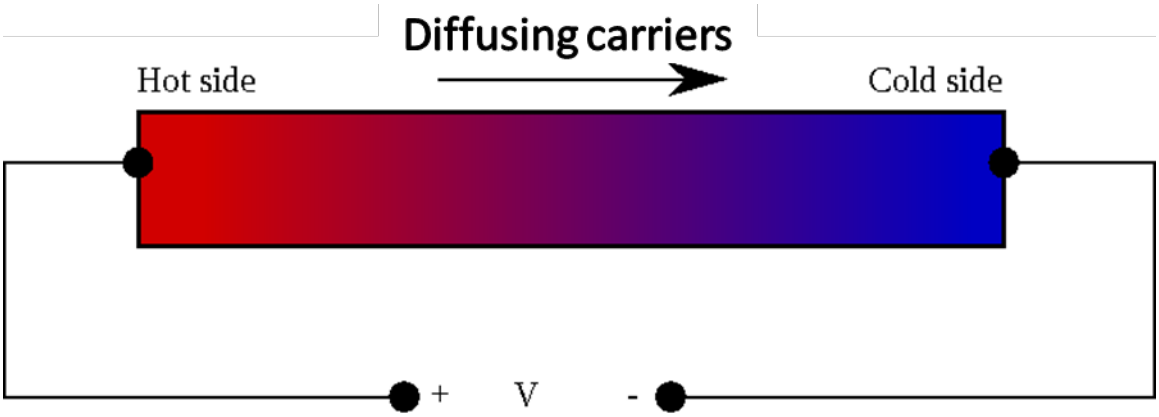

Figure 1-9: Schematic of the Seebeck effect.

The Seebeck coefficient depends on charge-carrier diffusion and phonon drag,[85] which can be tuned by temperature, geometry, impurities and the electronic structure of the materials. For metallic materials, the Seebeck coefficient S can be estimated using the Mott formula:[86]

$$S = -\frac{\pi^2}{3}\frac{{k_B}^2 T}{e}\frac{\partial ln\sigma(E)}{\partial E}\Big|_{E=E_F} \quad (1-18)$$

where k_B is the Boltzmann constant; e is the electron charge; T is the temperature; $\sigma(E)$ is the electronic conductivity as a function of the energy E and E_F is the Fermi energy. As the equation indicates, the Seebeck coefficient can be enhanced when there's a sharp feature in the DOS $N(E)$, such as the Van Hove singularity (VHS).[87]

1.4.2. Peltier effect

The Peltier effect, named after the physicist Jean Charles Athanase Peltier, can be understood as the complement of the Seebeck effect. When electric current passes through a material, heat can move in a certain direction, which creates a cool and a hot area at the two ends of the material, as shown in Figure 1-10. The Peltier heat generated per unit time $\dot{Q}$ can be calculated as:

$$\dot{Q} = \Pi I \quad (1-19)$$

where I is the electric current and Π is the Peltier coefficient of the material and it represent how much heat is carried per unit charge. The relationship between the Peltier coefficient Π and the Seebeck coefficient S is:

$$\Pi = ST \quad (1-20)$$

Figure 1-10: Schematic of the Peltier effect

1.4.3. Thomson Effect

The Thomson effect can be understood as a combination of the Seebeck and Peltier effects. It describes the heat exchange along a conductor with temperature gradient when electric current passes through it. The Thomson effect can account for the situation where the Seebeck coefficient depends on temperature in the Peltier effect. The heat production rate per unit volume $\dot{q}$ can be calculated as:

$$\dot{q} = -\mathrm{K}\vec{J} \cdot \nabla T \quad (1-21)$$

where $\vec{J}$ is the current density and K is the Thomson coefficient, which depends on temperature and the Seebeck coefficient change due to temperature gradient:

$$\mathrm{K} = T\frac{dS}{dT} \quad (1-22)$$

1.4.4. Thermoelectric figure of merit

The thermoelectric figure of merit ZT is a key parameter to evaluate the performance of a thermoelectric material. It quantifies the ability to convert heat into electrical energy. The thermoelectric figure of merit is defined as:[88]

$$ZT = \frac{S^2 \sigma T}{\kappa} \quad (1-23)$$

where σ is the electrical conductivity and κ is the thermal conductivity. $S^2\sigma$ is defined as the power factor (PF). High PF means that the material can generate large voltage and have high electrical conduction. However, due to the Wiedemann-Franz law, the thermal conductivity κ increases with increasing electrical conductivity σ, which counters the improvement of ZT. As a result, optimizing thermoelectric materials involves a balance between the electrical and thermal transport properties.[88]

1.5. Carbon Nanotubes

Carbon nanotube (CNT) systems are complicated, and the researches of them are comprehensive. A very detailed discussion of CNT systems is beyond the goal of the thesis. I will briefly introduce the basic concepts of CNTs and CNT fibers (CNTFs), which can be helpful to understand the research project in Chapter 5. A more comprehensive discussion of CNT can be found in our collaborator Dr. Natsumi

Komatsu's thesis Ref.[89], including structures, electrical, optical, thermal, thermoelectric properties of CNTs.

Carbon nanotubes (CNTs) are cylindrical nanostructures consisting of rolled-up sheets of graphene. CNTs can be synthesized by chemical vapor deposition (CVD) using hydrocarbon gases with catalyst.[90,91] CNTs have attracted great scientific interest due to their outstanding structural, electrical, thermal, and mechanical properties.[92–94] CNTs can be classified as single-wall carbon nanotubes (SWCNTs), double-wall carbon nanotubes (DWCNTs), and multi-wall carbon nanotubes (MWCNTs) based on the number of the graphene layers. The aspect ratio of CNTs is high, with a few nanometers in diameter and up to centimeters in length.[95,96] The crystal structure of the CNTs depends on how the graphene sheets are wrapped into the cylinder, which is defined as chirality.

Figure 1-11 shows the planer structure of a graphene sheet with lattice vector $\boldsymbol{a_1}$ and $\boldsymbol{a_2}$. $\boldsymbol{R}$ is the symmetry vector. For example, the graphene sheet can be wrapped into a CNT such that line OB and AB' overlap. In this case, OA describes the chiral vector $\boldsymbol{C_h}$ which can be defined as:

$$\boldsymbol{C_h} = n\boldsymbol{a_1} + m\boldsymbol{a_2} \equiv (n, m) \quad (1-24)$$

where n and m are integers and $n \geq m \geq 0$. OB describes the translation vector $\boldsymbol{T}$. Specifically, the CNTs with chirality (n, n) are called armchair nanotubes and the CNTs with chirality $(n, 0)$ are called zigzag nanotubes. The chiral angle θ is the angle between $\boldsymbol{C_h}$ and $\boldsymbol{a_1}$. It can be given by:[89]

$$\theta = cos^{-1}\left(\frac{\boldsymbol{C_h}\cdot\boldsymbol{a_1}}{|\boldsymbol{C_h}||\boldsymbol{a_1}|}\right) = cos^{-1}\left(\frac{2n+m}{2\sqrt{n^2+m^2+nm}}\right) \quad (1-25)$$

and the diameter of the CNT d_t is given by

$$d_t = \frac{|\boldsymbol{C_h}|}{\pi} = \frac{a_{C-C}}{\pi}\sqrt{3(n^2+m^2+nm)} \quad (1-26)$$

where $a_{C-C} \approx 1.44$ Å is the distance between the nearest carbon atoms.

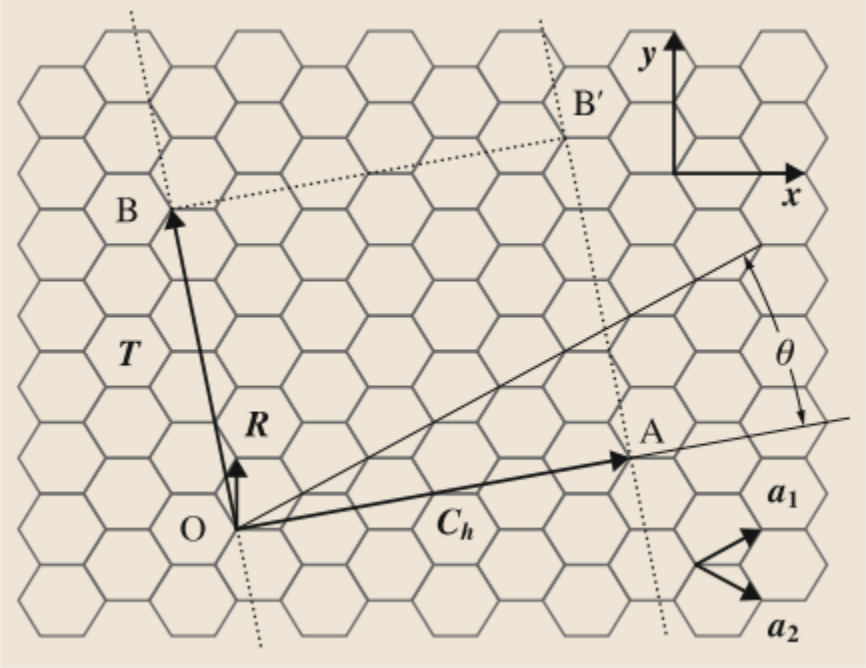

Figure 1-11:[97] **Schematic of a graphene layer used to explain the chirality of the CNTs.**

The properties of the SWCNTs are determined by the chirality. The diameter-dependent band gap of the SWCNTs can be calculated based on the chirality. Hence, the nanotubes can be classified to be metallic or semiconducting:[89,92,94,97] when $v \equiv$

$(n-m)\ mod\ 3 = 0$, the nanotube is metallic; when $v \equiv (n-m)\ mod\ 3 = 1\ or\ 2$, the nanotube is semiconducting. Specifically, metallic non-armchair tubes ($v = 0, n \neq m$) have small curvature-induced band gaps which is proportional to $1/{d_t}^2$.[98,99] An example of the band structure and DOS of the metallic and semiconducting SWCNTs is shown in Figure 1-12.

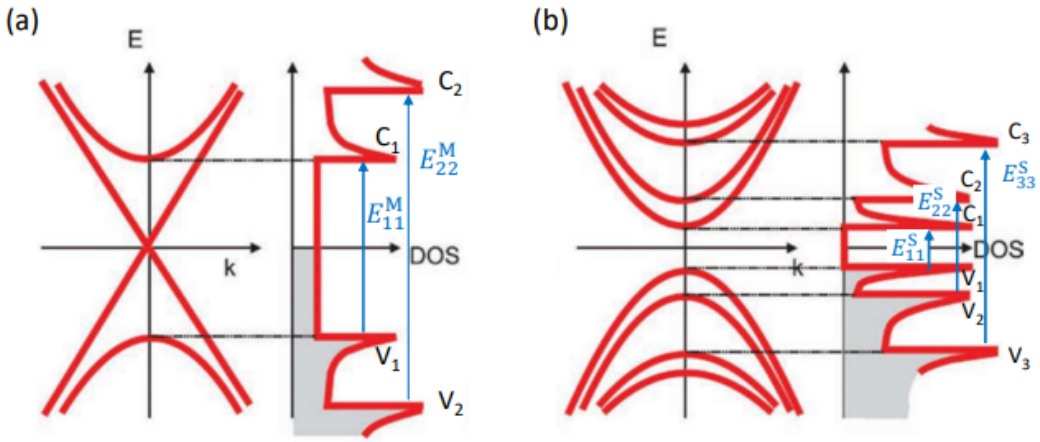

Figure 1-12:[89,100] **Band structure and DOS of (a) metallic SWCNTs and (b) semiconducting SWCNTs. V_i and C_j indicate the sub-bands in valence and conduction bands. The blue arrows indicate the optical transitions for parallel polarization.**

CNT fibers (CNTFs) are macroscopic fibers composed of many CNTs highly aligned together by Van de Waals force and mechanical compression. CNTFs can be assembled from individual CNTs by the spinning method.[91,101–103] CNTFs usually have the diameter of micrometer scale and the length can reach meters. CNTFs retain many of the remarkable properties of individual CNTs while being usable at macroscopic

scales. The applications of CNTFs are broad because of their flexibility, light weight, and outstanding thermal and electrical properties.[102–104] For example, they are promising candidates for thermoelectric active cooling materials thanks to their unique combinations of electrical and thermal properties.[105,106] CNTFs can be mechanically exfoliate into CNT bundles whose diameter can be tens of nanometers. Figure 1-13 shows the images of individual CNTs, CNT bundles and CNTFs.

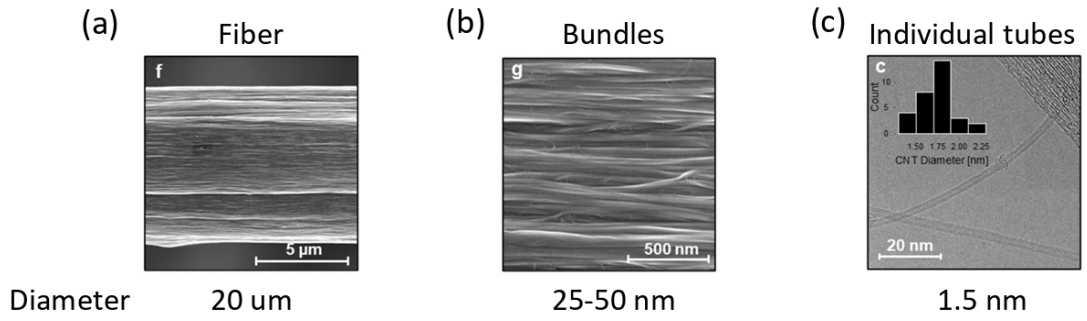

Figure 1-13:[89,107] **(a) Scanning electron microscope (SEM) image of a CNTF. (b) SEM image of CNT bundles. (c) Transmission electron image (TEM) of individual CNTs.**

Chapter 2

Plasmonic and Thermoelectric Related Phenomena in Metallic Nanowires and Nanojunctions

In this chapter, I will summarize the plasmonic and thermoelectric related phenomena in metallic nanowires and nanojunctions based on the previous works. They are helpful to understand the research projects in chapter 3, 4 and 5.

2.1. Photothermoelectric (PTE) effect in metallic nanowires

The PTE effect originates from the Seebeck effect: a focused laser beam can be used as a localized heat source to introduce the temperature gradient and as a result the Seebeck voltage. In quasi-one-dimensional (1D) systems with large aspect ratio, a laser beam is focused on the sample at location x_0 to induce a temperature gradient $\nabla T(x, x_0)$ at all axial locations x, and an open-circuit voltage is established as a result of the Seebeck effect. The voltage $V(x_0)$ can be written as

$$V(x_0) = -\int_0^L S(x)\nabla T(x, x_0)dx \quad (2-1)$$

where $S(x)$ is the position-dependent Seebeck coefficient and L is the sample length. If the sample is perfectly uniform (i.e. $S(x) = S_{ave}$, a position-independent average), then the voltage V is zero if the temperature is identical at $x = 0$ and $x = L$. Therefore, any detected voltage signal indicates non-uniformity of the system's Seebeck coefficient. By scanning the laser over the system, the photovoltage $V(x_0)$ as a function of the laser position x_0 can be obtained.

The PTE effect has been used to show the non-uniformity of the Seebeck coefficient in metallic nanowires caused by grain boundaries[108] and impurities.[109] The Seebeck coefficient along the single crystal gold nanowire is found to be correlated with the crystallographic defects and strain associated with misorientation (Figure 2-1a), detected by electron backscatter diffraction.[108] The Seebeck coefficient of a gold nanowire is also found correlated with the concentration of Pt impurities (Figure 2-1b).[109] We can also fabricate photodetectors based on the PTE effect of the structure where there are sharp features in the Seebeck coefficient. For example, photodetectors can be made with gold nanowires with asymmetric geometry (Figure 2-1c), as a result of the Seebeck coefficient changes with geometry at the nanoscale.[110]

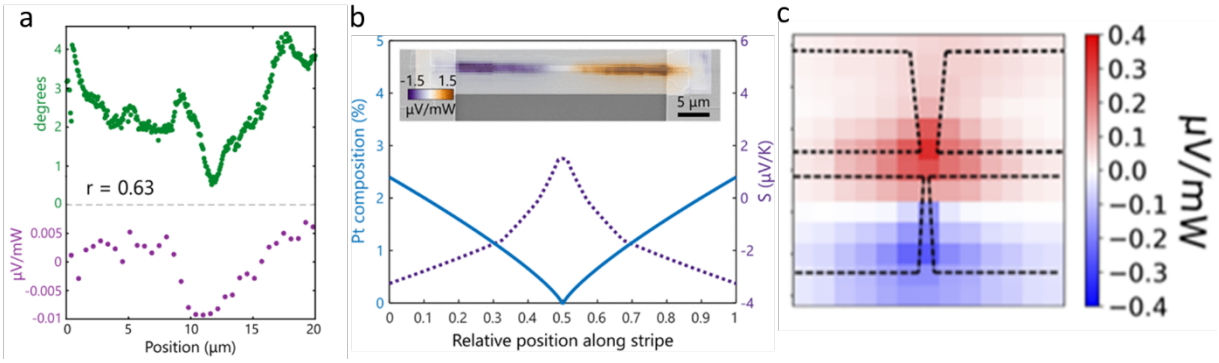

2.2. Plasmonic heating

When light is shining on the gold nanowire, the wire can absorb energy from the light and the temperature rises. When the polarization of the light is perpendicular to the nanowire ($\theta = 90^{\circ}$ in Figure 2-2a), the plasmon mode transverse to the nanowire can be excited, resulting in a larger absorption and larger temperature rise (Figure 2-2b) than the polarization along the nanowire ($\theta = 0^{\circ}$ in Figure 2-2a).[111] The similar polarization dependent heating behavior is also observed in TiN nanowires (Figure 2-2c).[112]

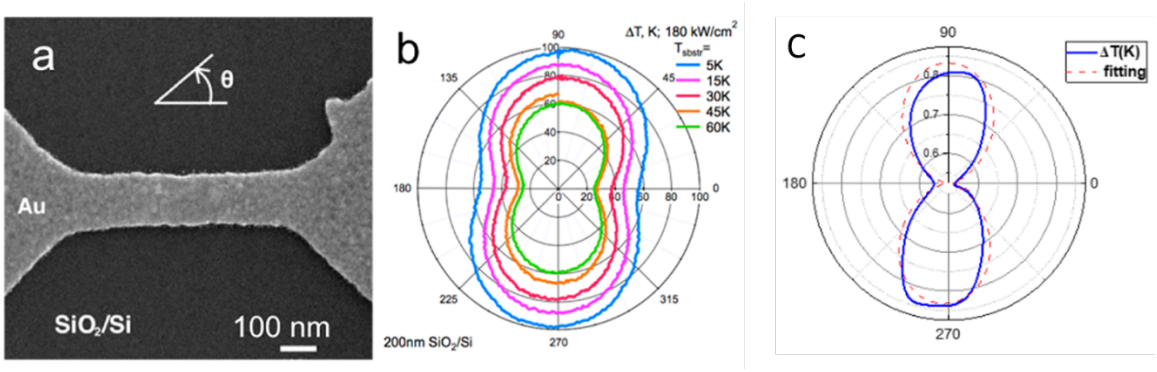

Figure 2-1: (a)[111] A SEM image of the gold nanowire on SiO_2/Si substrate. θ is the angle between the nanowire and the polarization of the light. (b)[111] Polar plot of the nanowire temperature as a function of θ with different substrate temperatures. (c)[112] Polar plot of the nanowire temperature as a function of θ in the TiN nanowire with substrate temperature to be 180K.

2.3. SERS in plasmonic nanojunctions

Planar gold nanowires can be electromigrated to form a nanogap,[113] and molecules can be deposited inside and around the gap to get a molecular junction. The details about the fabrication are discussed in Chapter 3. These junctions can be designed to have good plasmonic properties in near infrared region, can be fabricated on Si substrate in large scale and are reported to support SERS.[114,115] Localized gap plasmon modes can be excited by the incident light and the electric filed inside the gap can be greatly enhanced over the field of the incident radiation,[116] causing SERS signals from these hot spots. An example of a SERS spectrum in a plasmonic nanojunction is shown in Figure 2-3.

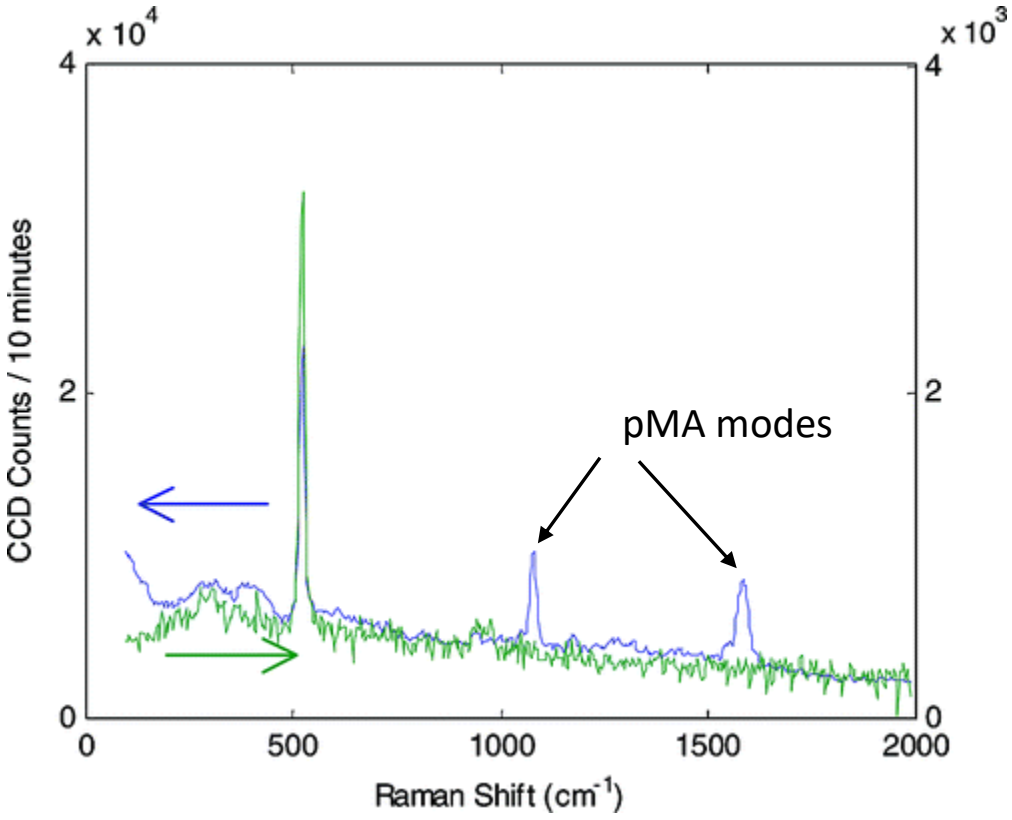

Figure 2-2:[115] **Blue curve (left scale): pMA SERS spectrum at hotspot center of one nanojunction densely covered by pMA, integrated for 10 min at incident power of 700 μW. Green curve (right scale): integrated signal under same conditions on middle of Au pad on the same nanojunction. The features near 520 and 960 cm^{-1} are from the Si substrate. No Raman features are detectable on either the Au pads or their edges under these conditions.**

2.4. Open circuit photovoltage (OCPV) in plasmonic nanojunctions

As we discussed in Chapter 1, LSPs can be excited optically in plasmonic systems including the nanojunctions. Due to the randomness of the shape of the nanogap after the electromigration process,[113] the geometry of the nanojunctions can be asymmetric across the gap. As a result, the plasmon modes and the hot carriers generated from the decay of the plasmon modes are asymmetric too. Then the hot electrons can tunnel from one side to another.[117] The tunneling current can be expressed using the Landauer theory:[118]

$$I_{hc} = \frac{2e}{h}\int (f_L(E) - f_R(E))T(E)dE \quad (2-2)$$

where $T(E)$ is the energy dependent transmission function; $f_L(E)$ and $f_R(E)$ are the electron distribution on the left and right electrode of the nanogap, respectively; h is the Planck constant.

Similar with the Seebeck effect, the net current of the system at the steady state should be 0, so a voltage must be generated to balance the optically driven tunneling electron current. Compared with the PTE effect, due to the resistance of the nanojunction device is much larger after the electromigration than the nanowire, the OCPV is much larger in the nanojunctions than the PTE voltage in nanowires (Figure 2-4a).[117]

The asymmetric plasmon mode excitation can be artificially introduced by designing the metals across the nanogap to have different plasmonic properties, including the width and the material.[119] The two sides can be designed to be Pt and Au with different widths. Au is more plasmonic active than Pt, so the hot electrons are generated more on the Au side. The electron tunneling direction is always from Au to Pt (Figure 2-4b). The hot carrier generation can be also tuned by the width of the nanowire.[119] In this way, we can engineer the direction of hot carrier tunneling in plasmonic tunneling structures.[119]

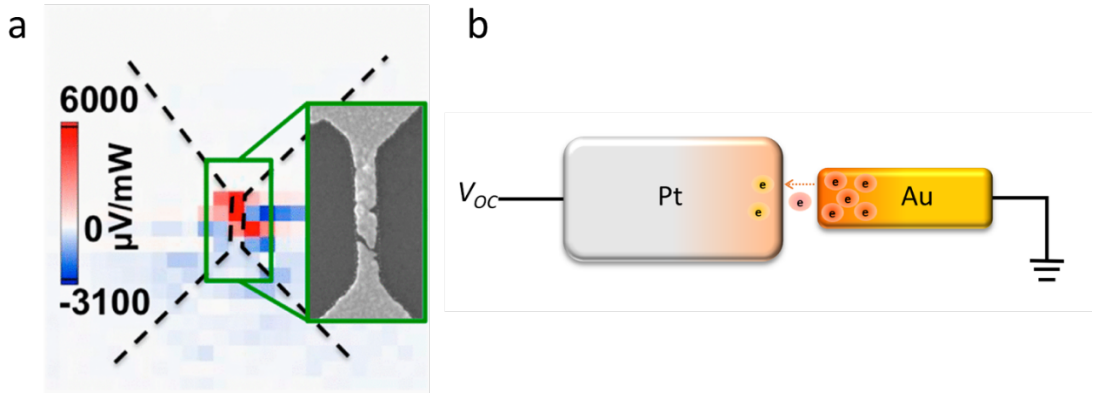

Figure 2-3: (a)[117] OCPV from the gold nanojunction. The inset shows the SEM image of the junction. (b)[119] Schematic of engineering of the direction of the electron tunneling. The hot electrons always tunnel from the Au side to the Pt side, because Au is more plasmonically active.

We also find that the OCPV can be enhanced using nanojunction devices made of single crystal (SC) gold than those made of polycrystal (PC) gold.[120] The enhancement can reach an order of magnitude. As illustrated in Figure 2-5, this enhancement is attributed mostly to the suppression of electron-phonon scattering and improved hot carrier tunneling efficiency in single-crystal devices:[120] the SC gold with defect-free nanostructures can suppress electron-phonon scattering and increase the mean free path of the hot carriers. The hot carrier lifetime in SC and PC gold nanoparticles are 3.1 ps and 1.6ps respectively based on previous report.[121]

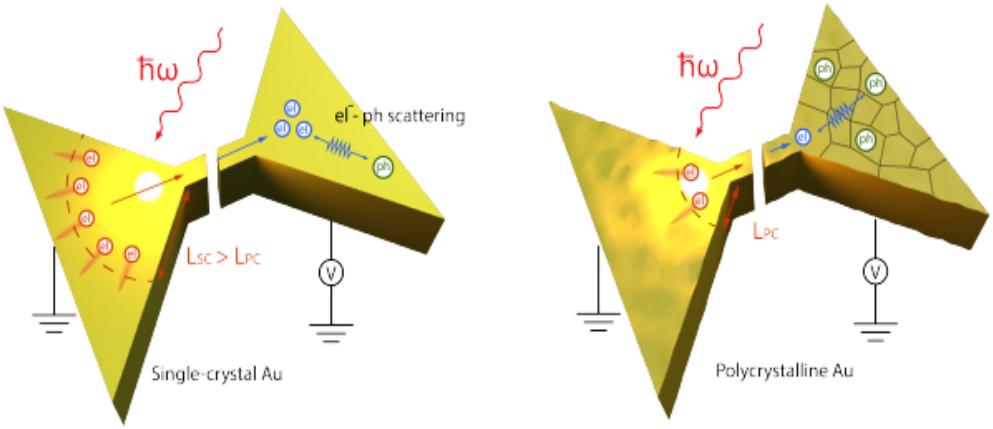

2.5. Electroluminescence (EL)

Light emission from electrically biased tunnel junctions was found in the 1970s by Lambe and McCarthy.[122] The mechanism is that the LSPR in the tunneling nanostructure can be excited inelastically by the tunneling electrons, and the LSPs can decay radiatively via far field photon emission. One feature of the light emission induced by the inelastic tunneling is the broad band spectrum with a limit that the

energy of the photons must be smaller than the energy of the electrons (i.e., $\hbar\omega \leq eV$, V is the bias voltage). This is known as below-threshold light emission. Recently, the above-threshold light emission (which means the photon energy can be higher than the electron energy ($\hbar\omega \geq eV$)) has been reported in scanning tunneling microscopy (STM) systems and nanofabricated tunnel junctions.[123–128] Several mechanisms, including the spontaneous blackbody thermal radiation model,[123,126] the coherent multi-electron interactions,[124,127] and the finite temperature effects,[129] are proposed to explain the above-threshold light emission. These mechanisms are discussed and compared in Ref.[130] and Dr. Yunxuan Zhu's thesis.[131] All these mechanisms cannot explain the phenomena we see in our planar plasmonic nanojunction system. Next, we will focus on the plasmonic hot carrier recombination mechanism which can explain the light emission in our system.

The above threshold light emission in the planar plasmonic nanojunctions is reported in Ref.[33]. The plasmonic hot carrier recombination mechanism gives the emission spectrum to be:[33]

$$U(\omega, V_b) \approx \rho(\omega) I^{\alpha} e^{-\hbar\omega/k_B T_{eff}} \quad (2-3)$$

where $U(\omega, V_b)$ is the photon count rate at frequency ω and at given voltage bias V_b; $\rho(\omega)$ is the plasmonic DOS as a function of ω; T_{eff} is the effective temperature of the hot carriers; I is the tunneling current, depending on the voltage bias V_b, and the value of $\alpha = 1.2$,[33] which can be obtained from the experimental results. This equation describes the light emission as a Boltzmann like thermal emission with an

effective temperature T_{eff} under the modification of the plasmonic DOS and the tunneling current. The spectra measured at different voltage bias are shown in Figure 2-6a. The shapes of the spectra are the same and a normalization process can be performed: each spectrum can be first divided by its I^{α} and then divided by the reference spectrum, which is the highest one in Figure 2-6a. Then log is taken for all the spectra, as shown in Figure 2-6b. It can be written as:

$$log\left(\frac{U_i\,(\omega, V_i)/I^{\alpha}}{U_{ref}\,(\omega, V_{ref})/I^{\alpha}}\right) = -\frac{\hbar\omega}{k_B}\left(\frac{1}{T_i} - \frac{1}{T_{ref}}\right) \quad (2-4)$$

where $U_i(\omega, V_i)$ and $U_{ref}(\omega, V_{ref})$ are the spectra of the spectrum i and the reference spectrum; T_i and T_{ref} are the effective temperature of spectrum i and the reference spectrum. The effective temperature T_{eff} is found to be linear in V_b:[33]

$$T_{eff} = \beta V_b \quad (2-5)$$

By the linear relationship and the normalization analysis, the T_{eff} for the spectrum at each bias can be obtained, as shown in Figure 2-6b. We can see that the hot-carrier distributions with high effective temperatures (above 2000 K) are achievable under modest electrical bias (~1 V). With the effective temperature for each spectrum, the plasmonic DOS $\rho(\omega)$ can be obtained (Figure 2-6c). We can see that the $\rho(\omega)$ of each bias voltage overlaps each other, indicating that the $\rho(\omega)$ is independent of the bias voltage and is only determined by the geometry of the nanojunctions and hence the excited plasmon modes. The mechanism of the can be summarized as (Figure 2-6d):[33] the LSPs excited by inelastic tunneling electrons undergo a nonradiative decay

process in which a plasmon energy quantum $\hbar\omega_{LSP}$ is transferred to an individual conduction hot electron–hole pair. The energy distribution of these hot carriers is centered around the Fermi level E_F, and extends to $E_F \pm eV$. If the rate of tunneling events outpaces carrier relaxation, a steady-state hot carrier distribution is sustained, with its specific form depending on the time interval between successive electron tunneling events and the hot carrier lifetimes (approximately hundreds of femtoseconds). The above-threshold light emission originates from the plasmon-enhanced radiative recombination of hot electrons and holes with high energies in the hot-carrier distribution. This above threshold light emission is material dependent. Statistically, for plasmonic-active material like gold, both the emitting photon counts and the effective temperature are larger at a given bias voltage than a plasmonic-poor material like palladium.[33]

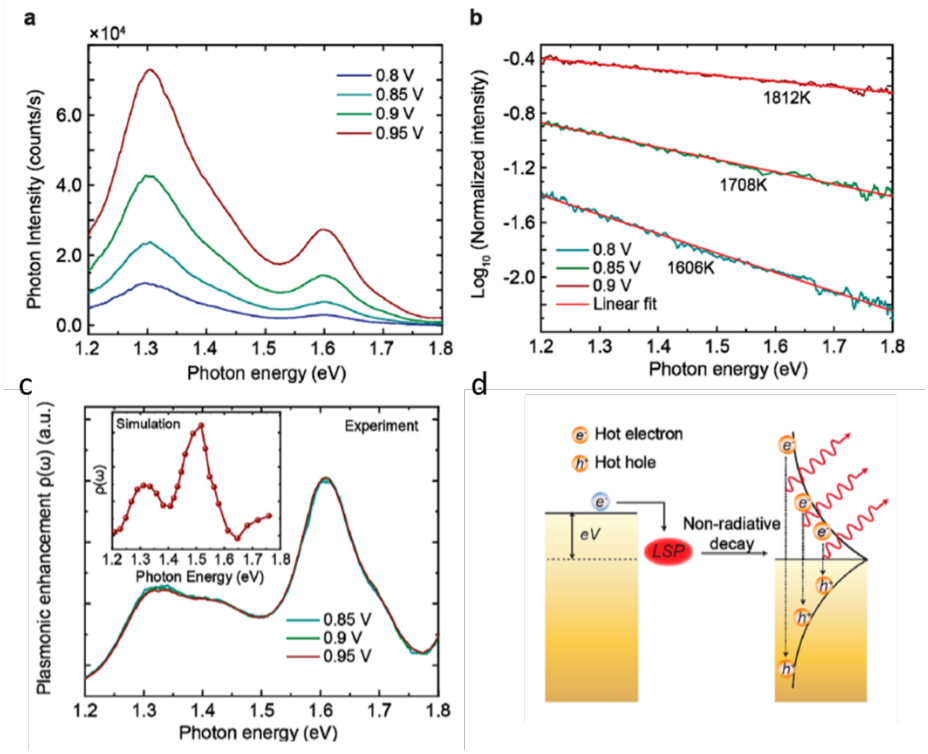

The plasmons can be also excited optically in these nanojunctions, and there is light emission called photoluminescence (PL). Ref.[132] finds that the light emission from the plasmonic nanojunctions can be greatly enhanced by a combination of optical and electrical excitation. The light emission in this case is called electro-photoluminescence (EPL, Figure 2-7a). As shown in Figure 2-7b, the enhancement ratio can reach more than 1000 and the ratio is larger at lower bias voltage. The mechanism of the enhancement is the higher effective temperature under optical and electrical excitation compared with electrical excitation only (Figure 2-7c).[132] The

effective temperature is even non-zero at 0 bias voltage in EPL due to the optical excitation, and the exponential Boltzmann term gives the great enhancement.

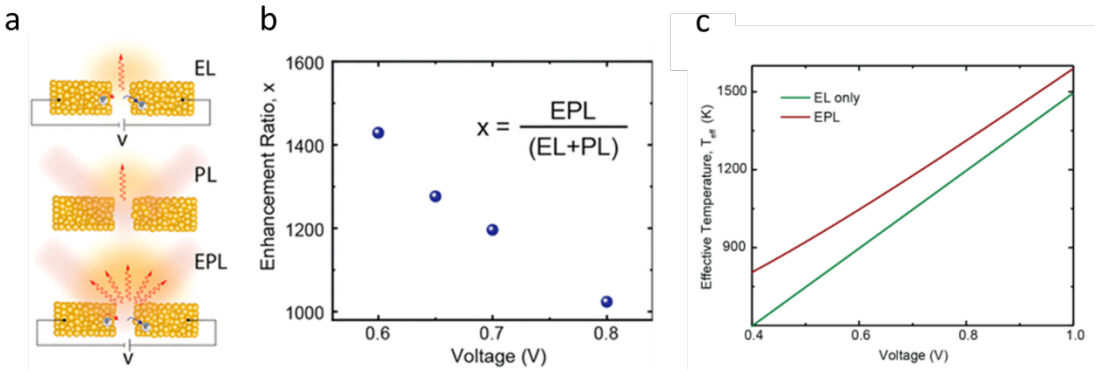

Figure 2-4:[132] **(a) Schematics of EL, PL and EPL. (b) Light emission enhancement ratio as a function of bias voltage. The enhancement can reach more than 1000. (c) The effective temperature of hot carriers in EL (green) and EPL (red) cases.**

The region of the EL can be controlled by multi-step electromigration in aluminum junctions.[133] The further electromigrated, the larger the nanogap is and the lower the conduction is, as illustrated in Figure 2-8. The EL in different regions can be summarized as:[133] in the high conductance region, the EL is dominated by the hot carrier mechanism and the above threshold light emission can be observed; in the intermediate region, the EL is dominated by the multi-electron mechanism: multi electrons can tunnel through the junction barrier coherently at a lower probability,

creating a higher-energy LSP and decaying in the same way to generate above-threshold emission; in the low conductance region, the EL can be well explained using the one-electron inelastic tunneling mechanism and the below threshold light emission can be observed.

EL is also reported to be a tool to probe plasmon–exciton coupling in hybrid structures consisting of a nanoscale plasmonic tunnel junction and few-layer two-dimensional transition-metal dichalcogenide transferred onto the junction.[134] The resulting hybrid states act as a novel dielectric environment that affects the radiative recombination of hot carriers and the local photonic DOS in the plasmonic nanostructure. The strong coupling between the plasmon and the exciton is observed with the Rabi splitting exceeding 50 meV (Figure 2-9).[134]

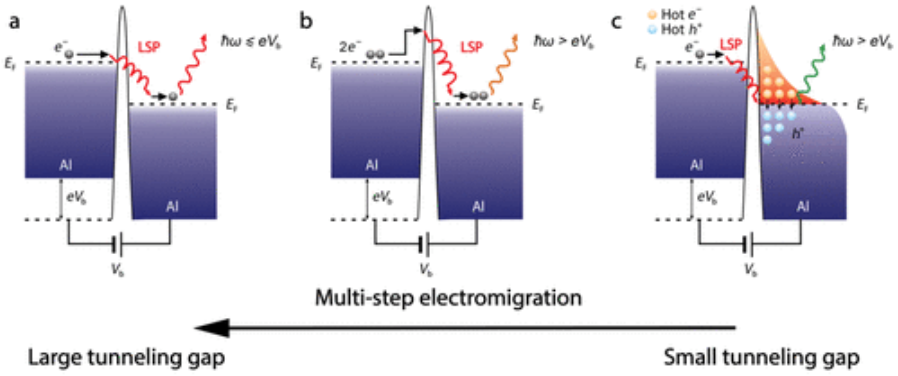

Figure 2-5:[133] **Schematics for various light emission mechanisms and the electromigration experimental setup. (a) An electron can inelastically tunnel from the source to the drain, exciting LSPs which subsequently decay into a radiative photon with energy limited by the LSPs. (b) Two electrons can tunnel through the junction barrier coherently at a lower probability, creating a higher-energy LSPs and decaying in the same way to generate above-threshold emission. (c) LSPs decay non-radiatively, exciting hot electrons and hot holes above and below the Fermi energy, which recombine radiatively to produce above-threshold photons.**

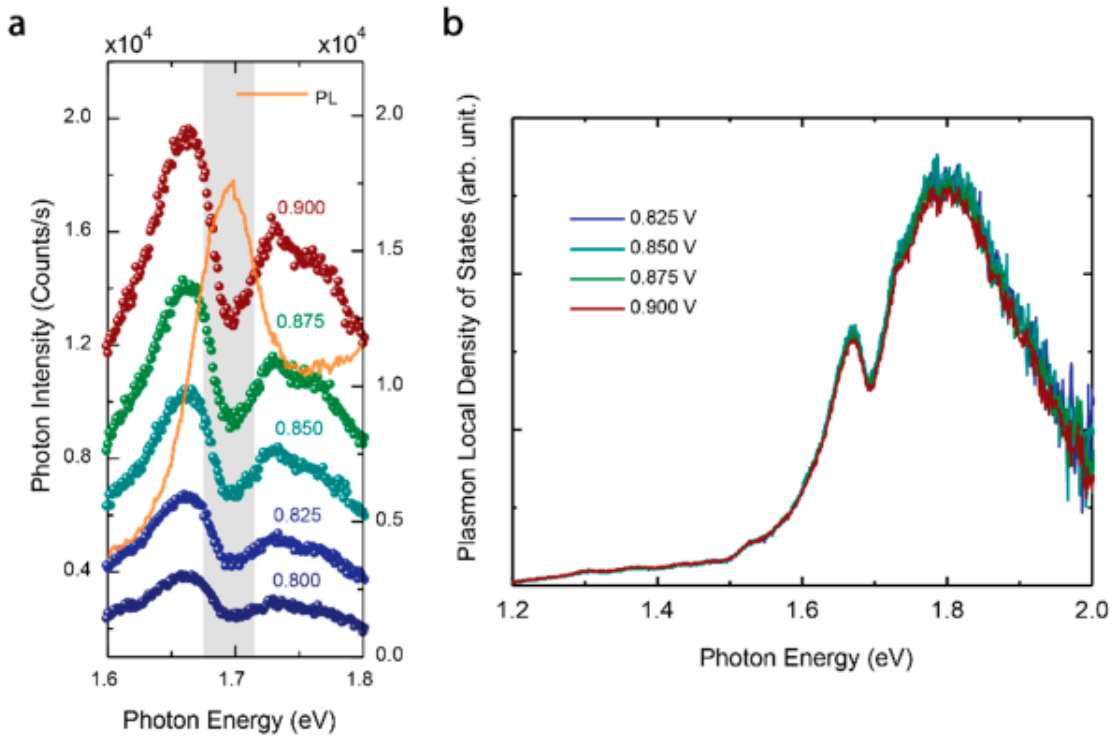

Figure 2-6:[134] **(a) Measured EL spectra at different biases, plotted together with the PL spectrum measured for the WSe_2 on top. (b) Extracted plasmonic DOS obtained by removing the Boltzmann-like hot carrier energy distribution for different biases.**

The discussions in this chapter show the potential of the plasmonic nanowire and nanojunction systems as platforms for large scaler and on-chip optical, electrical, opto-electrical, and thermoelectric applications, such as nanoscale thermal light source, high sensitivity spectroscopy and photodetectors… The plasmonic nanojunctions are also good platforms to study the fundamental physics of highly localized plasmons and hot carriers and their interaction with the environments and other systems.

Chapter 3

Surface Enhanced Raman Spectroscopy in Molecular Junctions via Remote Excitation

In this chapter I will discuss the project about the remote excitation SERS including the device fabrication, experimental setup, data analysis, and simulation. This chapter is based on the publication **"Quantifying Efficiency of Remote Excitation for Surface-Enhanced Raman Spectroscopy in Molecular Junctions"**.[135] The theoretical and simulation parts are done by the collaborators Qian Ye, Dr. Keith Sanders and Prof. Alessandro Alabastri.

3.1. Motivation

The easiest way to optically excite the nanogap system for SERS as well as OCPV is to shine the laser directly at the gap. In the direct excitation configuration, however, local heating of the metal is substantial, with the temperature rise of the nanowire reaching ~100 K with 220 kW/cm^2 incident laser intensity when the

substrate temperature is low.[111] This greatly hampers potential further manipulation of the molecules, such as electrostatic gating and inelastic electron tunneling spectroscopy.[136,137] Remote exaction for SERS has been demonstrated in the recent years in nanorods and tip-based systems.[138,139] A laser is shone at the location which is several micrometers away from the SERS hotspot and molecules. SPPs are generated and propagate to the molecule position to excite SERS signals. The efficiency of this remote SERS approach has not been examined in detail. In the nanowire system, SPPs are generated at the gratings which are several micrometers away from the junction with laser polarization perpendicular to the grating slits. Remote excitation gives a temperature rise a factor of 60 smaller than direct excitation.[140] Besides, OCPV, as a probe of the plasmonic properties, by remote excitation in the electromigrated junctions is also observed.[141]

3.2. Device fabrication

All the devices are fabricated on Si wafers with 2 μm thick thermal oxide SiO_2 layer. First, 50 nm thick large contact Au pads with a 5 nm Ti adhesion layer are first prepared by shadow mask E-beam evaporation, as shown in Figure 3-1. There are 24 (12*2) contact pads at the two sides of the common ground pad. 24 Au nanowires will connect each pad with the common ground.

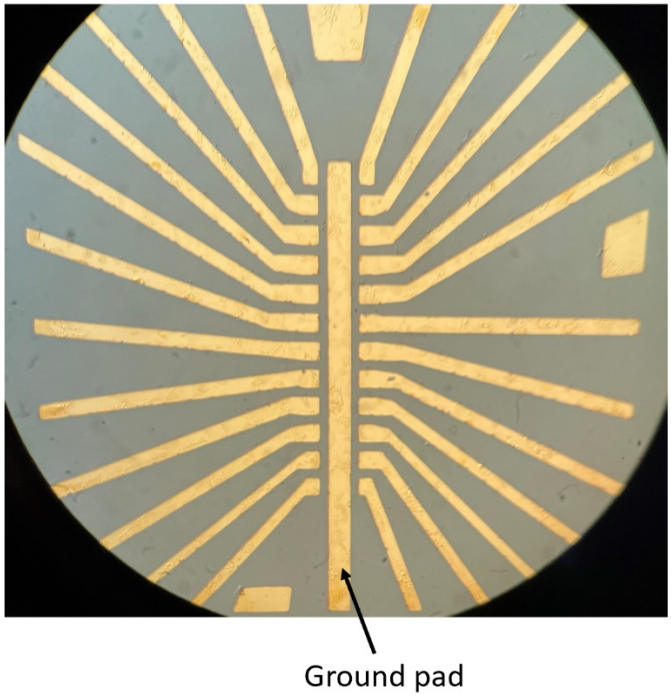

Figure 3-1: SiO2/Si chip with Au contact pads by shadow mask E-beam evaporation.

The chip is cleaned by acetone, ethanol and isopropyl alcohol (IPA) and then followed by oxygen plasma cleaning for 5 minutes. After cleaning, two layers of E-beam resist polymethyl methacrylate (PMMA) 495 and 950 are spin coated. First, the PMMA 495 is spin coated with 3000 rpm for 60 seconds and then the PMMA 950 is spin coated with 4000 rpm for 40 seconds. The chip is baked at 225 Celsius for 2 minutes after each spin coating. The width of Au nanowire is designed to be 120 nm and the length is 800 nm. The center of the grating is 5.9 μm away from the nanowire center. The slits are 8 μm long and 250 nm wide, and the distance between the slits is 500 nm. The thickness of Au is 30 nm. The above parameters for the geometry of the

device are determined based on the previous work.[140] The nanowire and the gratings with geometry discussed above are written by the Elionix E-beam lithography system.

After E-beam lithography, the device is developed in the developer which is made of Methyl isobutyl ketone (MIBK) and IPA with a ratio of 1:3 for 45 seconds. After developing and a following quick plasma cleaning, 30 nm thick Au is evaporated using E-beam evaporator with rate of 0.2-0.3 Å/s under 10^{-6} mbar pressure. Then the device is lifted off by acetone for about 6 hours. The scanning electron microscope (SEM) images of the device are shown in Figure 3-2.

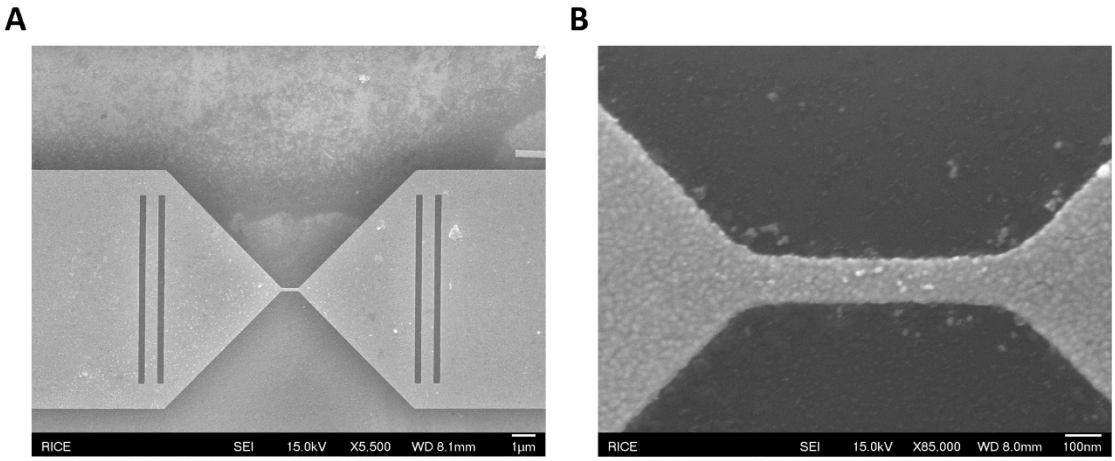

Figure 3-2: SEM images of the device before electromigration. (A) Low magnification SEM image, showing the gratings and the nanowire. (B) High magnification SEM image, focusing at the nanowire.

After lift-off, the molecules are deposited to the device. The chip is soaked in 20 mL ethanol solution with 1 mM benzene-1,4-dithiol (BDT) for 24 hours inside a nitrogen glovebox with oxygen concentration less than 0.1%. The BDT molecules can be self-assembled on the Au nanowire surface due to Au-S linkage.[142,143] The devices are wire bonded at the Au contact pads and chip carrier after molecule deposition. Then the device with the chip carrier is mounted into the Montana Instruments Cryostation.

The nanowire is electromigrated at 30 K to form the junction:[113] an increasing voltage bias is applied by the source meter Keithley 2400 to the nanowire and the current is monitored as a feedback simultaneously. The bias increases from 0.1 V by steps of 0.001 V until the current drops, indicating an increase in resistance, or the voltage bias reaches 1 V. Then the bias is set to 0.1 V to start a new cycle. The cycles are repeated until the conductance of the device is smaller than conductance quantum G_0 (12.9 $k\Omega$ in resistance), which we assume the nanogap is formed (Figure 3-3A). The resistance of the device after each cycle is shown in Figure 3-3B. There's

chance for the BDT molecules on the Au surface to fall into the nanogap during the electromigration process and form a molecular junction.

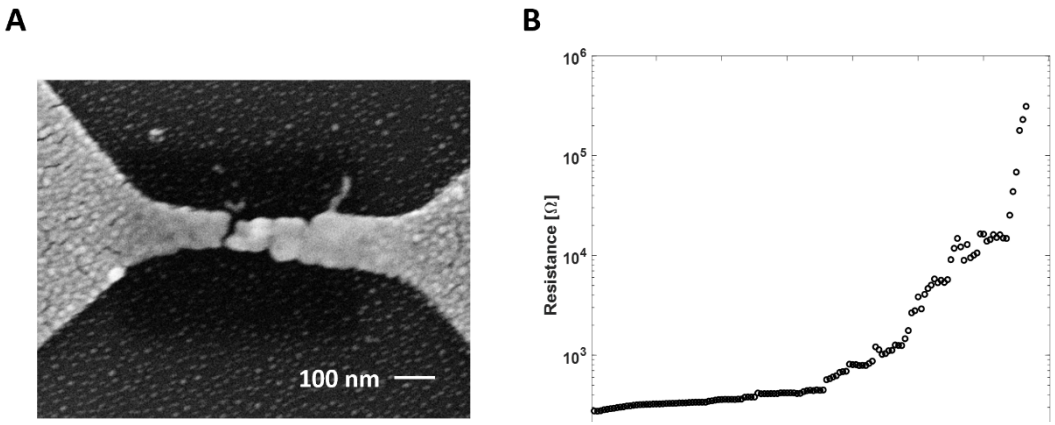

Figure 3-3: (A) SEM image of the nanowire after electromigration. (B) The resistance of the device after each electromigration cycle.

3.3. Experimental setup

All measurements are performed using a home-made Raman system, as shown in Figure 3-4. The sample is placed in Montana Instruments Cryostation and then cooled down to 30 K. We use 785 nm continuous wave (CW) laser to excite the system. The power of the laser is controlled by a half waveplate (HWP) and a polarizer. The polarization of the laser is controlled by another HWP. The polarization angle in the sample plane is marked by θ. The emission from the laser is modulated by an optical chopper, whose frequency is the reference for the lock-in amplifier. The laser is focused at the sample plane by a Zeiss Epiplan-Neofluar 50× objective. The diameter of the laser spot is 1.8 μm measured by knife-edge. We can shine the laser on the

junction with normal incidence for direct excitation and shine the laser at the grating with a small angle deviation by tilting mirror M1 after normal incidence. The OCPV is first amplified by the voltage amplifier SRS 560 (not shown in the Figure) and measured by the lock-in amplifier SRS DSP 7270. Both remote and direct Raman signals are collected by the same objective. The 785 nm signal reflected by the sample is blocked by the Bragg Notch filter (BNF), and the Raman signals are focused at the Synapse CCD spectrometer. Note that the gratings also behave as a SERS substrate, so it is important to block the SERS signals from the grating during SERS measurements by remote excitation. There's an angle difference between the SERS photons coming from the junction and grating when they enter the spectrometer. By setting the entrance slit width of the spectrometer to be 0.05 mm, all signals from the grating can be blocked. The position sample stage is controlled by a nano-positioner (ANC 300 Piezo Controller) in x, y and z directions. The map scans can be measured with the moving sample stage and fixed laser spot position. A CCD camera shows the optical image of the device and helps to focus the laser at the junction and gratings.

The SERS signals by remote excitation before and after electromigration are measured, as shown in Figure 3-5. After electromigration, there are several Raman modes of the BDT molecule in the range of 1000 to 1600 cm^{-1}. Some Raman modes are overlapping, but four Raman modes can still be assigned according to previous reports.[144–146] Before electromigration, there are no detectable Raman modes in this range, consistent with the signal originating from the junction once the nanogap hotspot is created by electromigration.

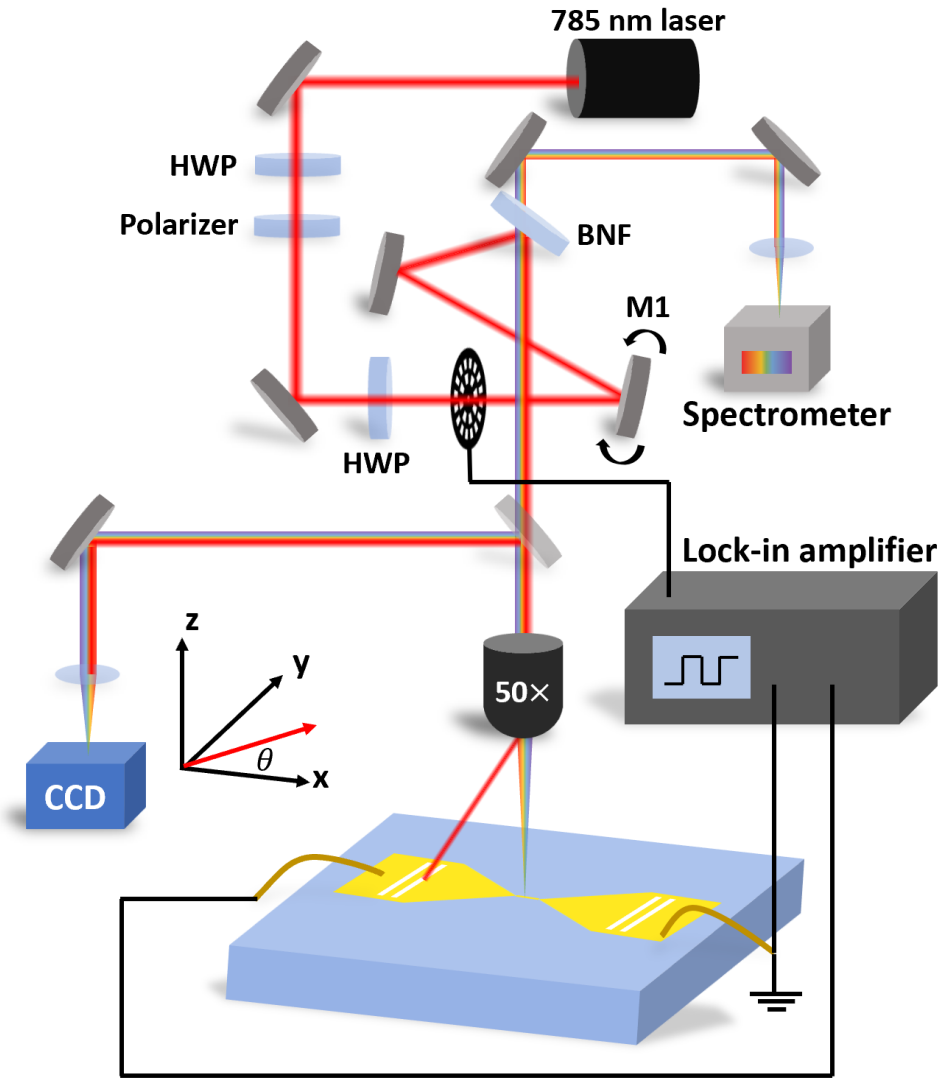

Figure 3-4: Scheme of OCPV and SERS measurement setup

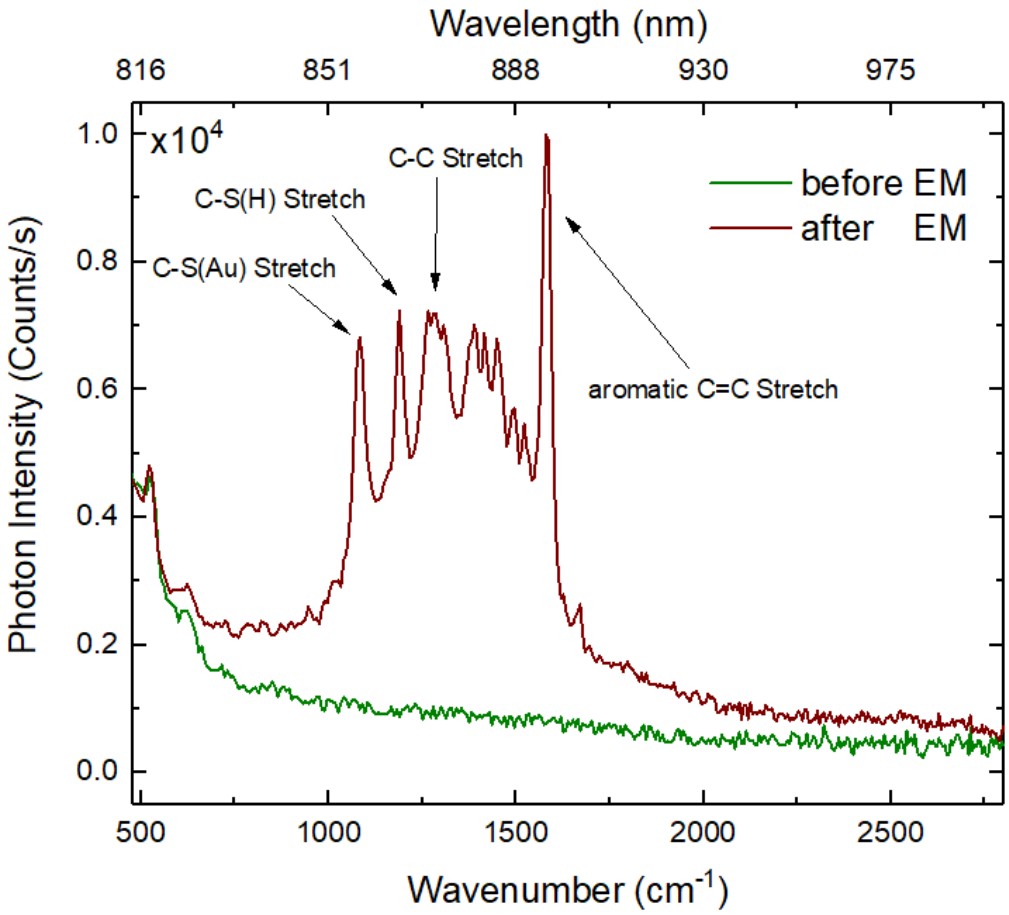

Figure 3-5: SERS spectra under remote excitation before and after electromigration. Before electromigration, there's no Raman mode, suggesting the Raman signal from the grating is blocked and the Raman modes in the spectrum after electromigration come from the junction by remote excitation.

3.4. Theoretical and simulated analysis on SPPs in vacuum-Au-SiO2 structure

In our system, the propagating SPPs can be described by a simplified 2D model. The scheme is shown in Figure 3-6. The Au layer (region 1) is 30 nm thick and the vacuum (region 3) and SiO_2 (region 2) are set to be infinitely thick. Assuming SPPs propagating in x direction, we can get the electric and magnetic field in the three regions.[1]

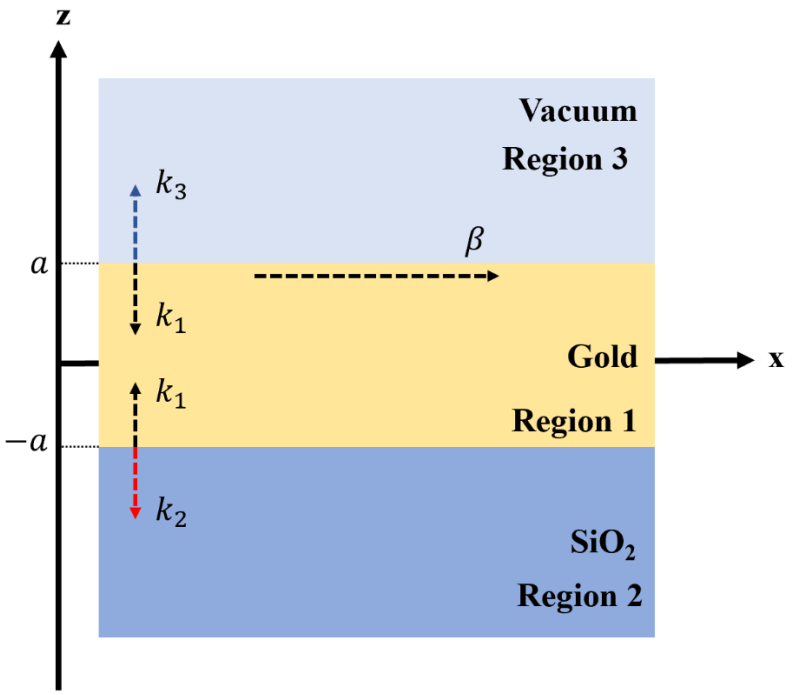

Figure 3-6: Scheme of the SPPs mode in Vacuum-Au-SiO_2 structure. TM modes are considered. SPPs propagate in x direction.

Considering the continuity of H_y and E_x, the dispersion relation can be written as:

$$e^{-4k_1 a} = \frac{k_1/\varepsilon_1 + k_2/\varepsilon_2}{k_1/\varepsilon_1 - k_2/\varepsilon_2} \cdot \frac{k_1/\varepsilon_1 + k_3/\varepsilon_3}{k_1/\varepsilon_1 - k_3/\varepsilon_3} \quad (3-1)$$

where k_1, k_2, k_3 are the wave vectors in region 1, 2, 3 in z direction respectively; β is the wave vector in SPPs propagation direction; ε_1, ε_2, ε_3 are the dielectric function in region 1, 2, 3 respectively. $2a = 30\ nm$ is the thickness of Au. The wave equation for TM modes is:

$$\frac{\partial^2 H_y}{\partial z^2} + (k_0^2 \varepsilon - \beta^2) H_y = 0 \quad (3-2)$$

we have:

$$k_i^2 = \beta^2 - k_0^2 \varepsilon_i \quad i = 1, 2, 3 \quad (3-3)$$

where k_0 is the wave vector of the input laser. By solving the equations above, every wave vector in the system can be solved:

$$k_1 = 3.858 \times 10^7 + 1.139 \times 10^6 i \quad (3-4)$$

$$k_2 = 5.25 \times 10^6 + 3.256 \times 10^5 i \quad (3-5)$$

$$k_3 = 9.94 \times 10^6 + 1.720 \times 10^5 i \quad (3-6)$$

$$\beta = 1.276 \times 10^7 + 1.339 \times 10^5 i \quad (3-7)$$

The wavelength of SPPs is calculated to be $Re\left(\frac{2\pi}{\beta}\right) = 492$ nm. The calculation details are shown in **Appendix A.**

A simulation of SPPs generation is performed to do a comparison. The simulation is done in COMSOL Multiphysics with a 2D model containing the gratings (Figure 3-7A). The simulated wavelength of the SPPs is 489 nm (Figure 3-7B), consistent with the theoretical result. The diffraction pattern through the grating slits is clearly seen in Figure 3-7C.

To have a better understanding of the SPPs in our system, the SPPs in Au-vacuum and Au-SiO_2 interface is simulated. The results are shown in Figure 3-8. The decay length of the electric field in z direction is about 30 nm for both cases, which means the SPPs in the vacuum-Au-SiO_2 structure is the summation of SPPs in Au-vacuum and Au-SiO_2 interface.

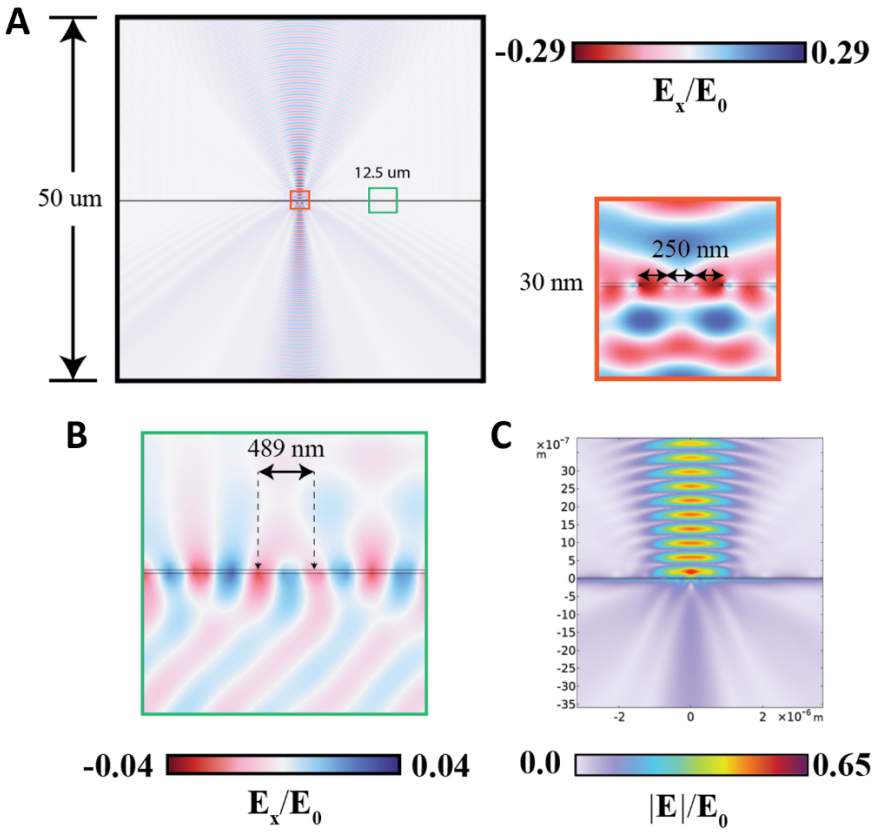

Figure 3-7: Simulation of SPPs generation. (A) Scheme of the 2D model with Gaussian laser beam input. The right panel (the enlarged image of the orange box in the left panel) shows the grating geometry and the surrounding electric field distribution. Au layer is 30 nm thick. (B) Electric field distribution in the area indicated by the green box in (A). The wavelength of the SPPs is 489 nm. (C) Electric field amplitude distribution. Diffraction pattern is formed in the substrate.

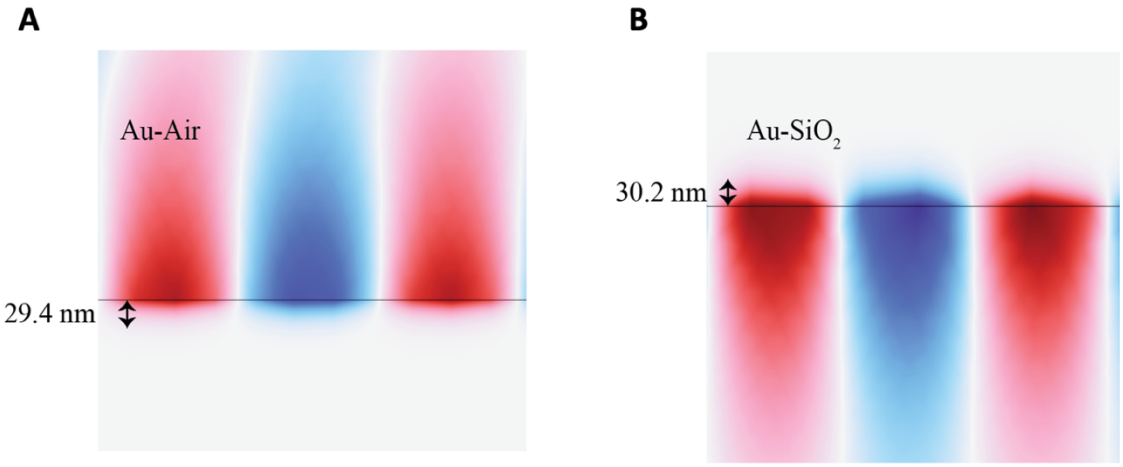

Figure 3-8: (A) Simulated SPPs at Au-vacuum interface, the decay length in Au is 29.4 nm. (B) Simulated SPPs at Au-SiO_2 interface, the decay length in Au is 30.2 nm. The vacuum and SiO_2 are set to be infinitely thick.

3.5. Polarization dependence of OCPV and Raman spectrum by direct and remote excitation

Maps of OCPV and SERS signal are measured by moving the laser spot over the junction and grating area with user-defined pixel size. The OCPV V_{OC} and SERS are measured at each pixel. The results are shown in Figure 3-9. To quantify SERS response for these maps, all the Raman photon counts are summed up in the 1000 to 1600 cm^{-1} range. As the OCPV and SERS are known to change linearly with the input optical power when the input optical power is low (lower than 100 $\mu W/\mu m^2$),[117,147–149] both the OCPV and Raman count rate are normalized by the incident laser power.

OCPV is an additional benchmark for judging the degree to which incident optical energy is concentrated into the nanogap LSPRs. Strong excitation of nanogap LSPRs is essential to generate a substantial OCPV, just as such LSPR excitation is needed for SERS response. There is not a simple, direct correlation between OCPV and SERS response, however, because even at fixed nanogap tunneling conductance, the magnitude of the OCPV depends on the asymmetry of the nanogap and the particular LSPR modes. Indeed, the magnitude and even the sign of the OCPV under remote excitation can vary substantially.[141]

When the incident laser is polarized in the 90 degree orientation (transverse to the nanowire and parallel to the grating slits, θ=90), we can see very strong OCPV and SERS by direct excitation of the nanogap but there is almost no signal when the laser spot is positioned for remote excitation of the grating. Conversely, when the laser is polarized in the 0 degree orientation (parallel to the nanowire and transverse to the grating slits, θ=0), we can see a much weaker OCPV and SERS by direct excitation of the nanogap, but the signal is strong when the laser is positioned on the grating for remote excitation.

These observations are consistent with expectations: the 90 degree polarized light, by direct excitation, can couple to the transverse dipolar plasmon mode of the nanowire, which is hybridized with high order LSPR modes localized at the nanogap due to the asymmetric geometry of the junction,[10,15] as shown in Figure 3-10. As a result, a stronger plasmon resonance is generated for this incident polarization. This

has two consequences. Efficient excitation of the nanogap LSPRs by direct illumination of the nanogap generates a large number of hot electrons via decay of the plasmon, leading to a larger OCPV[117] (Figure 3-9A, left panel). The stronger LSPR response also leads to a highly localized and dramatically enhanced electric field, which contributes to the larger SERS signal[10] (Figure 3-9B, left panel). Conversely, for remote excitation, the 90 degree polarized light cannot couple efficiently to the grating, so that very little energy is transferred to SPPs. Thus, both the remote OCPV (Figure 3-9A, right panel) and SERS signals (Figure 3-9B, right panel) are small.

When the laser is polarized in the 0 degree orientation, however, although the coupling to the nanowire transverse plasmon mode is weak, the high order plasmon modes localized at the gap can be still weakly excited by direct illumination. This weaker plasmon response still results in some hot carrier tunneling and localized electric field enhancement, so we can still see the OCPV (Figure 3-9C, left panel) and SERS (Figure 3-9D, left panel) signals by direct excitation. For remote excitation, 0 degree polarized light can couple efficiently to the grating and generate SPPs which then propagate to the junction, couple to the nanogap LSPRs and create hot electrons and enhanced fields, so we have both relatively large remote OCPV[141] (Figure 3-9C, right panel) and SERS (Figure 3-9D, right panel) signals.

The dominance of the nanowire transverse plasmon mode for direct illumination as described above is quite sensitive to nanowire width and thickness. Over the whole ensemble of devices, by direct excitation, about 70% show that both

SERS and OCPV are larger with the 90 degree polarized light (Figure 3-9). The remaining 30% of devices under direct illumination of the nanogap have maximum OCPV and SERS responses closer to the 0 degree incident polarization. This variation can be explained by the several nanometers Au thickness variation and roughness as well as device-to-device variation of the gap geometry. The details will be discussed in the next section.

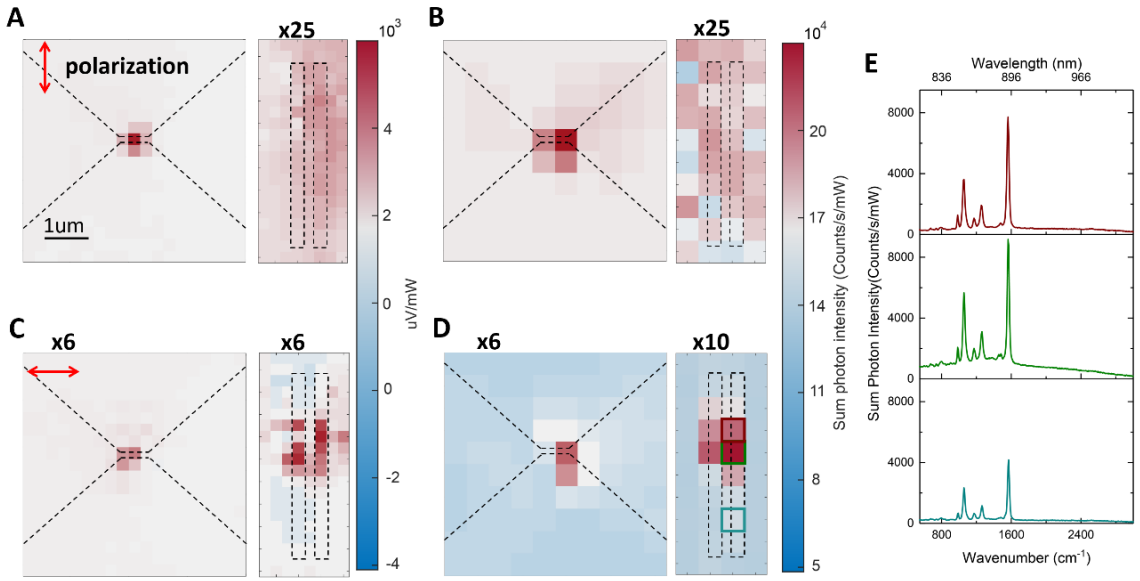

Figure 3-9: Maps scans of OCPV and SERS by direct and remote excitation with different input laser polarization. (A) OCPV with 90 degree polarized light. (B) SERS with 90 degree polarized light. (C) OCPV with 0 degree polarized light. (D) SERS with 0 degree polarized light. (E) SERS spectra with the excitation positioned at the pixels indicated in (D).

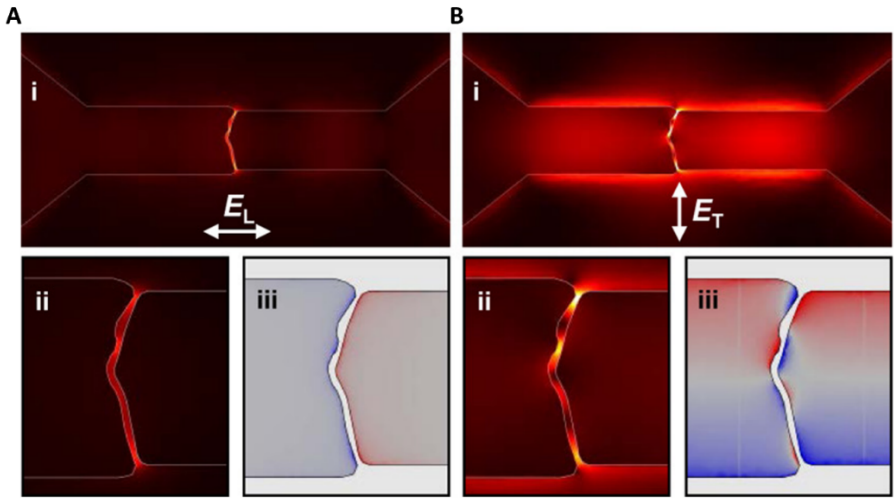

Figure 3-10:[10] **electric field distribution around the nanowire (i), in the gap (ii) and electric charge distribution across the gap (iii) with 0 degree (A) and 90 degree (B) polarized light excitation. Larger electric field and charge density are clear in (B).**

It is important to consider the factors that affect the efficiency of remote excitation SERS relative to direct excitation SERS. Qualitatively, during the remote excitation process, there are some energy losses when the light couples to the grating, and in the excitation of the propagating SPPs, in their propagation to the junction region and in their coupling to the nanogap LSPRs. Due to these inefficiencies, the OCPV and SERS by remote excitation are much smaller than those by direct excitation for a fixed laser power. The OCPV and SERS signals by direct excitation are highly localized at the pixel containing the gap, no matter the polarization of the laser. The

remote signals are largest when the laser spot is positioned at the middle area of the grating because the coupling efficiency between the grating and the incoming laser, and between the grating and the propagating SPP modes, is higher in that configuration. The SERS spectra measured at different pixels at the grating by remote excitation are shown in Figure 3-9E. The Raman modes positions and relative strength are the same; the only difference is the magnitude of Raman intensity, as moving the laser away from the middle of the grating degrades the efficiency of coupling energy to the nanogap.

3.6. Simulated E field and charge distribution for direct and remote excitation

Electric field and charge distribution under both direct and remote excitation are simulated in COMSOL Multiphysics to compare with the experimental results. The details about the COMSOL model geometry and settings are shown in **Appendix B**.

The electric charge and field distribution around the gap can be simulated as shown in Figure 3-11 and 3-12 for remote and direct excitation, respectively. For remote excitation, both the electric field and charge for 0 degree polarized light are larger than 90 degree polarized light, which qualitatively agrees well with the experimental results in Figure 3-9. We still can see the simulated filed enhancement factor exceeding 20 because of the contribution of the diffraction light propagating in SiO_2 substrate to the gap. For direct excitation, we can see the electric field is greatly

enhanced for both polarizations. The enhancement factors are over 100, much larger than remote excitation. This is consistent with the experimental results in Figure 3-9.

For direct excitation, however, both the electric field and charge for 0 degree polarized light are larger than for 90 degree polarized light, which is inconsistent with the experimental results. By reducing the thickness of Au layer in simulation to 20 nm, results are consistent with the experiments, with larger enhancement factor and charge under 90 degree direction polarized light excitation (Figure 3-13). These simulations show that the polarization dependence of the enhanced field is quite sensitive to the assumed thickness of the metal. There are several potential contributors to this issue. First, the effective dielectric function of the real Au layer deviates slightly from the theory value we use in the simulation due to the adsorbates, Au surface roughness and grain boundaries, and other defects from device fabrication. Second, the thickness of the Au layer may deviate the designed value of 30 nm by a few nm during e-beam evaporation, and the local thickness of the metal near the junction can change during the electromigration process. Third, the polarization dependence behavior is also related to the detailed geometry of the gap, which can evolve through annealing between when the measurements are performed and when electron microscopy is used to find a geometry to use in the simulation. The relationship between the Au thickness in simulation and field enhancement factor for both polarizations under direct excitation is shown in Figure 3-14.

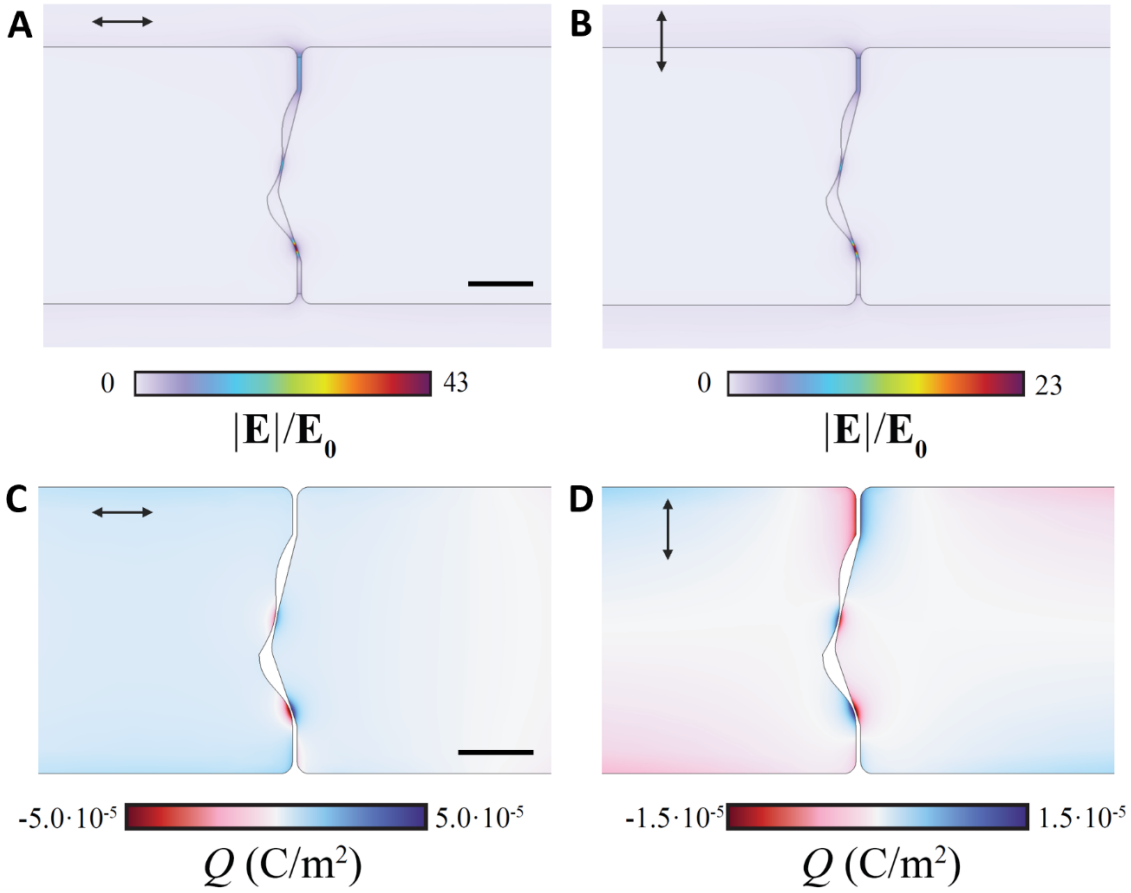

Figure 3-11: Electric field enhancement and charge distribution under remote excitation with 30nm thick Au layer. (A) (B) Field enhancement with different laser polarizations. (C) (D) Electric charge distribution with different laser polarizations. Polarization directions are indicated by the black arrows. The scale bars are 30 nm.

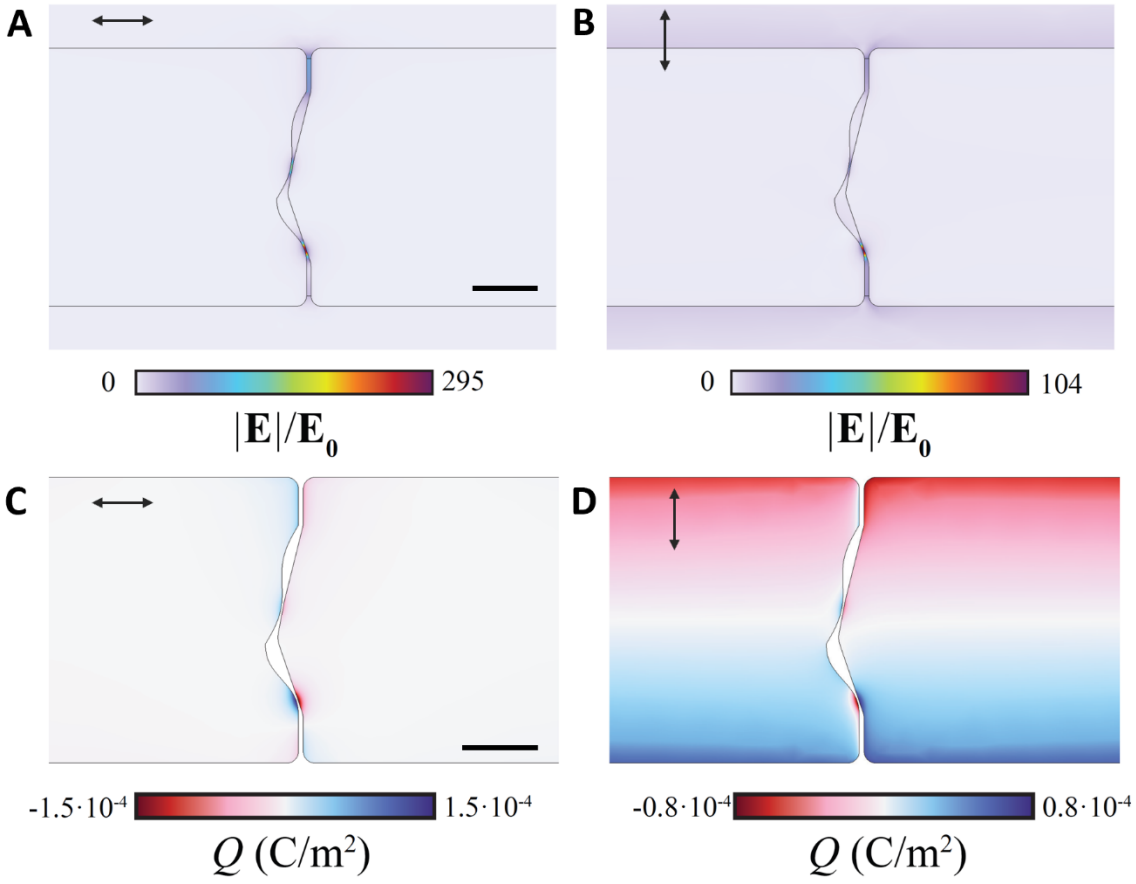

Figure 3-12: Electric field enhancement and charge distribution under direct excitation with 30nm thick Au layer. (A) (B) Field enhancement with different laser polarizations. (C) (D) Electric charge distribution with different laser polarizations. Polarization directions are indicated by the black arrows. The scales bars are 30 nm.

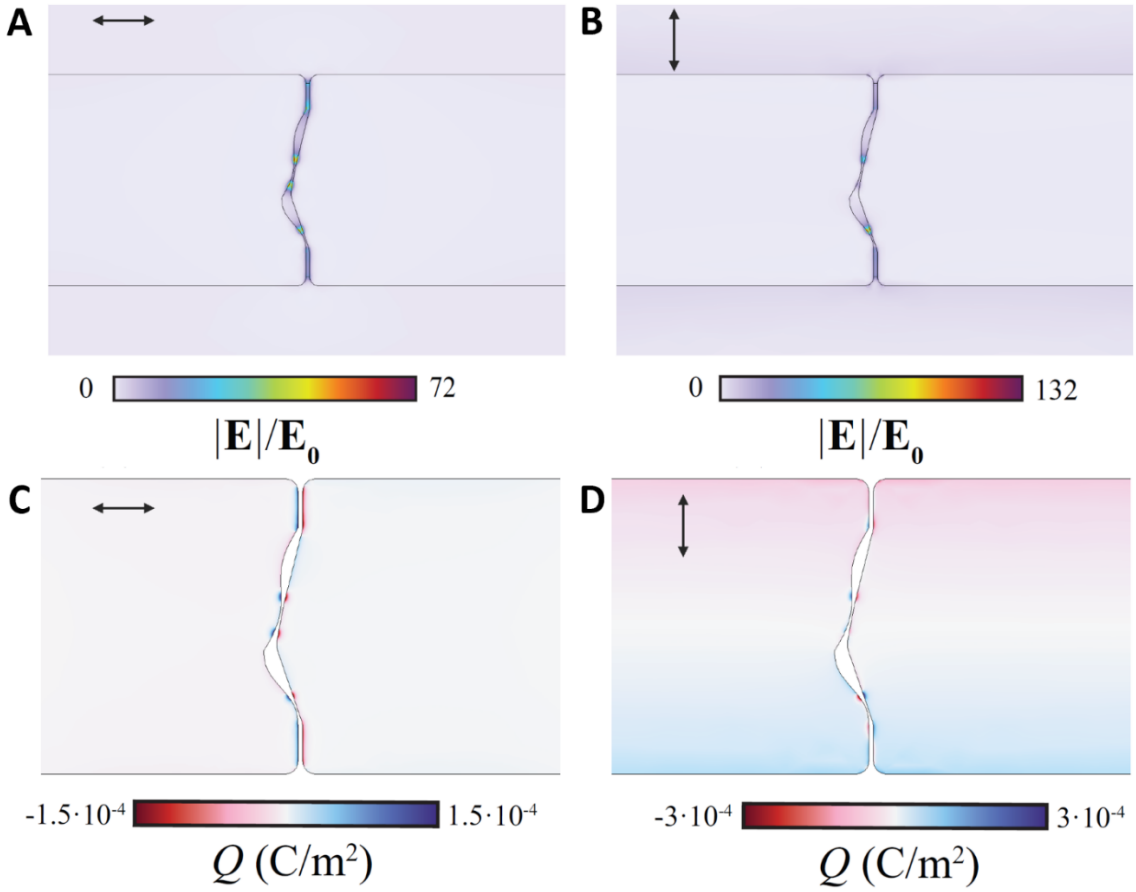

Figure 3-13: Electric field enhancement and charge distribution under direct excitation with 20nm thick Au layer. (A) (B) Field enhancement with different laser polarizations. (C) (D) Electric charge distribution with different laser polarizations. Polarization directions are indicated by the black arrows. The scales bars are 30 nm.

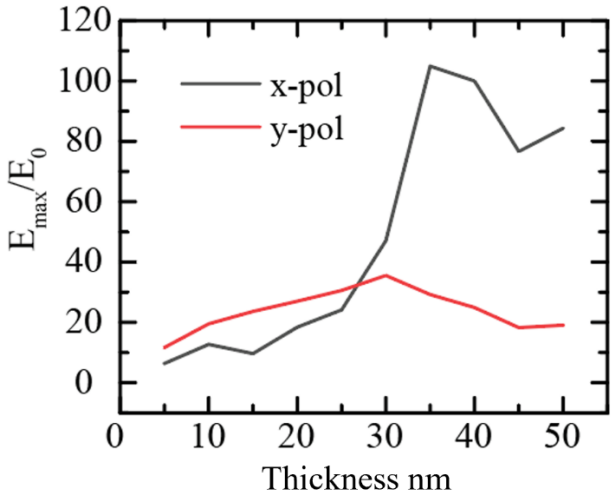

Figure 3-14: The maximum of electric field enhancement with x (0 degree) and y (90 degree) polarized light in the gap under direct excitation vs. Au thickness.

3.7. Statistical analysis on the coupling efficiency of the remote excitation SERS

By measuring an ensemble of 33 devices, we are able to perform a quantitative statistical of the system. SERS by both direct and remote excitation are measured for each device. The coupling efficiency of the remote SERS is defined to be the ratio between photon count rates (in unit counts/s/mW) by remote and direct excitation. As shown in Figure 3-15A, the coupling efficiency averaged across all the devices for each Raman mode is found to be around 10%. For most individual devices, the coupling efficiency averaged across all the Raman modes is also about 10% (Figure 3-16). There are still some devices that show low coupling efficiency less than 5%.

This may be caused by the defects in the Au layer that affect the propagation of SPPs, or by particular nanogap geometries that have lower coupling between the propagating SPPs and the nanogap LSPRs.

The discussion above suggests the 10% coupling efficiency is the intrinsic property of our device design. Electrodynamic simulations reveal one of the dominant mechanisms limiting the efficiency of remote excitation SERS. The details about COMSOL simulations on the energy propagation and absorption are in **Appendix B**. The simulated energy propagation in the +x direction from the grating to the junction is shown in Figure 3-15B, calculated by 3D finite element simulation of the full device geometry and plotting at each x location the x-directed Poynting flux integrated over the transverse cross-section. The simulated power of the input laser is P_0. With 0 degree polarized light (blue curve), about 1.5% of incident energy couples to the grating and into SPPs and starts propagating in the +x direction at around $x = 1500\ nm$. During the propagation, most of that power dissipates, so that only 0.3% of the original incident power reaches the junction at $x = 5900\ nm$ and couples to the local gap modes. With 90 degree polarized light (red curve), almost no energy is coupled into SPPs, and therefore almost no energy reaches the junction. For comparison, the energy absorbed by the nanowire under direct excitation with 90 degree polarization is calculated to be 2.4% of P_0, indicated by the red dashed line. Based on the simulation, therefore, the total coupling efficiency of power to the nanogap just from plasmon dynamics is $0.3/2.4 = 12.5\%$ and qualitatively consistent with the 10% experimental result. A number of additional factors can contribute to

the slightly smaller experimental result, including inefficiencies in the coupling between propagating SPPs and nanogap LSPRs.

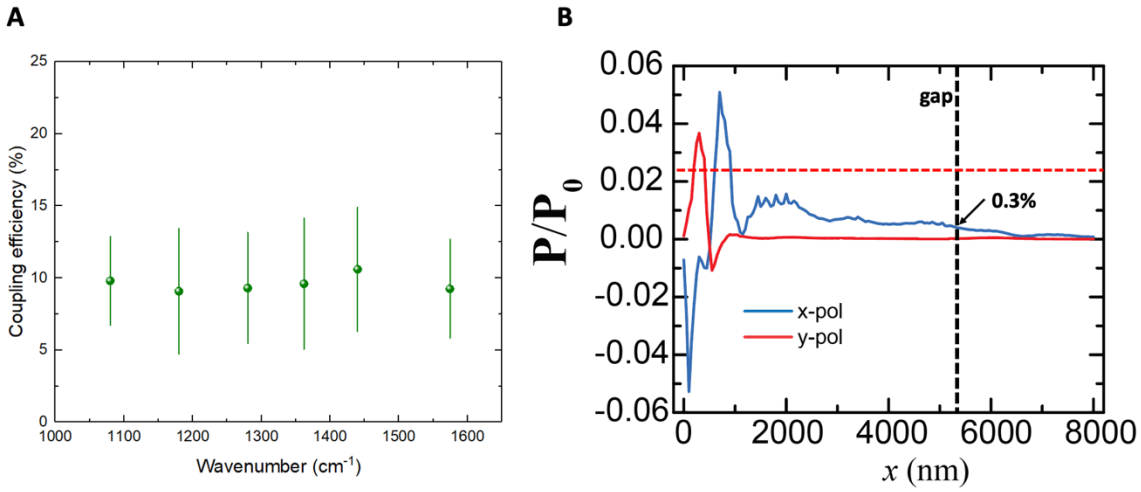

Figure 3-15: (A) Remote SERS coupling efficiency averaged across all devices for each Raman mode. The coupling efficiency is about 10% for all Raman modes. The error bars are the standard deviation. (B) Simulated energy propagation from the grating to the junction the 90 (y polarization) and 0 (x polarization) degree polarizations. The origin is at the middle of the two slits. The junction is at about 5900 nm indicated by the black dashed line. The red dashed line represents the absorption of the nanowire by direct excitation.

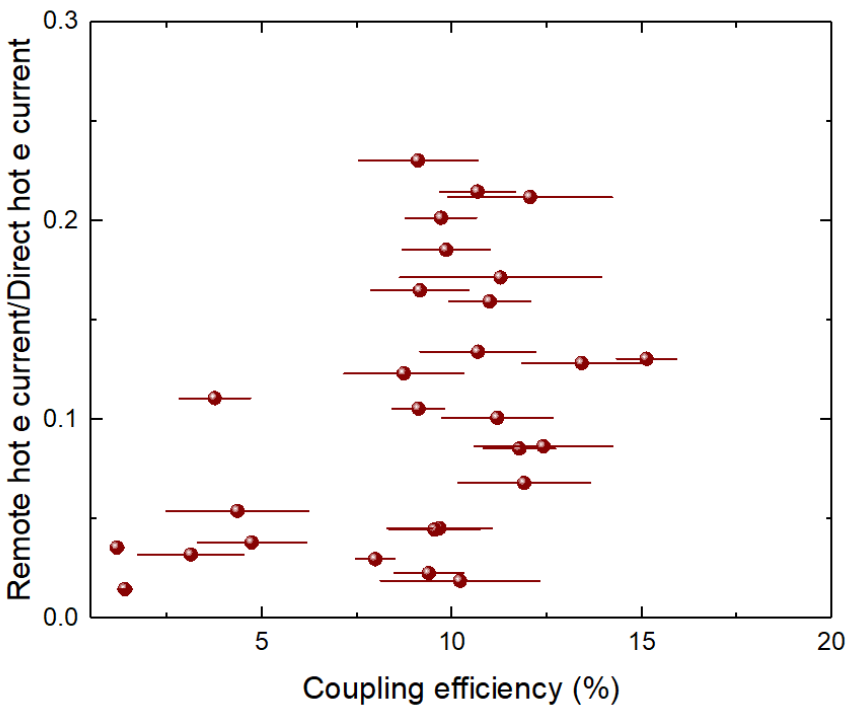

Figure 3-16: Remote SERS coupling efficiency averaged across all Raman modes for each device.

Given the propagation losses, the robustness of the 10% efficiency across many devices implies that the coupling of propagating SPP modes and the nanogap LSPRs is routinely quite efficient, despite microscopic configurational variations from device to device. From the hybridization picture of plasmons[15], this is to be expected. This is in analogy to the idea that a 1D delta function has spectral content from the entire continuum of delocalized harmonic waves in 1D; there should always be overlap and hence coupling between the delocalized SPPs and the highly localized LSPRs at the nanogap.

3.8. Stability of SERS by direct and remote excitation

After the map scans, the laser spot can be moved to the pixel where the SERS signal is the largest, and then time dependent spectra are measured by both remote and direct excitation for the same device to check the relative stability of remote SERS, as shown in Figure 3-17. The input laser intensities are adjusted to make the SERS photon counts comparable. The results shown in Figure 3-17 are typical and have been seen in multiple devices. For direct excitation, the spectra show apparent temporal intensity fluctuations (blinking) and spectral diffusion in the time range of 200 seconds, which are commonly seen in few or single-molecule SERS.[115,150] Initially, several Raman modes in the range of 1200 to 1400 cm^{-1} are strong and overlap each other. Some modes fade away in 60 seconds and we can only see three modes between 60 to 100 seconds. At 110 seconds, a new mode appears and lasts for about 70 seconds. After 180 seconds, there's no detectable Raman modes, indicating that the nanogap molecular junction has degraded. Previous studies report that the origin of the SERS fluctuation are thermal induced molecular reorientation and sub-nanometer configuration changes of the junction.[115,151,152] In our nanowire device, the thermal heating by direct laser illumination and the localized strong electric field enhancement can contributes to the reconfiguration of the molecules and the Au atoms of the junction, and the fluctuations in spectra are usually accompanied by the changes in device resistance.[114,153]

Conversely, the SERS signals are more stable in a much longer time range under remote excitation even when the photon count rate is approximately the same as the direct excitation case. The strongest Raman modes in 1200 to 1400 cm^{-1} remain stable for more than 2500 seconds both for intensity and peak position. There are some fluctuations for other weaker modes but the magnitude of these fluctuations are smaller than the direct excitation configuration. This is consistent with less thermal heating and more stable junction configurations in the remote excitation configuration, implying that remote excitation methods may be better suited for delicate chemical and biological sensing applications.

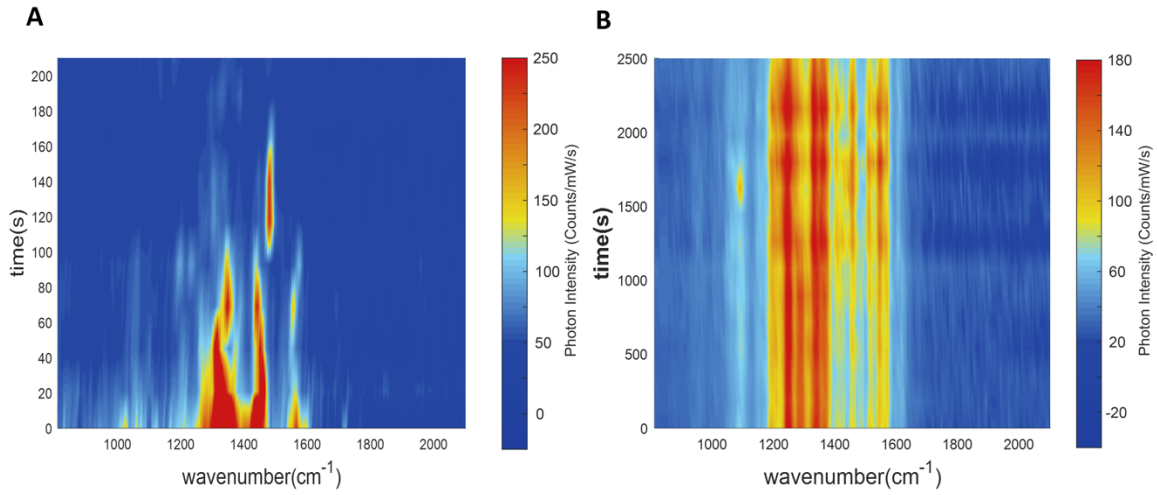

Figure 3-17: Time dependent spectra for the same device by direct and remote excitation. (A) Direct excitation SERS for 200 seconds. (B) Remote excitation SERS for 2500 seconds. The photon count rates are adjusted to be comparable by changing the laser power. Remote excitation SERS is much more stable.

3.9. Summary

The experimental results show the polarization dependent OCPV and SERS under both direct and remote excitation: for direct excitation, 90 degree polarization gives larger OCPV and SERS signals because of the coupling between transverse mode and localized gap modes. For remote excitation, only 0 degree polarization gives detectable signal because of the generation and propagation of the SPPs. The polarization dependence agrees well with the COMSOL simulation results. A statistical analysis is performed and the coupling efficiency of the devices is around 10%, which is supported by the energy flow simulation. The rest of energy is lost

during the SPPs generation, propagation and coupling the gap modes. For a same device, SERS by remote excitation is much more stable than direct excitation, suggesting less laser heating. Remote excitation and its resulting greater junction stability improve the prospects for both sensitive SERS detection of analytes in delicate environments and for combining SERS with challenging electronic spectroscopy techniques such as field-effect gating and inelastic electron tunneling spectroscopy.

Chapter 4

Large Magnetic Field Dependent Electroluminescence in Diamagnetic Plasmonic Nanojunctions

This chapter focuses on the EL behavior of diamagnetic plasmonic nanojunctions in magnetic field. It is based on our paper in preparation "Large Magnetic Field Dependent Electroluminescence in Diamagnetic Plasmonic Nanojunctions". The theory, modeling and simulation parts are performed by our collaborators Jaime Abad-Arredondo, Dr. Antonio I. Fernandez-Dominguez, and Dr. Francisco J Garcia-Vidal.

4.1. Motivation

The effects of external magnetic field on LSPRs have been studied extensively when examining individual metallic, non-magnetic nanoparticles.[154–156] The classical Hall physics, producing off-diagonal components of the permittivity, leads to Kerr rotation[156] and circular dichroism effects in scattering and absorption.[157] Considering

that the off-diagonal components of the permittivity are orders of magnitude smaller than the diagonal terms in diamagnetic materials like gold,[154,158,159] the magnetic effects on the optical response of the diamagnetic nanostructures are generally correspondingly small, which agrees with the small classical Hall angle in diamagnetic materials. Here we demonstrate that experimental EL spectra of planar nonmagnetic plasmonic nanojunctions are quite sensitive to an external static magnetic field, with changes in total emission (all polarizations included) at specific wavelengths up to tens of percent under an external magnetic field of a few Tesla. This exceeds the impact of incorporating the Hall effect into electromagnetic calculations by more than two orders of magnitude. Polarization analysis of the EL spectra shows profound changes that are asymmetric with external field direction. The dramatic tuning of the EL spectra indicates that the near-field radiative density of plasmonic states at the nanogap is modified by the external *B*-field. In addition, a single-particle quantum model suggests that the external magnetic field introduces significant ellipticity to the electronic transition dipoles in the nanogap, and these chiral electromagnetic sources can result in B-dependent changes in emission comparable to the experimental results.

4.2. Device fabrication and experiment setup

The device fabrication is similar to the process mentioned in Chapter 3 for the remote excitation Raman devices, including standard fabrication of nanowires, wire bonding and electromigration. The difference is that for EL measurements, we

prepare the devices on Si chip with 300 nm SiO_2 layer on top, instead of 2 μm thick SiO_2. The reason is that clear interference pattern can be seen from light emission devices with 2 μm thick SiO_2.[112] The interference originates from the direct upward light emission and light reflection from the SiO_2/Si interface, and make it difficult to extract the plasmonic DOS and effective temperature. A typical zero-bias resistance of the nanojunctions following electromigration is tens of kiloOhms (smaller than SERS devices), consistent with a sub-nm interelectrode tunneling distance. An SEM image of the device is shown in Figure 4-1.

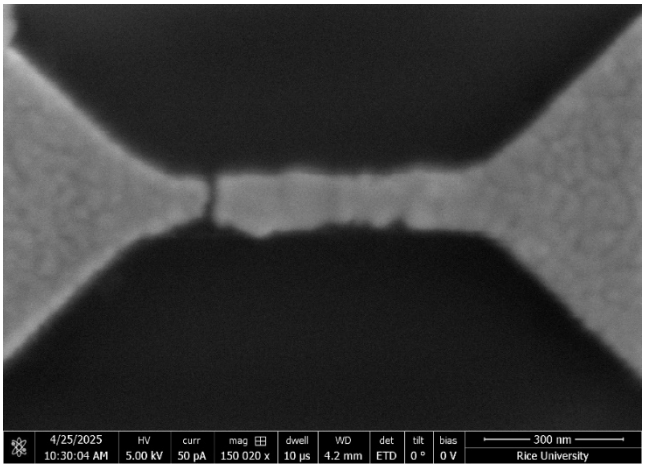

Figure 4-1: An SEM image of the nanojunction device in EL measurements.

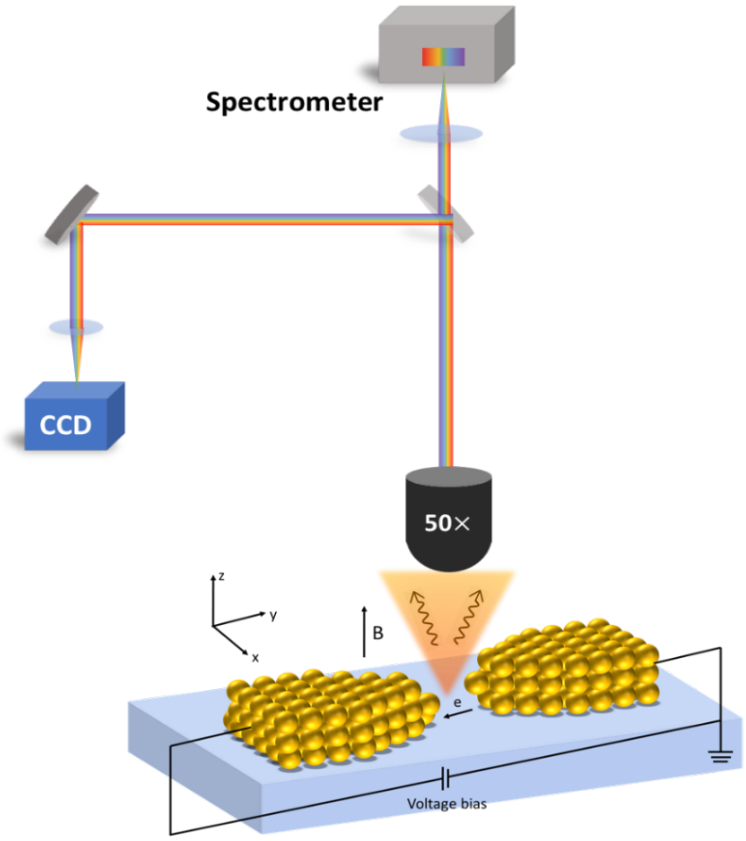

Figure 4-2: Schematic of the EL measurement setup under magnetic field.

The measurement setup is based on a home-build Raman spectroscopy system. The sketch of the optical setup is shown in Figure 4-2. EL photons are collected by an Olympus 50× long working distance objective with 0.35 NA. Spectra are measured using Horiba IHR320 gratings and Synapse Si CCD system. The direct current (DC) bias voltage is applied by a Keithley 2400 source meter which also measured the tunneling current. The sample is placed in a Quantum Design Opticool system with both optical and electrical accessibility with DC magnetic field up to ±7 T. During the

electromigration and measurements, the temperature of the chamber and the substrate is fixed at 10 K help stabilize the devices. The external magnetic field is along the z direction and perpendicular to the device plane. During the EL measurements, the bias voltage is off when sweeping the magnetic field from one value to another one to prevent device degradation due to further electromigration during the long-time bias. The EL measurements are performed when the tunneling current fluctuations are stable to within 5 % to minimize the geometric instability of the devices.

4.3. Magnetic field dependent EL spectra

We have found similar magnetic field response in many junctions, and we highlight data from a particular individual device for clarity. We first measure the spectra under different magnetic field from -6 T to 6 T at 1.1 V bias voltage as shown in Figure 4-3. Both the amplitude and shape of the spectra change dramatically with the magnetic field: the peak near 585 nm has a trend of increasing when the magnetic field increase from -6 T to 6 T. The intensity increases by a factor of 2 from -6 T to 6 T. For the peak around 660 nm, a decreasing trend can be seen when the magnetic field increase from -6 T to 6 T. From -6 T to -2 T, the intensity decreases slightly, and from -2 T to 6 T, the intensity drops from about 3500 counts/s to 1800 counts/s, nearly a factor of 2. The change of the peak around 720 nm is more complicated. From -6 T to 2 T, the trend is decreasing, and from 2 T to 6T, the peak intensity increases. Comparing the ratio between the peaks around 660 nm and 720 nm, from 0 T to 6 T,

we can see that the ratio is getting smaller, and under 6 T, the 720 nm peak is even higher than the 660 nm peak. The changes in EL spectra are asymmetric for positive and negative magnetic field in terms of both amplitude and shape.

A control experiment of Joule thermal emission from unmigrated TiN nanowires under different magnetic field is performed, as shown in Figure 4-4. The voltage is fixed at 3.5 V which is much larger than the EL measurements to make the TiN nanowires hot enough to glow. The light emission from the hot TiN nanowires is purely thermal and is expected to be magnetic field independent[112]. In Figure 4-4, each spectrum is an average of 3 individual spectra measured under the same condition. The average eliminates the spectrum fluctuation due to the instability of the devices at high temperature. The thermal spectra under different magnetic field almost overlap each other, suggesting the thermal emission from our setup is magnetic field independent statistically. The control experiment confirms that the magnetic field dependent EL from the nanojunctions originates from the junctions themselves, not some unlikely artifact of the measurement setup.

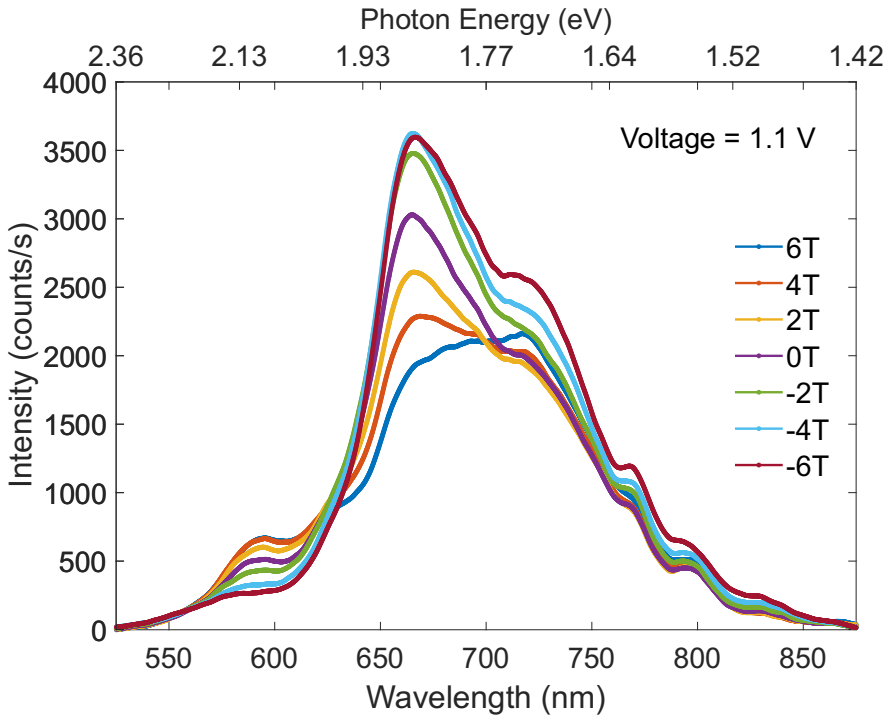

Figure 4-3: The total EL spectra (all polarization included) of a nanojunction device under the external magnetic field of -6 T to 6 T. The bias voltage is set to be 1.1 V. Both amplitude and shape of the spectra change dramatically with the magnetic field.

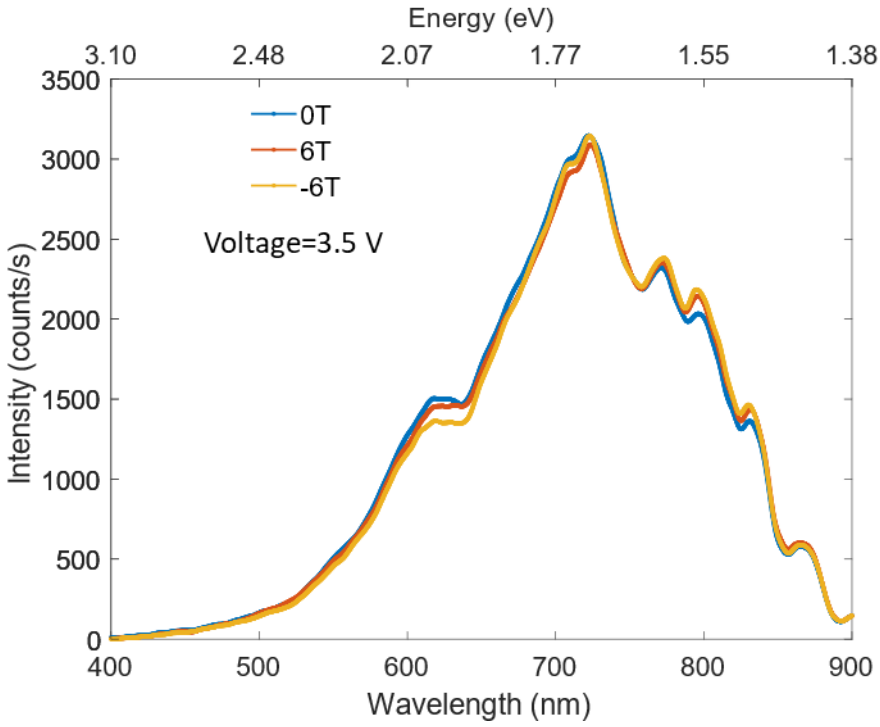

Figure 4-4: Control experiment of thermal emission spectra of a TiN nanowire device under the external magnetic field of ±6 T and 0 T. The bias voltage is set to be 3.5 V. Spectra under different magnetic field almost overlap each other, suggesting the thermal emission from our setup is magnetic field independent statistically.

To understand the magnetic field dependent EL, we first check the tunneling current as a function of the magnetic field using the same device measured in Figure 4-3, as shown in Figure 4-5. The bias voltage is set to be 1.1 V and the current is measured. Under different magnetic field, the current fluctuates from 121 μA to 118 μA, with a fluctuation less than 3 %. Considering the cyclotron radius of electrons in gold is on the order of micrometers under a few Tesla magnetic field, orders of

magnitude larger than the nanogap size, the small fluctuation might originate from the slight instability of the device. Such small changes in tunneling current magnitude cannot explain the change of a factor of 2 in the EL spectra.

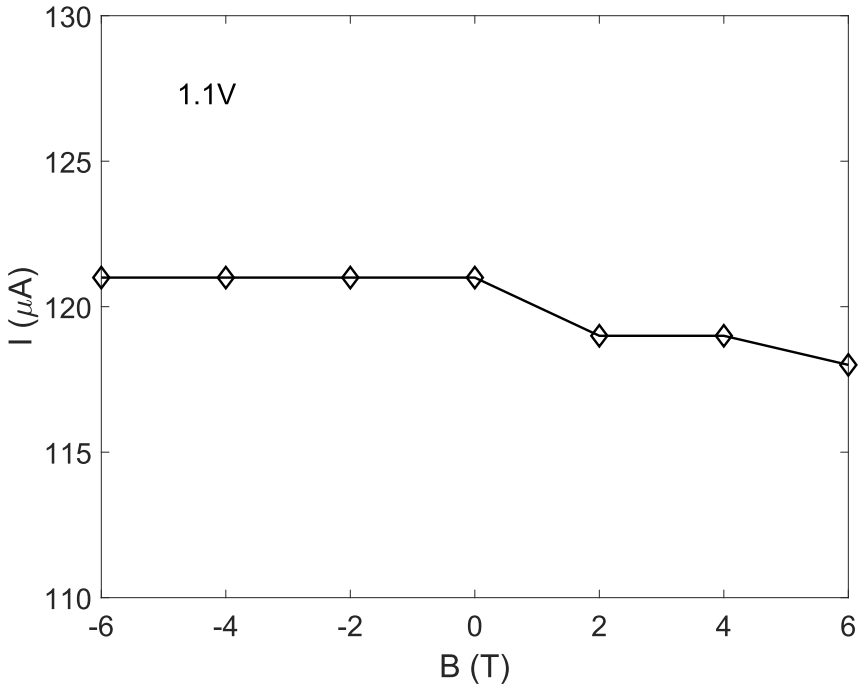

Figure 4-5: The tunneling current of the same device as Figure 4-3 under different magnetic field. The bias voltage is fixed at 1.1 V. The fluctuation of the current is smaller than 3 %, indicating that the current fluctuation and geometric instability are not the reasons for the magnetic field dependent EL.

In addition, we also rule out purely classical Hall physics. The anisotropic properties of the classical Hall effect can be captured by a complex permittivity tensor with non-zero off-diagonal elements which are known as the magneto-optical (MO) function ε_{mo}:[158,160]

$$\varepsilon_{mo} = i\frac{\omega_c(\omega_b\tau)^2}{\omega[(1-\omega\tau)^2+(\omega_c\tau)^2]^2} \quad (4-1)$$

where τ is the electron relaxation time; ω_b is the bulk plasmon frequency as described in Eq. (1-1); $\omega_c = eB/m$ is the cyclotron frequency and B is the magnetic field. The MO function ε_{mo} depends on material properties and the external magnetic field. Suppose the magnetic field is along the z direction, the permittivity tensor $\boldsymbol{\varepsilon}$ can be written as:

$$\boldsymbol{\varepsilon} = \begin{pmatrix} \varepsilon & \varepsilon_{mo} & 0 \\ -\varepsilon_{mo} & \varepsilon & 0 \\ 0 & 0 & \varepsilon \end{pmatrix} \quad (4-2)$$

For noble metals like gold, ε_{mo} is much smaller than the diagonal elements of the permittivity tensor when the magnetic field is a few Tesla.[161] Figure 4-6 shows the complex ε_{mo} of gold as a function of wavelength under 6 T magnetic field using the Drude model. Both the real and imaginary parts are 2-3 orders of magnitude smaller than the diagonal elements in the wavelength range of visible to near-infrared. Similarly, such small ε_{mo} alone cannot explain the change in the EL spectra. This is confirmed by the finite element simulations of absorption spectra of gold plasmonic

nanojunctions with optical excitation under different magnetic field (Figure 4-7). The difference of the absorption between 0 T and 6 T is very small.

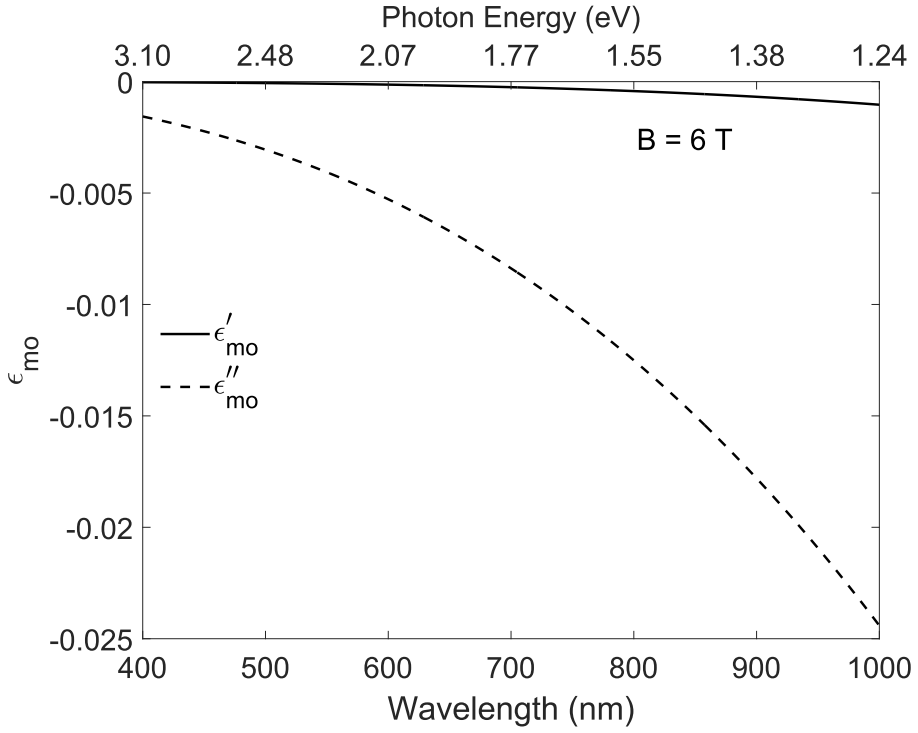

Figure 4-6: Real (ε'_{mo}) and imaginary (ε''_{mo}) parts of the off-diagonal elements of the permittivity tensor of gold as a function of wavelength under 6 T. The MO constant ε_{mo} is too small to explain the magnetic field dependent EL.

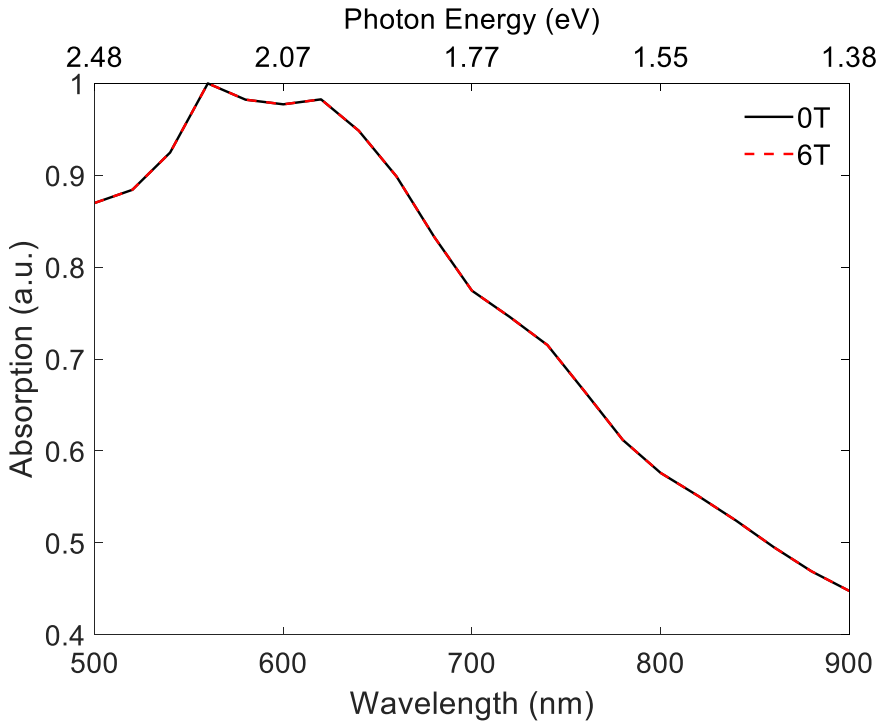

Figure 4-7: The simulated optical absorption spectra of the plasmonic nanojunction under 0 T and 6 T magnetic field. The polarization of the excitation light is along the x direction (parallel to the nanowire). The two spectra overlap each other, implying that the plasmon modes are effectively unaffacted, and therefore the MO effect cannot explain the magnetic field dependent EL.

Besides, the Zeeman physics cannot account for the change in EL, since the Zeeman splitting in gold nanostructures are reported to be on the order of a few meV,[162] much smaller than the energy scale of the EL photons and $k_B T_{eff}$, the corresponding effective temperature of the hot carriers.

4.4. EL at different bias voltage and extraction of the plasmonic DOS and effective temperature

To better understand the magnetic field dependent EL, we measure the EL spectra at different bias voltage under $\pm$6 T and 0 T magnetic field, as shown in Figure 4-8. Under each magnetic field, the voltage dependent spectra have the same shape, and the intensity is higher with larger bias voltage, consistent with previous reports.[33]

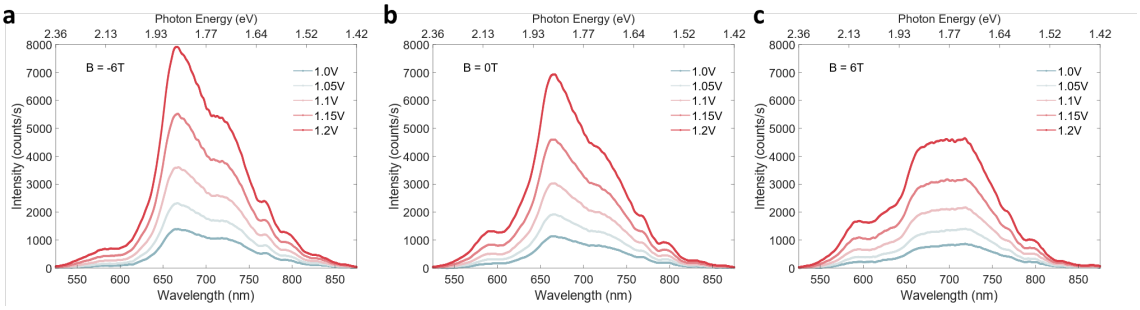

Figure 4-8: The EL spectra (unpolarized detection) with different bias voltage under -6 T (a), 0 T (b) and 6 T (c) magnetic field using the same device in Figure 4-3 and 4-5. At each magnetic field, the voltage dependent spectra have the same shape.

For the spectra under each magnetic field, the normalization analysis can be performed to extract the plasmonic DOS $\rho(\omega)$ and effective temperature T_{eff},[33] as described in Chapter 2: the spectra at each magnetic field in Figure 4-8 are divided by the spectrum with 1.2 V bias voltage and by their current value to the power of 1.2,

We then take log of each normalized spectra, and they can be written as a function of photon energy instead of wavelength:

$$log\left(\frac{U_i\,(\omega, V_i)/I^{\alpha}}{U_{ref}\,(\omega, V_{ref})/I^{\alpha}}\right) = -\frac{\hbar\omega}{k_B}\left(\frac{1}{T_i} - \frac{1}{T_{ref}}\right) \quad (4-3)$$

Eq. (4-3) describes the log normalized spectra are proportional to the photon energy, so we can fit them by a linear function $y = kx$. The log normalized spectra and the fits under $\pm$6 T and 0 T magnetic field are shown in Figure 4-9.

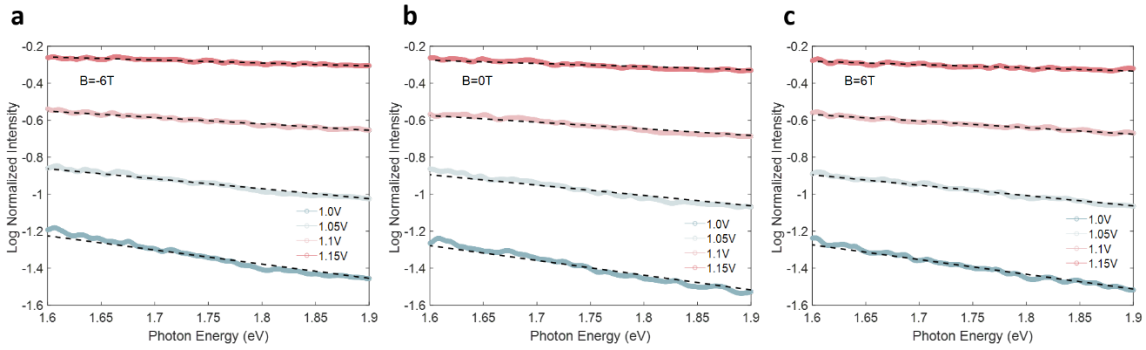

Figure 4-9: The log normalized spectra and the linear fits with different bias voltage under -6 T (a), 0 T (b) and 6 T (c) magnetic field.

For each magnetic field, we have 5 spectra with the 5 different bias voltage (1 V – 1.2V), and at each bias voltage, we have a corresponding effective temperature. However, we only have 4 fitted curve and slope. To solve each effective temperature, we use the assumption that T_{eff} is proportional to the bias voltage:[33]

$$T_{eff} = \beta V_b \quad (4-4)$$

From each fitting, we can get one β value, and all these β values are roughly the same. For example, the extracted β values in Figure 4-9c are 2427.4, 2467.1, 2470.3 and 2389.2. The standard deviation is about 1.53%. The final β is set to be mean value of these extracted β. Then the effective temperature T_{eff} can be obtained at each bias voltage using Eq. (4-4). The effective temperature T_{eff} as a function of the voltage under different magnetic field is shown in Figure 4-10. The effective temperature can reach more than 2000 K with relatively low bias voltage (1 V), suggesting the high efficiency hot carrier generation in the nanojunctions. Once the effective temperature T_{eff} is obtained, the plasmonic DOS $\rho(\omega)$ can be extracted at each bias voltage using Eq. (4-5), as described in Chapter 2.

$$U(\omega, V_b) \approx \rho(\omega) I^{\alpha} e^{-\frac{\hbar\omega}{k_B T_{eff}}} \quad (4-5)$$

We can get the plasmonic DOS $\rho(\omega)$ for each V_b, as shown in Figure 4-11. Under each magnetic field, the plasmonic DOS $\rho(\omega)$ at each bias voltage overlap, suggesting that $\rho(\omega)$ is voltage independent and only dependents on the material and geometry of the nanojunctions.[33] The final $\rho(\omega)$ is the average of $\rho(\omega)$ among all voltage value, as shown in Figure 4-12.

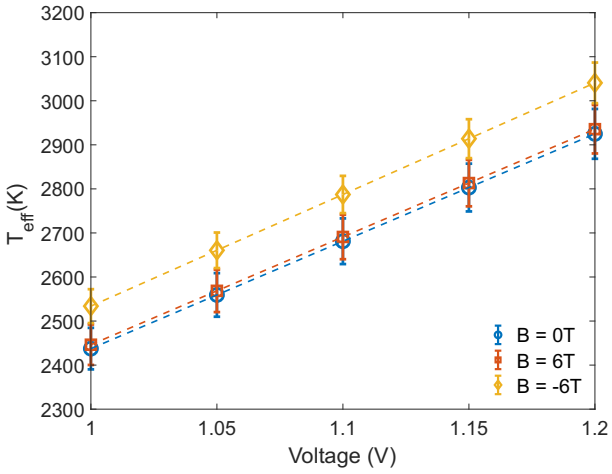

Figure 4-10: The effective temperature T_{eff} inferred from the normalization analysis as a function of voltage a under ± 6 T and 0 T magnetic field. The effective temperature is linear in voltage, consistent with prior hot carrier EL studies.[33] The dashed lines show the linear relationship. The error bars show the 95 % confidence interval.

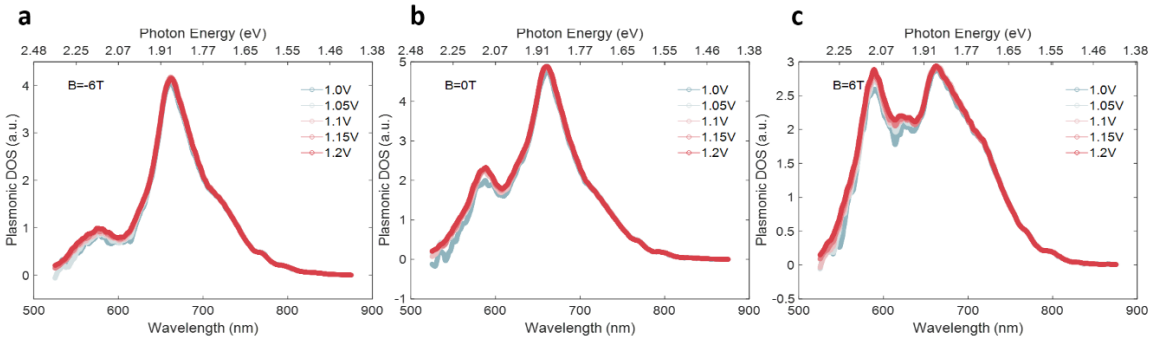

Figure 4-11: The extracted plasmonic DOS $\rho(\omega)$ at each voltage V_b under -6 T (a), 0 T (b) and 6 T (c) magnetic field. Under each magnetic field, the extracted plasmonic DOS $\rho(\omega)$ overlap, which agrees with the result that $\rho(\omega)$ is bias voltage independent.[33]

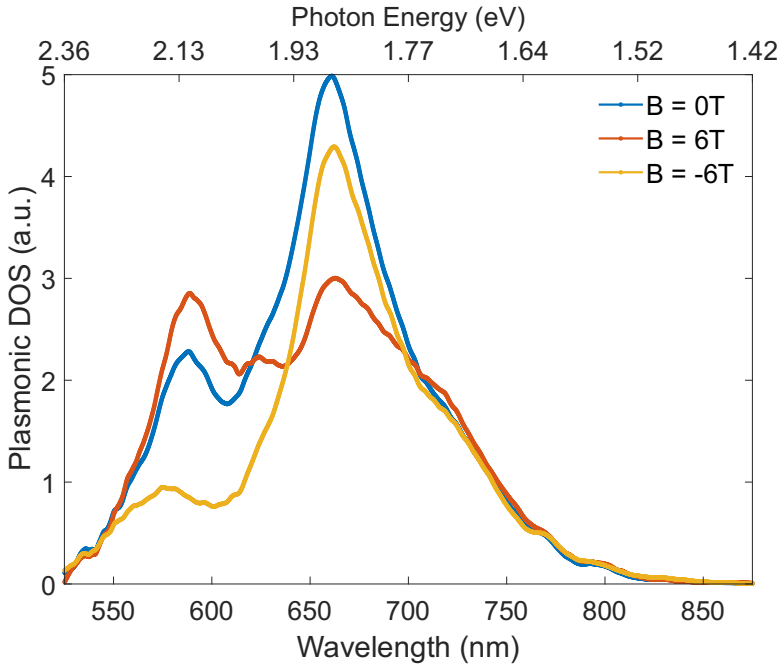

Figure 4-12: The plasmonic DOS $\rho(\omega)$ obtained by the normalization analysis of the EL spectra in Figure 4-8 under $\pm$6 T and 0 T magnetic field.

The normalization analysis is internally consistent at each external magnetic field value, suggesting that the magnetic field has no significant effect on the hot carrier generation and radiative recombination mechanisms in our plasmonic nanojunctions. Figure 4-12 shows that $\rho(\omega)$ varies markedly with magnetic field. In Figure 4-12, the peak near 585 nm increases with increasing magnetic field; the peak around 660 nm is the highest under 0 T magnetic field, followed by -6 T and then 6T; the intensity of the feature near 720 nm slightly increases from -6 T to 6 T; we can also see the appearance of the tiny peak near 615 nm under 6 T. For the effective temperature, under -6 T, T_{eff} is the highest and it reaches more than 2500 K with

moderate bias voltage. The effective temperatures under 0 T and 6 T are roughly the same and slightly lower than that under -6 T. The magnetic field dependent $\rho(\omega)$ indicates that the specific LSPR modes excited in the nanojunction change with the magnetic field, and as a result, the effective temperature describing the hot carriers decaying from these plasmons can be slightly different.

4.5. EL spectra with different polarization under magnetic field

To better understand how plasmon modes change with magnetic field, spectra with different detected polarization are measured, as shown in Figure 4-13 and 4-14. The bias voltage is fixed at 1.1 V and the same device in the previous measurements is used. Spectra as a function of detected linear polarization are shown in Figure 4-13. Figure 4-13a-c shows the polar plots with different magnetic field and Figure 4-13d-e shows line cuts of the corresponding spectra. The linear polarization angle is defined with 0 degrees parallel to the nanowire (y direction, Figure 4-2) and 90 degree is perpendicular to the nanowire (x direction, Figure 4-2). Under each magnetic field, the spectra change dramatically as a function of the detected polarization angle. At 0 degrees, the spectra are dominated by the low energy nanogap modes, and at 90 degrees, the spectra are dominated by the high energy transverse dipolar mode. For the polarization angle between 0 and 90 degree, the spectra are complicated due to the hybridization of the nanogap modes and transverse dipolar mode,[10,15] and the spectra are sensitive to the particular sets of LSPRs excited in the system by the tunneling electrons. Comparing the spectra at

different magnetic field, we can see that the spectra differ a lot at the same polarization angle, which supports the hypothesis that plasmon modes change with magnetic field.

The left-hand and right-hand circular polarized component of the spectra are also measured in Figure 4-14. No matter the magnetic field, large differences in left-hand and right-hand detected spectra can be observed. The dissymmetry factor defined as $g_{lum} = {2(I_{left} - I_{right})}\Big/{(I_{left} + I_{right})}$ under each magnetic field is shown in Figure 4-15. The dissymmetry factor can be close to ± 2 for some specific wavelength. The Circular dichroism is widely studied in plasmonic nanostructures.[163–166] In our nanojunctions, due to the randomness of the electromigration process, the nanojunctions can be highly asymmetric and chiral in geometry (see SEM images Figure 4-1 as an example). The nanogap plasmon modes themselves and the mode hybridization can be chiral, leading to circular dichroism in emission spectra. Under different magnetic field, the circular dichroism is different. This further suggests different plasmon modes are excited under different magnetic field. The plasmonic DOS for the left-hand and right-hand polarization light can be obtained using Eq. (4-5) and the effective temperature in Figure 4-10, as shown in Figure 4-16.

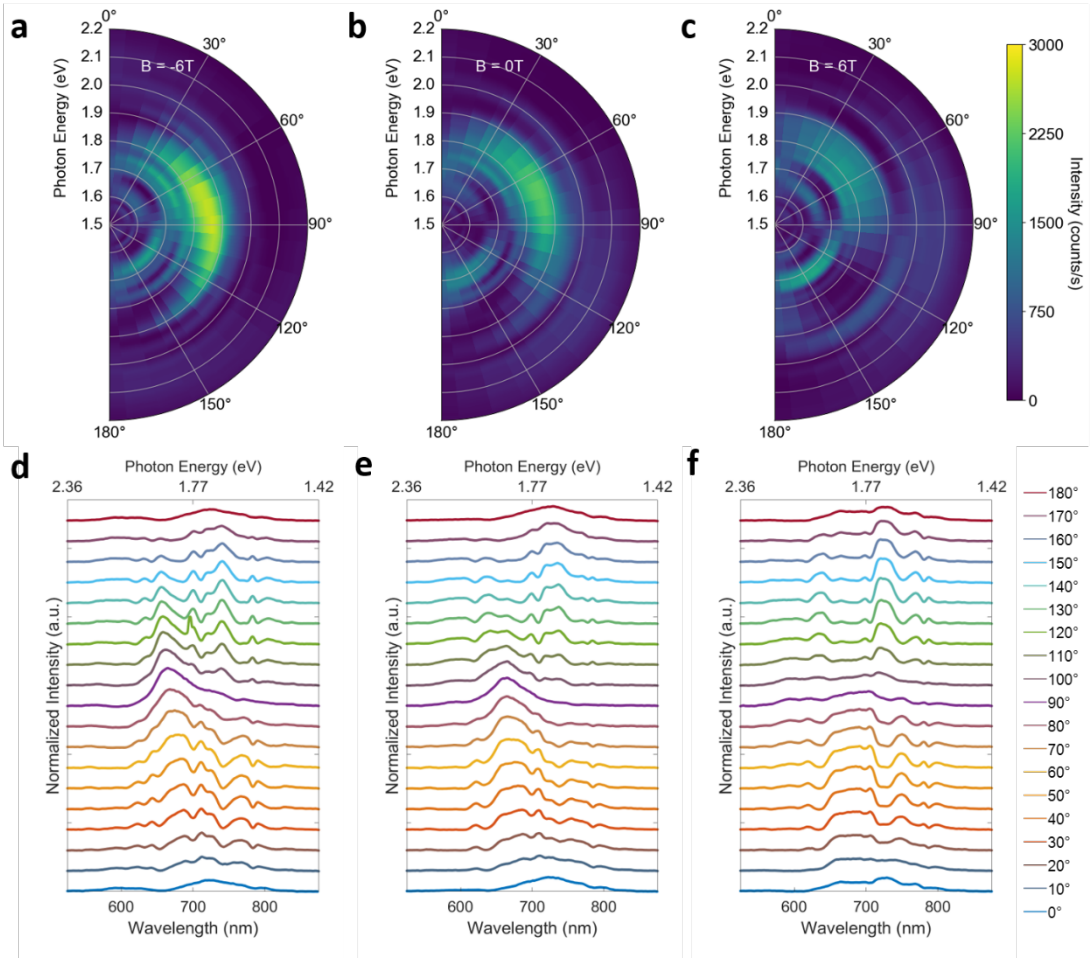

Figure 4-13: The EL spectra with different detected linear polarization using the same device as Figure 4-3. a-c, Polar plots of the EL spectra as a function of linear polarization under -6 T (a), 0 T (b) and 6 T (c). 0 degree is defined to be parallel to the nanowire (*y* direction) and 90 degree is perpendicular to the nanowire (*x* direction). d-e, The EL spectra at selected linear polarizations with applied field -6 T (d), 0 T (e) and 6 T (f). At each magnetic field, the spectra are distinct and change dramatically with the detected polarization angle, emphasizing the complicated character of the LSPRs.

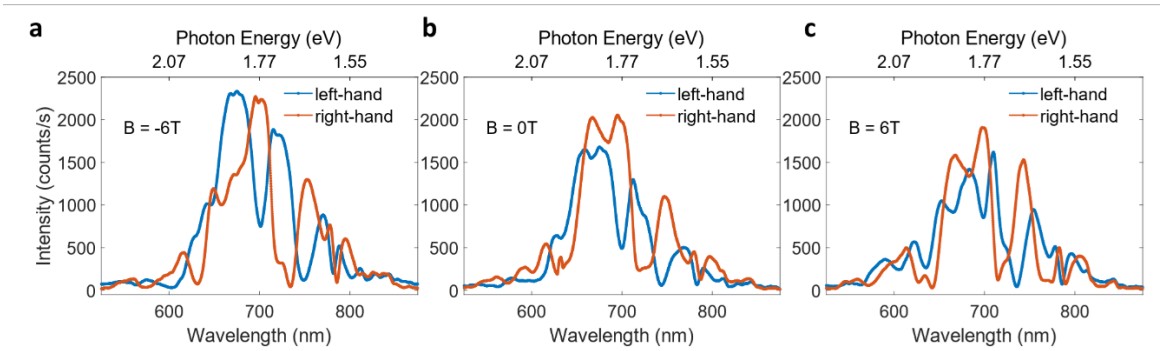

Figure 4-14: The EL spectra with detected circular polarization with applied field -6 T (a), 0 T (b) and 6 T (c). Clear circular dichroism can be observed at each magnetic field. Under different magnetic fields, the circular dichroism varies. The EL spectra with different emitted polarizations again imply that different sets of LSPR modes are excited under different magnetic field conditions.

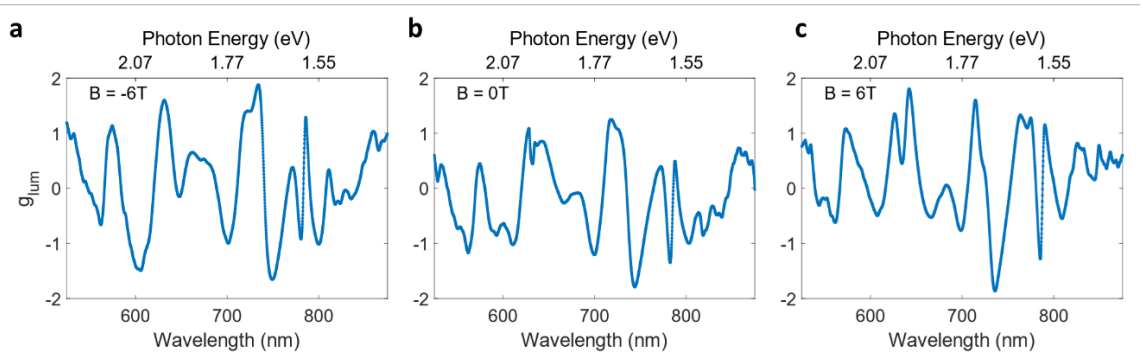

Figure 4-15: The dissymmerty factor of the circular polarized spectra with applied magnetic field -6 T (a), 0 T (b) and 6 T (c).

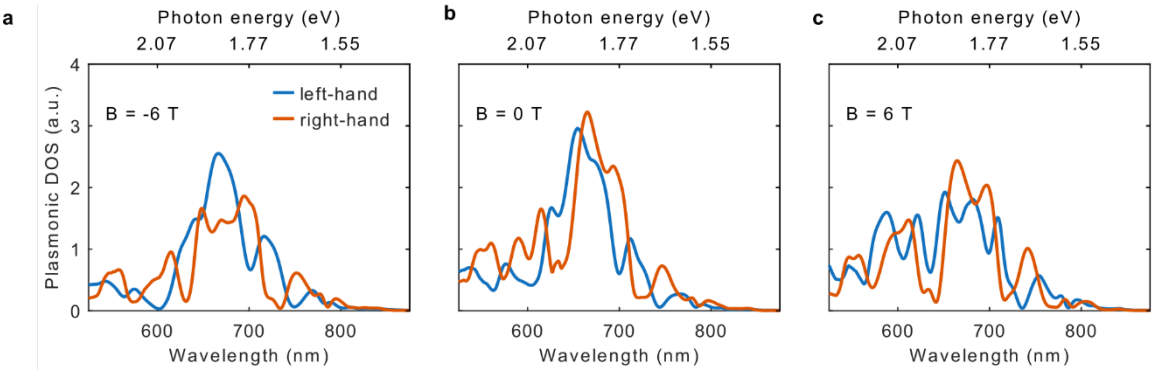

Figure 4-16: The extracted plasmonic DOS for far-field emission for the left-hand and right-hand polarization with applied field -6 T (a), 0 T (b) and 6 T (c).

4.6. EM model

As previously discussed, the MO response of bulk gold is far too weak to account for the pronounced magnetic field dependence observed in our EL. This discrepancy suggests that additional physical mechanisms beyond bulk metallic MO effects must be at play. We hypothesize that the large chiral effects observed experimentally arise from a combination of quantum tunneling and structural factors. On the one hand, the magnetic field modifies the electronic eigenstates in the metallic electrodes, $\psi_i(\boldsymbol{r}), \psi_j(\boldsymbol{r})$, thereby altering the transition dipole moments, $\boldsymbol{\mu}_{ij} \propto \int \boldsymbol{dr}\psi_i(\boldsymbol{r})\boldsymbol{\nabla}\,\psi_j(\boldsymbol{r})$, involved in the EL process. These modified transition dipole moments can acquire significant ellipticity, far exceeding bulk magneto-optic expectations. On the other hand, and crucially, their radiative characteristics are

strongly influenced by the plasmonic DOS at the nanogap. Asymmetric geometrical features at the junction sustaining highly confined and structurally chiral plasmonic modes are expected to amplify the influence of the applied magnetic field on the EL emission.

To test this hypothesis, we first numerically compute single-particle electronic eigenstates of the quantum wells modelling the electrode geometry under varying static fields. The potential landscape is given by square wells of depth given by the sum of the work function, Φ, and Fermi energy, E_F of gold. The effect of the magnetic field is accounted for by introducing the vector potential and employing the complete canonical momentum Hamiltonian, $\widehat{H} = \frac{\left(-i\hbar\nabla - q\vec{A}\right)^2}{2m}$. The eigenfunctions are determined within a rectangular region of approximately 250 nm^2 containing the nanogap. Since the system is biased under voltage V, we look for eigenstates around energies $E_F \pm eV/2$, on the left and right electrode respectively. From these, we extract the transition dipole moments for jumps between the left and right electrodes and express them in terms of their principal axes as:

$$\boldsymbol{\mu}_{ij} = \mu_{ij} \frac{\hat{u} + i\epsilon_s \hat{u}_\perp}{\sqrt{1+\epsilon_s^2}}, \quad (4-6)$$

where ϵ_s is the signed ellipticity parameter. Here, $\epsilon_s = 0$ ($\epsilon_s = \pm 1$) corresponds to linearly-polarized (left/right circularly polarized) dipole momenta, while intermediate values yield elliptically-polarized $\boldsymbol{\mu}$. More details of the transition dipole calculations and extra theoretical discussion can be found in Appendix G.

Figure 4-17a presents ϵ_s for dipole transitions between the 30 eigenstates nearest to the Fermi level of each electrode of the junction under different magnetic fields. At zero field (middle panel), $\epsilon_s = 0$ for all transitions and $\boldsymbol{\mu}$ is always linearly polarized. However, under ± 6 T fields (top and bottom panels), we observe substantial ellipticities. Notably, the sign of ϵ_s reverses with the magnetic field polarity, consistent with the expected behavior for the ellipticity of a classical point dipole.

To quantify these trends, we construct histograms $C_\mu(B)$ reflecting the distribution of transition dipole moments in magnitude and ellipticity. In order to better highlight the overall structure and influence of the magnetic field, in Figure 4-17b we display S, the averaged distributions for ±6 T ($S \equiv \left[C_\mu(6\text{T}) + C_\mu(-6\text{ T})\right]/2$), while Figure 4-17c highlights their difference ($D \equiv \left[C_\mu(6\text{T}) - C_\mu(-6\text{ T})\right]/2$), normalized to the overall counts. The asymmetry in these distributions reveals that positive magnetic field favors positive ellipticity, and vice versa, demonstrating the role of B in shaping the excitation landscape.

To assess the impact of the transition dipole ellipticity in far-field emission, we perform full-wave EM simulations by placing electric point-dipole sources with varying ϵ_s at the center of the junction geometry mimicking the experimental samples. The details of the simulation implementation can be found in Appendix H. The results shown in Figure 4-17d correspond to an asymmetric nanogap geometry. This configuration supports highly confined chiral modes, which are sensitive to the

dipole ellipticity and thus, the applied magnetic field, reproducing the phenomenology observed in the experiments. Note how even for moderate source ellipticity of $\epsilon_s = 0.3$, the chiral density of states at the gap is enough to result in a large modification of the radiated power spectra. For comparison, we also performed identical simulations using a symmetric nanogap in Figure 4-18, which exhibited negligible dependence on source ellipticity, highlighting the crucial role of structural asymmetry in the tunnelling junction enabling magnetically tunable EL. In our simulations, the spin-orbit coupling and electronic structure of gold are not involved, which suggests the large magnetic field dependent EL should be observed in other diamagnetic metallic plasmonic junctions. This agrees with the fact that the similar magnetic field dependent EL is observed in aluminum plasmonic junction as well (Figure 4-19).

Finally, although the average ellipticity across all dipolar transitions remains small, complying with the correspondence principle, our results reveal the importance of the local density of chiral optical states in confined nanogap systems, which can selectively amplify specific chiral transitions. Our simulations confirm that asymmetric nanojunctions can indeed support relevant chiral density of states, leading to pronounced differences in radiated power depending on dipole helicity.

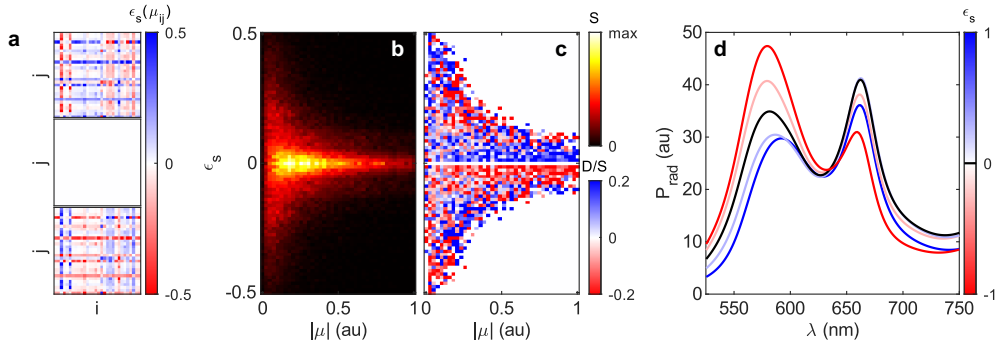

Figure 4-17: (a) Ellipticity of the transition dipole moments for jumps between eigenstate *i* of the left electrode and eigenstate *j* of the right electrode obtained for an applied magnetic field of -6 T (top), 0 T (middle) and 6 T (bottom). We show the values for the 30 eigenstates closest to the Fermi level of each electrode, spanning an energy range of approximately 80 meV. (b), (c) Statistical analysis of the transition dipole moments based on the histograms $C_\mu(B)$, which count the number of transitions found with a certain ellipticity, and transition dipole module for a given magnetic field. In b we show $S \equiv (C_\mu(6\ \mathrm{T}) + C_\mu(-6\ \mathrm{T}))/2$, while in c we display $D \equiv (C_\mu(6\ \mathrm{T}) - C_\mu(-6\ \mathrm{T}))/2$, normalized to S, highlighting the fluctuations due to the change of magnetic field. (d) Radiative density of states for a linear (black), and circularly polarized point dipoles ($\epsilon_s = \pm 1$). Colored curves represent the spectra for source ellipticities of $\epsilon_s = \pm 0.3$.

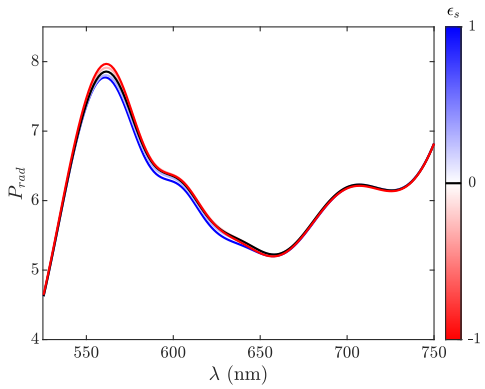

Figure 4-18: Radiation power of an elliptically polarized source in presence of a symmetric junction. The spectrum is virtually unmodified for all different dipole ellipticities.

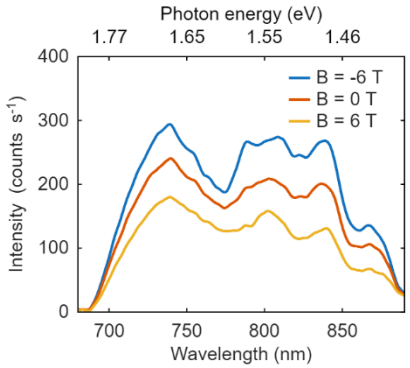

Figure 4-19: The EL spectra at $\pm$ 6 and 0 T magnetic field of the aluminum device. The bias voltage is 1.8 V and the tunneling current is about 380 nA. The similar asymmetric change in both the amplitude and shape of the spectra can be observed. This supports that the magnetic tuning of EL is general for diamagnetic plasmonic junctions, not only for gold devices.

4.7. Summary

In summary, we experimentally show that the EL spectra of plasmonic nanojunctions can be dramatically modulated by an external magnetic field of a few Teslas. The plasmonic DOS and hot carrier effective temperature extracted from a normalization analysis shows that the far-field radiation by the LSPRs excited by the tunneling current is magnetic-field dependent, which is further supported by the polarized EL spectra. Gold MO models fail to explain the observed results, implying the quantum-tunneling origin of the large magnetic sensitivity. The ability to tune LSPR-based electroluminescence with external magnetic fields opens the possibility of novel optoelectronic devices. Single-nm scale control over nanogap geometry would enable the engineering of on-chip light sources and the polarization of their emission, while providing foundational insights into the relationship between light emission, geometric chirality and magnetism.

Chapter 5

Understanding the Local Seebeck Coefficient of Carbon Nanotube Fibers Using the Photothermoelectric Effect

In this chapter, I will discuss the project of probing the variation of the Seebeck coefficient of CNTFs using the PTE effect. This chapter is based on the publication Ref.[167] "Understanding the Local Seebeck Coefficient of Carbon Nanotube Fibers Using the Photothermoelectric Effect". The CNTFs are grown by Dr. Lauren W. Taylor, Dr. Oliver S. Dewey and Dr. Matteo Pasquali. The devices are fabricated under the help of Shengjie Yu and Dr. Junichiro Kono. The thermal model and thermal property measurements are done by Dr. Yingru Song and Dr. Geoff Wehmeyer.

5.1. Motivation

CNTFs are promising candidates for thermoelectric active cooling materials thanks to their unique combinations of electrical and thermal properties.[105,106] As the synthesis and fabrication of CNTFs have improved, CNTFs are reported to have a giant

thermoelectric power factor as large as 14 ± 5 mW m^{-1} K^{-2} at room temperature,[168] which is the highest value for any CNT system and approaches the highest values reported for 2D materials.[169,170] The outstanding electrical properties and thermoelectric response are typically discussed and investigated at the scale of the macroscopic fiber (~centimeter scale lengths or longer). However, due to the inherent microstructure, defects and imperfections of the fibers introduced during fabrication, the local properties at different positions can deviate from the average values. At present there is a relative lack of data on the variation of local properties along the fibers, though there have been some examinations of chemical heterogeneity[171] and mechanical properties[172] by nanoscale imaging.

Several reports have previously probed the variation of the Seebeck coefficient of CNT films[173] and bundles,[174] and photodetectors can be made of CNTs based on the PTE effect.[175–177] In this project, we apply this approach to high quality CNTFs, providing mechanistic insight on the Seebeck coefficient variation along the fiber, with spatial resolution of micrometers. This local assessment is essential to understanding and optimizing CNTF properties and their origins.

5.2. Device fabrication

The CNTFs in this study are very similar to the CNTFs reported in reference,[168] comprising double-wall CNTs, with average outer-wall and inner-wall diameters of

1.8 ± 0.2 nm and 0.9 ± 0.1 nm respectively. The CNT length to diameter aspect ratio is 3600 ± 80, measured via extensional viscosity.[178] Continuous fibers are fabricated by a solution spinning method.[107,179,180] A SEM micrograph of the fiber is shown in Figure 5-1A. The CNTs within the fiber are densely packed and highly aligned, comparable to the CNTFs in reference.[179] The average diameter of the fiber is measured to be 17.5 μm from a cross-section view. The Raman spectra of the fiber are also measured, as shown in Figure 5-2. The Raman G-to-D ratio is 50 at 532 nm laser excitation for the common G and D modes observed in CNTFs[107,168], implying a low defect density, and the low frequency radial breathing modes (RBM) position is consistent with the CNT diameters.[181] As-made, these fibers are highly electrically conductive (~8 MS/m at room temperature) and are known to be strongly *p*-type doped by the remnant acid in the fiber.[168,179]

A 1-2 mm piece of the fabricated CNTFs is cut to make a device. A photograph of a typical device is shown in Figure 5-1B. All the devices are fabricated on Si wafers with a 2 μm thick SiO2 layer. Gold contact pads with Ti adhesion layer are evaporated, and the fiber is connected to the Au pads by silver paste. The device is wire bonded at the Au pads for electrical measurements.

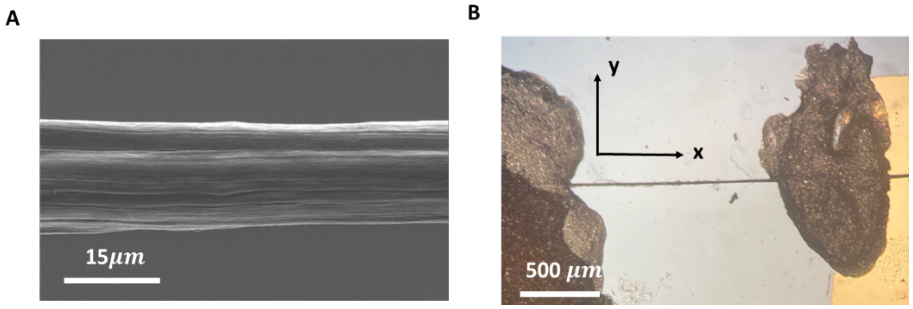

Figure 5-1: (A) SEM micrograph of the solution-spun CNTF. The CNTs in the fiber are densely packed and highly aligned. The average diameter of the fiber is 17.5 µm. (B) Optical micrograph of the device. The fiber is supported on a SiO2/Si substrate. The fiber is connected electrically to gold pads by silver paste.

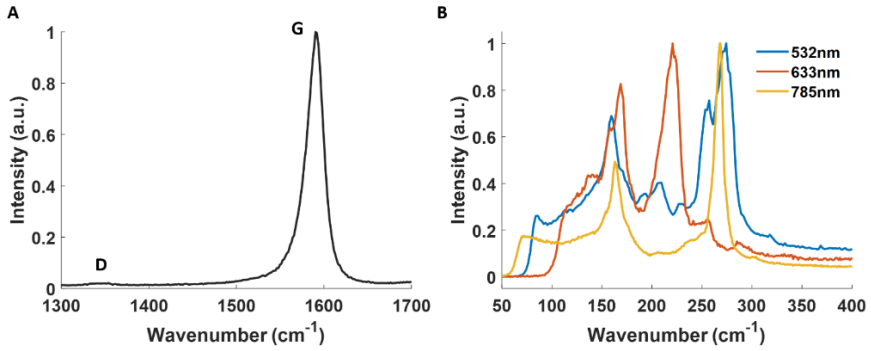

Figure 5-2: Raman spectra of the CNTFs. (A) Raman D and G band of the fiber. The G-to-D ratio is about 50, suggesting low density of defects. The Raman spectrum is acquired with 785 nm excitation laser. (B) The low frequency RBM of the fiber. The spectra are acquired with 532, 633 and 785 nm excitation laser.

The diameter of the CNTs estimated from the RBM is consistent with the real values.[168]

5.3. CNTF PTE measurement setup

The experiment setup for the PTE measurements is shown in Figure 5-3. We use a 1060 nm diode laser as the excitation source. The laser is modulated by an optical chopper and focused at the fiber by a Zeiss 100× objective with 2.5 μm laser spot ($1/e^2$ radius). The intensity of the laser is controlled by a half wave plate (HWP) and a polarizer. Another HWP controls the polarization angle, θ, the angle between laser polarization and x direction. The photovoltage is first amplified by a SR 560 voltage preamplifier and then measured by an Ametek 7270 lock-in amplifier synced to the chopper. The device can be moved in the x and y directions with two Thorlabs DRV001 stepper motors, so the map of photovoltage can be obtained by scanning the excitation laser over the x-y plane with user-defined pixel size. The spatial resolution of the measurement is limited by the laser spot size and the step size of the motors. All measurements are taken under ambient conditions at room temperature.

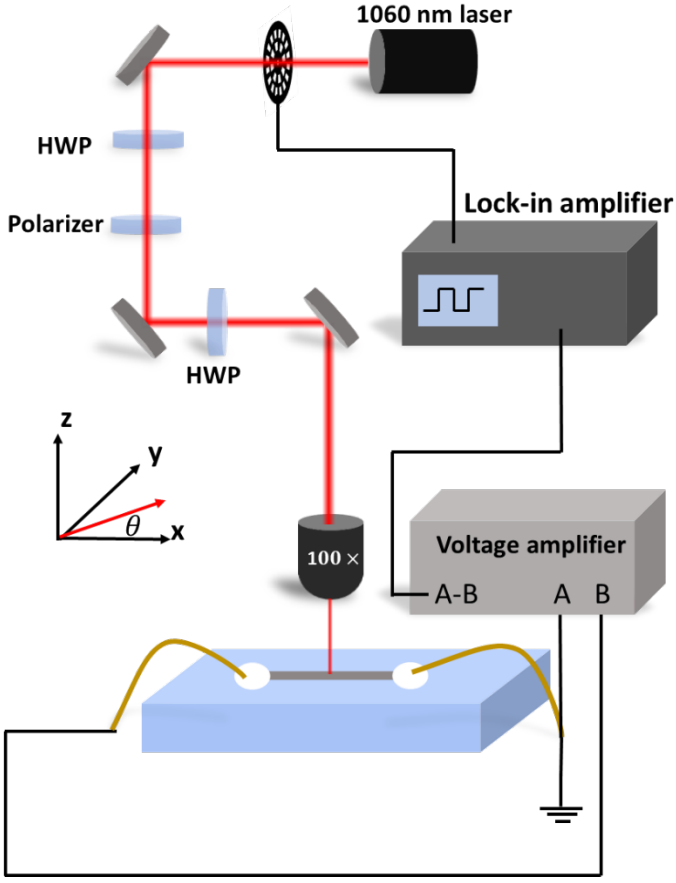

Figure 5-3: Schematic of the photovoltage measurement setup. The polarization angle of the incident 1060 nm light is θ relative to the x direction.

5.4. PTE origin of the photovoltage

First, the laser spot position is fixed at the center of fiber and the photovoltage is measured with different excitation laser power, as shown in Figure 5-4A. The photovoltage is linearly proportional to the input power, consistent with previous PTE investigations.[176,182] Therefore, the photovoltage is normalized by the laser power is the following discussion. To confirm the thermal origin of the photovoltage,

we measure the photovoltage as a function of the chopper time period, as shown in Figure 5-4B. When the chopper period is short, the thermal quasi-steady state is not yet established, and the temperature rise does not reach its maximum value before the laser is blocked. As a result, the photovoltage is small. When the chopper period increases, the system has more time to respond and the temperature rise is larger, so the photovoltage increases. At sufficiently long periods, thermal steady-state is reached during the illumination and the temperature rise is maximized, leading to saturation of the photovoltage. The exponential fitting of the photovoltage as a function of the chopper period (dashed line in Figure 5-4B) gives a thermal time constant on the order of milliseconds, consistent with the previous PTE results.[174,176,182] This confirms that the photovoltage is due to the PTE effect rather than a photovoltaic effect, as such a purely electronic mechanism has time scales that are on the order of picoseconds.[183] The photovoltage also shows a slight laser polarization dependence, as shown in Figure 5-4C. The photovoltage is slightly smaller when the laser polarization is perpendicular to the fiber axial direction ($\theta = 90°$) than the laser polarization is parallel to the fiber ($\theta = 0°$) with the ratio to be 0.85. This angle dependence is consistent with the high alignment of single CNTs along the fiber.[175,177,184]

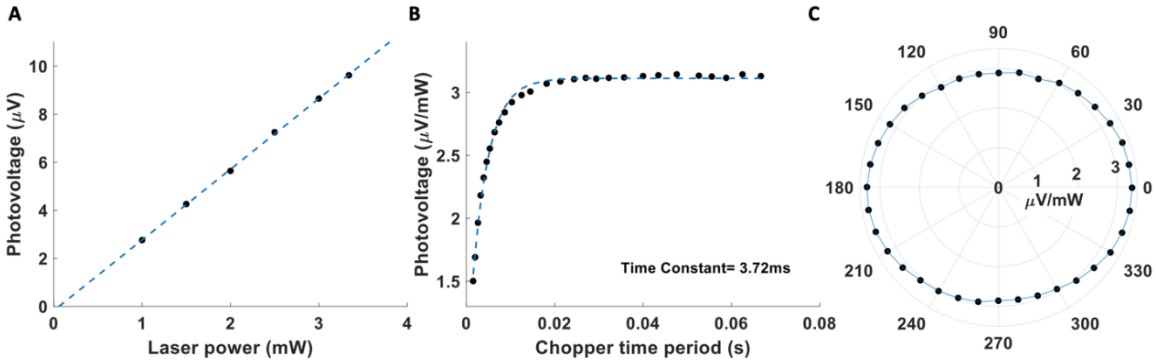

Figure 5-4: (A) The PTE voltage (points) scales linearly with the laser power. The blue dashed line is the linear fit. (B) The normalized PTE voltage measured as a function of chopper time period. The blue dashed curve is the exponential decay fit, which gives the time constant to be 3.7 ms. The millisecond time scale confirms that the voltage is from the PTE effect rather than a photovoltaic effect. (C) Laser polarization dependence of the PTE voltage. The voltage is the largest when the polarization is parallel to the axial direction (θ=0°), and the voltage is the smallest when the polarization is perpendicular to the axial direction (θ=90°). Line is interpolation.

5.5. Numerical extraction of the Seebeck coefficient

As discussed in Chapter 2, the photovoltage $V(x_0)$ when the laser is at position x_0 on the fiber can be written as:

$$V(x_0) = -\int_0^L S(x)\nabla T(x, x_0)dx \quad (5-1)$$

The Seebeck coefficient of the fiber $S(x)$ is a function of position along the fiber, and the temperature gradient $\nabla T(x, x_0)$ is a function of both laser position and position along the fiber. In the map measurements, the fiber is discretized into different pixels. Within each single pixel, the properties of the fiber are considered to be uniform. The photovoltage $V(x_j)$ when the laser is at pixel j on the fiber can be written as:

$$V(x_j) = -\sum_{i=1}^{N} S_i \cdot \nabla T_i(x_j) \cdot \frac{L}{N} \quad (5-2)$$

where N is the total pixel number, L is the length of the fiber, S_i and $\nabla T_i(x_j)$ are the Seebeck coefficient and the temperature gradient at pixel i respectively when laser is shining on pixel j. $V(x_j)$ is measured in the PTE map. The $\nabla T_i(x_j)$ matrix can be obtained from the thermal model. More details about the thermal model can be seen in the next section and **Appendix C.**

We can re-write the equation above in the matrix form as:

$$\begin{pmatrix} \nabla T_1(x_1) & \cdots & \nabla T_N(x_1) \\ \vdots & \ddots & \vdots \\ \nabla T_1(x_N) & \dots & \nabla T_N(x_N) \end{pmatrix} \cdot \begin{pmatrix} S_1 \\ \vdots \\ S_N \end{pmatrix} = -\frac{N}{L} \cdot \begin{pmatrix} V(x_1) \\ \vdots \\ V(x_N) \end{pmatrix} \quad (5-3)$$

The ∇T matrix has a rank of N-1 (details in the next section), so the general solution of the equations $S_i = S_{i,\mathrm{rel}} + S_{\mathrm{ave}}$. S_{ave} is the solution of the homogeneous linear equations $\nabla T \cdot S = 0$. S_{rel} is a particular solution of the above inhomogeneous linear equations.

Consider the symmetric boundary condition of the temperature, for a perfectly uniform fiber ($S(x)$ is an position-independent constant), we have: $V(x_0) = -\int_0^L S(x)\nabla T(x, x_0)dx = -S\int_0^L \nabla T(x, x_0)dx = S\big(T(x=0) - T(x=L)\big) = 0$. As a result, $S_{\text{ave}} = C(1,1,\dots,1)^T$, where C is a constant. S_{rel} can be numerically solved by $S_{\text{rel}} = -\frac{N}{L}\cdot \nabla T^{-1}V$, where ∇T^{-1} is the Moore-Penrose pseudoinverse of the matrix ∇T. The constant C can be obtained by setting the average of the Seebeck coefficient S_i to be the experimentally measured average Seebeck coefficient of the fiber, as described in the next section and **Appendix C**. In this case, the Seebeck coefficient as a function of position S_i is the summation of the average Seebeck coefficient S_{ave} of the whole fiber and the position-dependent relative Seebeck coefficient $S_{i,\text{rel}}$, which has 0 mean value. The total Seebeck coefficient describes a position-dependent fluctuation around the average value.

Filtering the photovoltage data is useful in reducing the noise in the extracted Seebeck coefficient. Because the ∇T^{-1} matrix has very large eigenvalues numerically, the noise in V will be amplified by $\nabla T^{-1}V$. In extracting the Seebeck coefficients used throughout this work, we use the smoothed data instead of the raw data of V. The robustness of the extraction of the Seebeck coefficient are discussed in detail in **Appendix D**.

5.6. Thermal model and CNTF thermal property measurements

A thermal model is needed to solve the temperature profile in PTE measurements and extract the Seebeck coefficient.

5.6.1. Derivation of PTE temperature profile

We consider one-dimensional (1D) steady-state heat conduction in the axial x direction of the CNTF due to point source heating from a laser beam. Because this heating period is substantially larger than thermal time constant (Figure 5-4B), transient heat conduction effects are negligible, and the steady-state model is appropriate to describe the amplitude of the temperature rise. A sketch of the thermal model is shown in Figure 5-5A. The 1D governing energy equation including radiation, convection and thermal contact resistance that is used to find the steady-state temperature profile $T(x)$ is:

$$\frac{\mathrm{d}^2T}{\mathrm{d}x^2} = m^2(T - T_0) \quad (5-4)$$

where $m^2 \equiv \frac{1}{kA}\left(\pi Dh + \frac{1}{R_{\mathrm{contact}}}\right)$ describes the effect of the losses to the surroundings, k is the fiber axial thermal conductivity; A is the fiber cross-sectional area; D is the fiber diameter; h is the heat transfer coefficient describing the combined effects of convection to the nearby air and radiation to the surroundings; R_{contact} is the thermal contact resistance for a unit length between the CNTF and the silicon substrate (units of $\mathrm{K.m/W}$); and T_0 is the ambient temperature. To simplify the mathematical

expressions, the origin of the coordinate is set at the center of the fiber in the thermal model (Figure 5-5A) and boundaries are at $\pm L/2$. The fiber can be divided into the left regime defined over a range from $[-\frac{L}{2}, x_0)$ and the right regime defined over a range from $(x_0, \frac{L}{2}]$. The analytical solution of the governing equation is:

$$\Delta T_{left}(x) = C_1\, exp(mx) + C_2\, exp(-mx) \quad (5-5)$$

$$\Delta T_{right}(x) = C_3 exp\,(mx) + C_4 exp\,(-mx) \quad (5-6)$$

where C_1, C_2, C_3, C_4 are constants. More details of the derivation are discussed in **Appendix C**. With the temperature profile Eq. (5-5) and (5-6), we can analytically find the temperature gradient profile as:

$$\nabla T_{\text{left}}(x) = C_1\, mexp(m(x - L/2)) - C_2 mex\, p\left(-m\left(x - \frac{L}{2}\right)\right) \quad (5-7)$$

$$\nabla T_{\text{right}}(x) = C_3\, mexp(m(x - L/2)) - C_4 mex\, p\left(-m\left(x - \frac{L}{2}\right)\right) \quad (5-8)$$

Eq. (5-7) and (5-8) calculate the temperature gradient on the left and right side of the laser spot x_0 . The temperature gradient at $x = x_0$ is set to 0 considering the temperature profile is highly symmetric near $x = x_0$ (see Figure G-1 in Appendix G), so the PTE voltage originates from the left and right region near $x = x_0$ cancels out. In other words, the diagonal elements of the $\nabla T_i(x_j)$ matrix in Eq. (5-3) is set to 0, and the off-diagonal elements are determined by Eq. (5-7) and (5-8).

5.6.2. Characterization of fin parameter mL in the PTE experiment

The PTE measurements are performed in an open environment at room temperature. In this case, the convection, radiation and heat conduction across the fiber-substrate interface are not negligible and are required accurate characterization, as shown in Figure 5-5B. We have utilized a steady-state Joule heating and resistance thermometry method to find the fin variable m. The CNTF samples are laid on the identical SiO_2/Si substrate as used in the PTE measurements to make sure the contact resistance is consistent, and measurements on multiple samples yield consistent values. The detailed analytical derivation of the steady-state Joule heating method, and the measured fin variable m values can be found in **Appendix C.**

5.6.3. Thermal conductivity measurements

The thermal conductivity of the CNTF samples are the input parameters to the PTE measurements and characterization of the fin variable m. Prior to any measurement, we use Joule heating (steady state and three-omega) measurements to evaluate the thermal conductivity of the CNTF. In this experiment, the CNTF sample is suspended over the inner two silver paste electrodes and the measurements are performed in the vacuum chamber to prevent convection and conduction through the substrate, as shown in Figure 5-5C. The detailed descriptions of the experimental setup and measured thermal conductivity can be found in **Appendix C**.

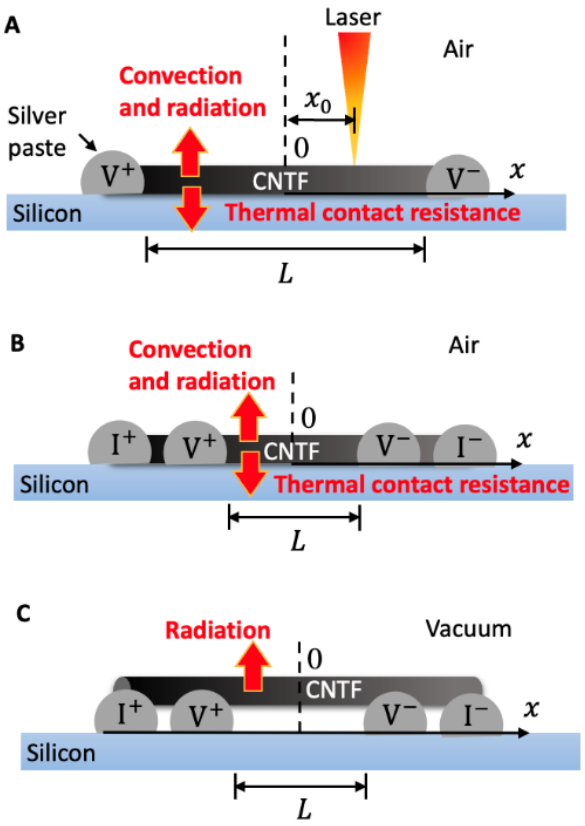

Figure 5-5: Illustrations of CNTF thermal experiments. (A) PTE measurement for supported CNTF in air with local laser heating at location $x = x_0$ and open-circuit voltage measurement. (B) Fin parameter measurement for supported CNTF in air. This fin parameter measurement uses position-independent Joule heating and resistance thermometry to find the fin parameter mL used in the analysis of the PTE measurements shown in (A). (C) Thermal conductivity measurement for suspended CNTF in vacuum using Joule heating and resistance thermometry.

5.6.4. Average Seebeck coefficient measurements

To obtain the average Seebeck coefficient S_{ave}, we have performed the standard steady-state measurements on both as-spun and annealed CNTFs. The CNTF samples are suspended over two heat-sunk Peltier modules which controls the temperature difference between both ends of the CNTF, as shown in Figure 5-6. The measured average Seebeck coefficients are 17.2 ± 0.9 μV/K for as-spun CNTF and 21.0 ± 0.3 μV/K for 423 K annealed CNTF. Details of the steady-state average Seebeck measurement and the data analysis are discussed in **Appendix C**.

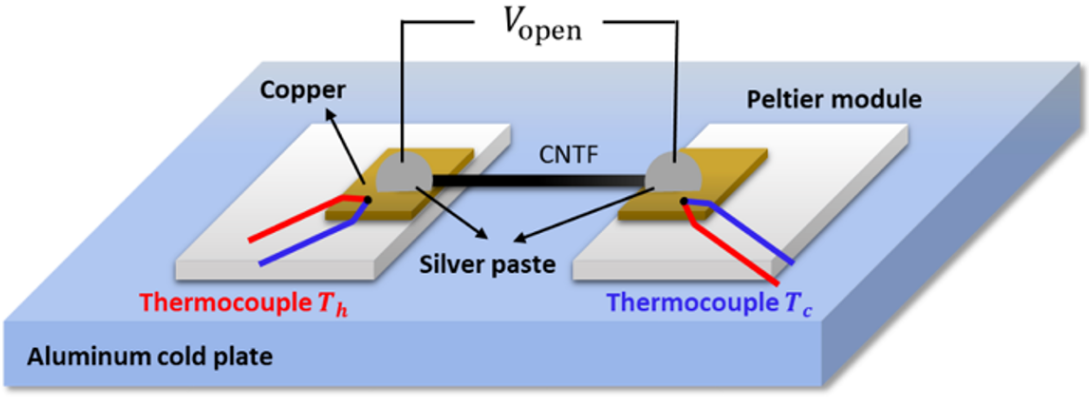

Figure 5-6: Schematic of standard steady-state average Seebeck measurements.

Some thermal parameters of the as-spun and 423 K (150 ℃) annealed CNTFs are shown in Table 5-1. With the values of these thermal parameters, the temperature and temperature gradient profiles can be obtained. Figure 5-7A shows an example of the temperature profile of the CNTF with 3 mW laser power at different x_0 position. Here, we set the origin of the coordinate to be the left end of the fiber to be consistent with the experiment. The ambient temperature T_0 is 293 K. Figure 5-7B shows the temperature gradient of the CNTF at different x_0 position based on Figure 5-7A.

CNTF indicator	Temp. coefficient β (ppm/K)	Electrical conductivity σ (MS/m)	Thermal conductivity k (W/m.K)	Fin variable m (m^{-1})
CNTF (as-spun)	2310±25	6.7±0.5	240±20	$2.5 \pm 0.2 \times 10^3$
CNTF (150 ℃ annealed)	2880±30	3.6±0.30	290 ±30	$3.0 \pm 0.3 \times 10^3$

Table 5-1. Measured quantities extracted from CNTF thermal experiments.

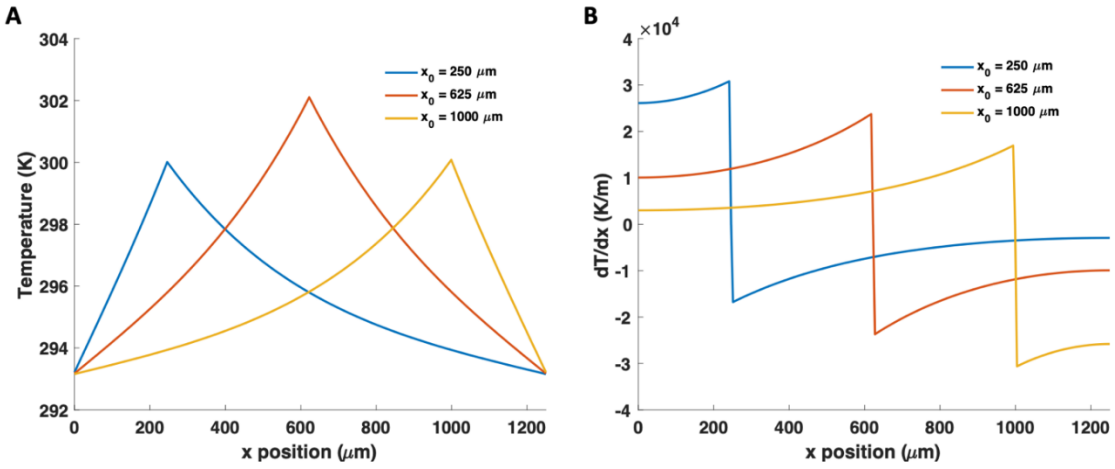

Figure 5-7: (A) The temperature profile along the CNTF with different laser spot position x_0 obtained from the thermal model. (B) The temperature gradient based on (A) along the fiber. The laser power is 3 mW.

5.7. PTE and Raman spectrum data on a locally annealed CNTF

We demonstrate the Seebeck coefficient extraction methodology with different types of fiber samples. The PTE map measurements and the Seebeck coefficient calculation are first performed on a fiber with a distinct feature in the Seebeck coefficient distribution deliberately introduced by localized laser annealing. It is known that thermal annealing of CNTF can de-dope the material by evaporating the remnant acid and/or other adsorbed dopants such as water vapor, and that this de-doping reduces their electrical conductivity and increases their average Seebeck response.[168,185] A high power (50 mW) 785nm laser is focused at the center of the fiber for 10 s, as shown in Figure 5-8A. Induced by the laser, the temperature is

increased to about 516 K (243 ℃) at the center based on our thermal model (**Appendix E**); this temperature rise is much larger than the temperature rises induced by the low-power (<3 mW) laser used in the PTE measurements. We expect the fiber to undergo modest dedoping by the brief exposure to elevated temperatures, resulting in an increase in the Seebeck coefficient near the center of the fiber within the heat-affected zone.

The PTE voltage maps of the device before and after laser annealing are measured, as shown in Figure 5-8B. Figure 5-8C shows the PTE voltage as a function of x_0 position obtained by finding the maximum of the absolute value in each y-column in the PTE voltage maps in Figure 5-8B. Before annealing, the PTE voltage is small but non-zero, implying a non-uniform distribution of the Seebeck coefficient along the unannealed fiber. After laser annealing, we observe a large difference in the magnitude of the PTE voltage over the whole fiber. The Seebeck coefficient of the fiber both before and after annealing is calculated, as shown in Figure 5-8D. Before annealing, the Seebeck coefficient fluctuates around the 17.2 μV/K average value. After annealing, we observe an overall increase in the Seebeck coefficient from $x = 350 \sim 850$ μm. At the center location of $x \approx 620$ μm near the laser absorption location during annealing, the Seebeck coefficient increase by ~30%, to about 22.4 μV/K. The steady state temperature profile during laser annealing is also simulated (**Appendix E**) in Figure 5-8D to help explain the increase in the Seebeck coefficient: near the edge of the fiber ($x < 350$ μm and $x > 850$ μm), the temperature rise is low and it is insufficient to dedope the fiber or cause the increase in the Seebeck

coefficient. In the range of $x = 350 \sim 850$ μm, the temperature rise is larger and leads to the measurable increase in the Seebeck coefficient. At the center, the temperature increases steeply to 516 K, which results in the increase of the Seebeck coefficient from about 19.5 μV/K to 22.4 μV/K in a short range of $x = 590 \sim 650$ μm.

We measure the Raman spectra of the fiber at $x \approx 620$ μm using 532 nm excitation before and after the laser annealing, as shown in Figure 5-8E. The spectra show a large red shift (17 cm^{-1}) of the 2D band and a qualitative change of the line shape of the G band after annealing. A broad G^- band at about 1520 cm^{-1} appears after annealing, and there is a 3 cm^{-1} red shift in the G^+ band.

Here, we give a brief explanation of the Raman spectra in CNTs: the Raman G and 2D bands are present in all sp^2 carbon structures. The G band is the in-plane bond stretching mode of the C-C bonds in the hexagonal lattice. The 2D band is related to the vibrational mode of the breathing of the six-carbon ring in the hexagonal lattice. The C^{13} isotope and strain information can be obtained from the shifts and linewidth of the G and 2D bands.[186–189] They can also be used to probe the position of the Fermi energy and the doping level because of the electron-phonon coupling of the metallic sp^2 structures.[185,190–194]

In pristine graphene, the G band is a single Lorentzian peak. In CNTs, due to the curvature of the tubes, the G band split into G^- and G^+ bands. Before annealing, the G^- and G^+ bands of the fiber (consisting of both metallic and semiconducting CNTs) are very close to each other, so the G band looks like a single Lorentzian peak. After

annealing, the Fermi energy of the metallic CNTs shifts towards closer to the band edge. An intermediate electron-hole pair is formed near the Fermi energy with the assistance of the phonon due to the electron-phonon coupling, and the perturbation of the phonon by electron-phonon interaction makes the phonon energy lower and the lifetime shorter.[191,192,194] As a result, the broadening and red shift of the G^- band in metallic CNTs can be seen after annealing. Before annealing, the Fermi energy of the metallic CNTs is high and the electron-hole excitation is blocked by Pauli principle, so the red shift and broadening of the G^- band do not occur.[192,194] In semiconducting CNTs, the energy gap between the valence and conduction band is much larger than the phonon energy, so the electron-phonon coupling doesn't happen. There's also report that the red shift and broadening of the G^- band only occur in metallic but non-armchair CNTs.[195] The Raman spectrum of the laser annealed sample in Figure 5-8E shows a substantial shift of the 2D band. The 2D band is reported to red shift when the doping level decreases because of the electron-phonon coupling, similarly with the G band.[193]

The Raman spectra are also measured at each pixel along the fiber after laser annealing. The 2D band position and G^-/G^+ ratio as a function of x position are shown in Figure 5-8F and G. The red shift of the 2D band and the increase in G^-/ G^+ ratio can be seen at the center of the fiber. Comparing Figure 5-8E, F and G, we can see the 2D band red shift and the increase of G^-/ G^+ are more localized than the increase of the Seebeck coefficient. From $x = 350 \sim 590$ μm and $x = 650 \sim 850$ μm, the Raman spectra remain the same while the Seebeck coefficient increases. Combining the

temperature profile during the laser annealing in Figure 5-8D, we can estimate the required temperature to see the Raman spectrum changes is about 460 K (287 °C).

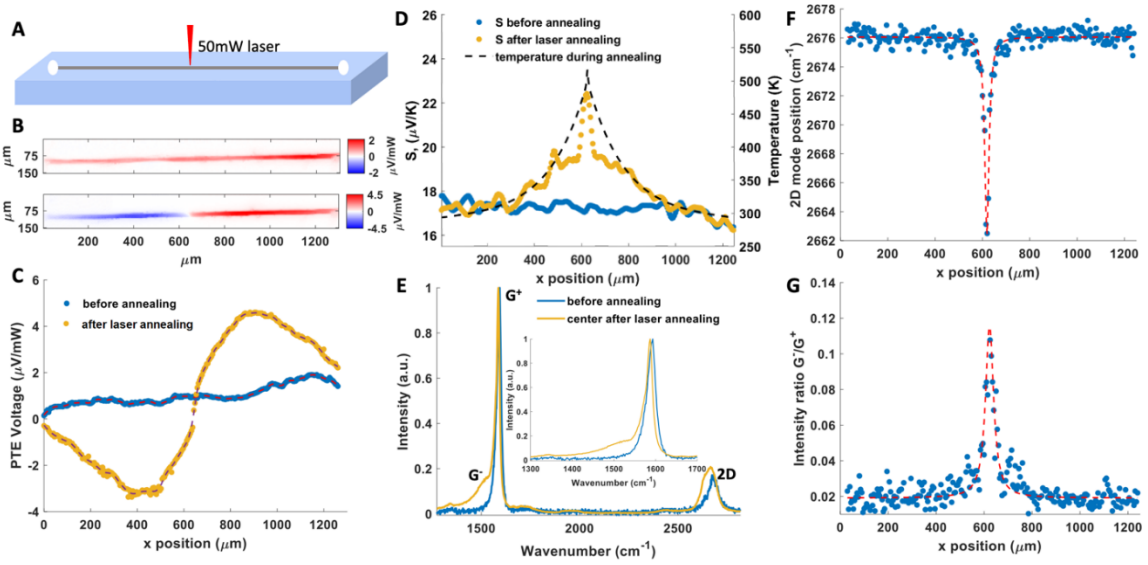

Figure 5-8: (A) Diagram of the laser annealing configuration. A 785 nm 50 mW laser irradiates the center of the fiber for 10 s to induce de-doping and modify $S(x)$. (B) The PTE map measurements of the device before (top) and after (bottom) the laser annealing. (C) The PTE voltage as a function of x_0 position along the fiber before (blue) and after (yellow) the laser annealing. The PTE voltage is obtained from the map in (B). The dashed lines are the smooth curves fit to the PTE voltage and used to extract S. The magnitude of the PTE voltage is much larger after the local laser induced annealing. (D) Left axis: calculated Seebeck coefficient as a function of x position before and after annealing. Right axis: simulated steady state temperature during the laser annealing. (E) Raman spectra of the fiber at $x \approx 620$ μm before and after the laser annealing show a red shift in the 2D band position and modified line shape of the G band. Inset: the spectra from 1300-1700 cm^{-1} including the G band. (F) The Raman 2D band peak position as a function of x position of the laser annealed fiber. The red shift can be clearly seen at $x \approx 620$ μm. (G) The Raman intensity ratio between

the G^- and G+ bands as a function of x position of the laser annealed fiber. The broad G^- band appears at $x \approx 620$ μm. The red dashed curves in (F) and (G) are lines to guide the eyes. Comparing the Raman spectra and the Seebeck coefficient, we confirm the increase in the Seebeck coefficient is caused by the shift of the doping level by the laser annealing.

5.8. Effect of global thermal annealing on CNTFs

We also measure the PTE map to investigate the Seebeck coefficient variation along a piece of the same fiber before and after a global thermal annealing. Focusing first on the pristine fiber, the PTE voltage is shown in Figure 5-9A (blue curve), and the extracted Seebeck coefficient profile is shown in Figure 5-9B (blue curve). The Seebeck coefficient fluctuates around the 17.2 μV/K average value and the standard deviation and range are 0.30 and 1.25 μV/K, respectively. To gain insight into the origins of the spatial variation, the whole fiber is annealed in a furnace with pressure below 100 mTorr for 4 hours at 423 K (150 °C) (a thermal cycle determined not to harm the silver paste contacts). The PTE map measurement is performed again on the fiber, and then the Seebeck coefficient is calculated, as shown by the orange curves in Figure 5-9A and B respectively. After annealing, the average Seebeck coefficient is measured via global thermopower to be 21.0 μV/K. Our finding in Figure 5-9B shows the spatial fluctuations are much smaller after annealing, with the standard deviation and range to be 0.13 and 0.72 μV/K.

Raman measurements are consistent with these PTE observations as well. The average Seebeck coefficient becomes larger after annealing because of the overall de-doping of the CNTF. The Raman spectra measured before and after annealing at 423 K for 4 hours, as shown in Figure 5-9C, show that the G band red shifts about 3 cm^{-1}, consistent with de-doping of the fiber. However, unlike the laser annealing sample, the 423 K annealed sample shows no detectible shift in the 2D band. This finding is consistent with the result from Figure 5-8F and shows that an annealing temperature of 423 K is not large enough to result in a 2D band shift.

Given that the modest 423 K annealing temperature is unlikely to introduce changes in structural arrangement or the strain of the fiber, the smaller fluctuation of the Seebeck coefficient after annealing suggests that the spatial variation in $S(x)$ likely originates from nonuniformities in the dopant concentration. We therefore attribute the lower spatial variation in $S(x)$ to a more uniform distribution of the doping level along the fiber for remaining dopant in the fiber. Modeling the Seebeck coefficient fluctuation as caused the by non-uniform doping level, we can estimate the Fermi energy E_F as a function of position, as shown in Figure 5-9B right axis. This model uses the same correlation between the Seebeck coefficient and the Fermi energy described in a previous report[168] on these fibers. The Fermi energy of the fiber before and after annealing estimated from this model is -0.465 eV and -0.459 eV, and we can see fluctuations at the scale of 1 meV. Considering the 3 cm^{-1} shift in the G band of the Raman spectra (Figure 5-9C), we can estimate that at least a resolution of $3\ cm^{-1}/\ 0.006\ (eV)\ =\ 0.5\ cm^{-1}$is needed for the Raman spectroscopy to probe the

Fermi energy fluctuation in 1 meV. However, the 0.5 cm^{-1} spectral resolution is not available for most commercial Raman spectroscopy systems. Our PTE effect-based method can therefore detect finer variation of S and E_F along the fiber compared with the Raman spectroscopy.

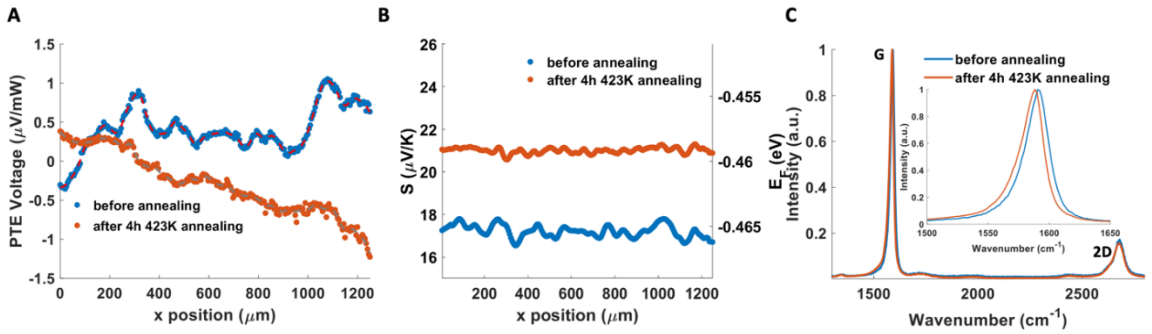

Figure 5-9: (A) The PTE voltage as a function of x_0 position along the fiber before and after annealing at 423 K for 4 hours in the furnace. The red and gray dashed lines are the smooth curves for the PTE voltage. (B) The calculated Seebeck coefficient and Fermi energy along the fiber before and after annealing. The Fermi energy is estimated based on the Seebeck coefficient via the model of Ref.[168]. (C) The Raman spectra of the fiber before and after annealing. Inset: The Raman spectra from 1500 – 1650 cm^{-1} including the G band. There is almost no shift in the 2D band and the G band red shifts about 3 cm^{-1}.

5.9. Summary

We demonstrate that mapping of the PTE is a non-destructive method to probe the variation of the Seebeck coefficient along doped CNTFs. The inferred Seebeck coefficient as a function of position along the fiber is consistent with expectations for a deliberately modified doping level distribution for the laser annealing sample. We

see a clear correlation between the Seebeck coefficient distribution and the Raman spectra as a function of position along the CNTF. This establishes that Seebeck response is dominated by the local doping level. The data in this work shows that the PTE based survey is more sensitive to small changes of doping level and the Fermi energy than typical Raman spectroscopy. Comparing the PTE measurements and the Seebeck coefficient results before and after a mild isothermal annealing, we see an increase of the average Seebeck coefficient of the fiber due to the decrease in the doping level. The spatial variation of the Seebeck coefficient is smaller after annealing, likely because of redistribution of dopants to a more uniform spatial distribution during the annealing process. From the Seebeck coefficient distribution, we can use a prior model connecting thermoelectric response and doping to calculate the Fermi energy along the fiber. This approach can be applied to other thermally one-dimensional systems, given reliable thermal models for the temperature distribution $T(x, x_0)$. Such measurements provide information about the uniformity of the system's thermodynamic and electronic properties, which is helpful for synthesizing higher quality and more uniform materials.

Chapter 6

Future projects

There are some possible follow-up works based on my projects:

1. Based on the previous reports, the frequency of the N ≡ C stretching vibration of phenyl isocyanide (PIC) molecule shows a strong dependence on temperature. [196,197] When the temperature is increasing, the angle between the N≡C bond and the Au surface decreases (Figure 6-1A), which makes the Raman mode shift to the lower wavenumber. The temperature and laser power dependent SERS can be measured, as shown in Figure 6-1B, C. The PIC based temperature sensor in SERS shows the sensitivity of 0.232 $cm^{-1}K^{-1}$ (Figure 6-1D). The PIC molecule-based temperature sensing can be also applied to the nanowire junction system. SERS by direct excitation can be measured as a function of temperature and laser power respectively for calibration and reference. SERS by remote excitation can be also measured to compare the temperature rise with the direct excitation. This method can help quantify the laser heating in the system.

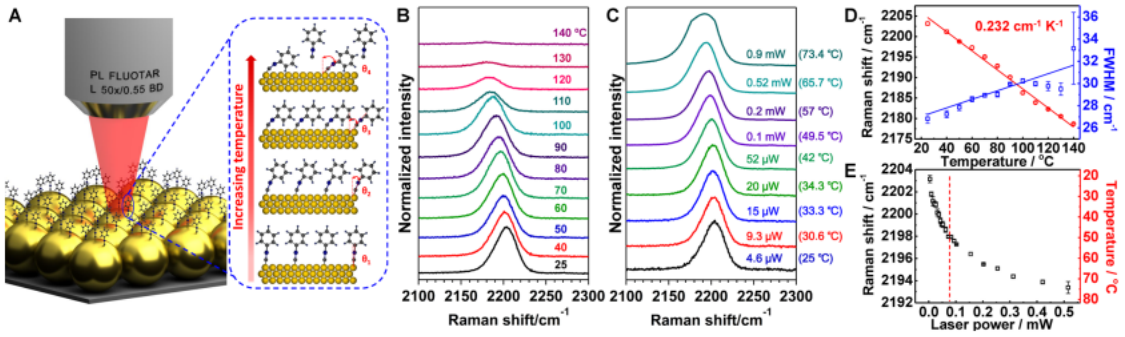

Figure 6-1:[196] **(A) Schematic of temperature-dependent SERS measurement and temperature-induced orientation change of PIC molecules. (B) Temperature- and (C) laser power-dependent SERS spectra of PIC in the spectral range of the N≡C stretching vibration. (D) Raman shift and FWHM of the N≡C peak as a function of temperature. (E) Raman shift of the N≡C peak as a function of laser power.**

2. In our current magnetic field EL setup, the sample is in x-y plane and the external magnetic field is fixed along z direction as shown in Figure 4-1. However, by design a new sample pod for the Opticool system, we can have the chip to be in x-z and y-z plane to control the relative directions of the sample plane, tunneling cuurent and the magnetic field. To do this, we need to put a small mirror in the Opticool chamber, as illustrated in Figure 6-2. The EL spectra can be measrued under different magnetic field and with different device orientations. Theses measurements may be helpful for us to better understand the role of magnetic field in EL and LSPRs.

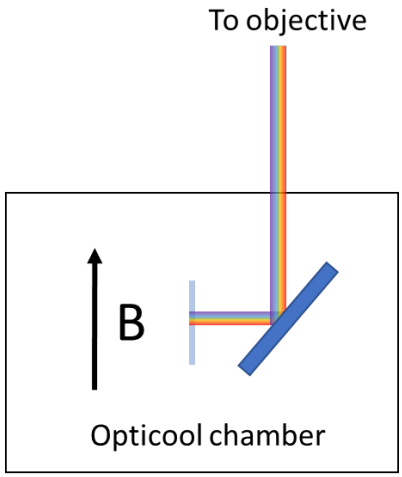

Figure 6-2: Sketch of the Opticool setup with a different chip orientation.

3. As discussed in Chapter 2-4, due to the randomness of the electromigration process, the nanojunctions can be highly asymmetric, which may result in asymmetric in I-V curve in these nanojunctions. The LSPRs can be different under positive and negative voltage bias as well. As a result, difference in EL spectra may be observed under voltage bias with different polarity. As discussed in Chapter 5, CD is observed in EL spectra. We may expect that other plasmonic behaviors like OCPV to be circular polarization dependent. OCPV can be measured under left-handed and right-handed laser excitation. The correlation between the CD in OCPV and EL can be statistically analyzed by measuring an ensemble of devices. The OCPV can be measured under different magnetic field too.

4. The PTE-based Seebeck coefficient extraction discussed in Chapter 5 is performed in steady state with laser illumination frequency small enough. At high chopper frequency, the phase shift of the average temperature as a function of laser

position is large and position-dependent (Figure 6-3), and this phase shift could possibly be useful in analysis of the PTE measurement because the phase shift is independent of the absorbed power. The similar PTE map measurements can be performed with different chopper frequency and the time-dependent temperature profile of the PTE measurements is needed.

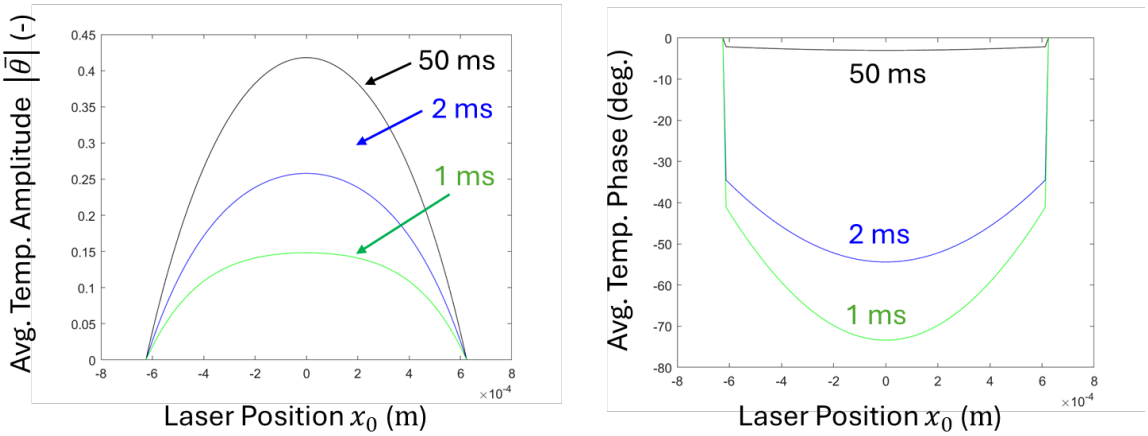

Figure 6-3: Amplitude (left) and phase angle shift (right) of the spatially averaged temperature $\bar{\theta}$ as a function of laser position x_0 for three chopper periods. This figure is provided by Dr. Geoff Wehmeyer.

References

(1) Maier, S. A. *Plasmonics: Fundamentals and Applications*; Springer US: New York, NY, 2007. https://doi.org/10.1007/0-387-37825-1.

(2) Kelly, K. L.; Coronado, E.; Zhao, L. L.; Schatz, G. C. The Optical Properties of Metal Nanoparticles: The Influence of Size, Shape, and Dielectric Environment. *J Phys Chem B* **2003**, *107* (3), 668–677. https://doi.org/10.1021/jp026731y.

(3) Novotny, L.; Hecht, B. *Principles of Nano-Optics*, 2nd ed.; Cambridge University Press: Cambridge, 2012. https://doi.org/DOI: 10.1017/CBO9780511794193.

(4) Wikipedia. *Localized surface plasmon* .

(5) Lu, X.; Rycenga, M.; Skrabalak, S. E.; Wiley, B.; Xia, Y. Chemical Synthesis of Novel Plasmonic Nanoparticles. *Annu Rev Phys Chem* **2009**, *60* (1), 167–192. https://doi.org/10.1146/annurev.physchem.040808.090434.

(6) Chu, M.-W.; Myroshnychenko, V.; Chen, C. H.; Deng, J.-P.; Mou, C.-Y.; García de Abajo, F. J. Probing Bright and Dark Surface-Plasmon Modes in Individual and Coupled Noble Metal Nanoparticles Using an Electron Beam. *Nano Lett* **2009**, *9* (1), 399–404. https://doi.org/10.1021/nl803270x.

(7) Hao, F.; Larsson, E. M.; Ali, T. A.; Sutherland, D. S.; Nordlander, P. Shedding Light on Dark Plasmons in Gold Nanorings. *Chem Phys Lett* **2008**, *458* (4–6), 262–266. https://doi.org/10.1016/j.cplett.2008.04.126.

(8) Li, C.; Chen, L.; McLeod, E.; Su, J. Dark Mode Plasmonic Optical Microcavity Biochemical Sensor. *Photonics Res* **2019**, *7* (8), 939. https://doi.org/10.1364/prj.7.000939.

(9) Gómez, D. E.; Teo, Z. Q.; Altissimo, M.; Davis, T. J.; Earl, S.; Roberts, A. The Dark Side of Plasmonics. *Nano Lett* **2013**, *13* (8), 3722–3728. https://doi.org/10.1021/nl401656e.

(10) Herzog, J. B.; Knight, M. W.; Li, Y.; Evans, K. M.; Halas, N. J.; Natelson, D. Dark Plasmons in Hot Spot Generation and Polarization in Interelectrode Nanoscale Junctions. *Nano Lett* **2013**, *13* (3), 1359–1364. https://doi.org/10.1021/nl400363d.

(11) Lassiter, J. B.; Sobhani, H.; Fan, J. A.; Kundu, J.; Capasso, F.; Nordlander, P.; Halas, N. J. Fano Resonances in Plasmonic Nanoclusters: Geometrical and Chemical Tunability. *Nano Lett* **2010**, *10* (8), 3184–3189. https://doi.org/10.1021/nl102108u.

(12) Nelayah, J.; Kociak, M.; Stéphan, O.; García de Abajo, F. J.; Tencé, M.; Henrard, L.; Taverna, D.; Pastoriza-Santos, I.; Liz-Marzán, L. M.; Colliex, C. Mapping

Surface Plasmons on a Single Metallic Nanoparticle. *Nat Phys* **2007**, *3* (5), 348–353. https://doi.org/10.1038/nphys575.

(13) Schertz, F.; Schmelzeisen, M.; Mohammadi, R.; Kreiter, M.; Elmers, H.-J.; Schönhense, G. Near Field of Strongly Coupled Plasmons: Uncovering Dark Modes. *Nano Lett* **2012**, *12* (4), 1885–1890. https://doi.org/10.1021/nl204277y.

(14) Bitton, O.; Gupta, S. N.; Houben, L.; Kvapil, M.; Křápek, V.; Šikola, T.; Haran, G. Vacuum Rabi Splitting of a Dark Plasmonic Cavity Mode Revealed by Fast Electrons. *Nat Commun* **2020**, *11* (1), 487. https://doi.org/10.1038/s41467-020-14364-3.

(15) Prodan, E.; Radloff, C.; Halas, N. J.; Nordlander, P. A Hybridization Model for the Plasmon Response of Complex Nanostructures. *Science (1979)* **2003**, *302* (5644), 419–422. https://doi.org/10.1126/science.1089171.

(16) Brongersma, M. L.; Halas, N. J.; Nordlander, P. Plasmon-Induced Hot Carrier Science and Technology. *Nat Nanotechnol* **2015**, *10* (1), 25–34. https://doi.org/10.1038/nnano.2014.311.

(17) Bohren, C. F. How Can a Particle Absorb More than the Light Incident on It? *Am J Phys* **1983**, *51* (4), 323–327. https://doi.org/10.1119/1.13262.

(18) Oldenburg, S. J.; Averitt, R. D.; Westcott, S. L.; Halas, N. J. Nanoengineering of Optical Resonances. *Chem Phys Lett* **1998**, *288* (2), 243–247. https://doi.org/https://doi.org/10.1016/S0009-2614(98)00277-2.

(19) Li, X.; Xiao, D.; Zhang, Z. Landau Damping of Quantum Plasmons in Metal Nanostructures. *New J Phys* **2013**, *15* (2), 023011. https://doi.org/10.1088/1367-2630/15/2/023011.

(20) Hao, F.; Sonnefraud, Y.; Dorpe, P. Van; Maier, S. A.; Halas, N. J.; Nordlander, P. Symmetry Breaking in Plasmonic Nanocavities: Subradiant LSPR Sensing and a Tunable Fano Resonance. *Nano Lett* **2008**, *8* (11), 3983–3988. https://doi.org/10.1021/nl802509r.

(21) Manjavacas, A.; Liu, J. G.; Kulkarni, V.; Nordlander, P. Plasmon-Induced Hot Carriers in Metallic Nanoparticles. *ACS Nano* **2014**, *8* (8), 7630–7638. https://doi.org/10.1021/nn502445f.

(22) Lisowski, M.; Loukakos, P. A.; Bovensiepen, U.; Stähler, J.; Gahl, C.; Wolf, M. Ultra-Fast Dynamics of Electron Thermalization, Cooling and Transport Effects in Ru(001). *Applied Physics A* **2004**, *78* (2), 165–176. https://doi.org/10.1007/s00339-003-2301-7.

(23) Inouye, H.; Tanaka, K.; Tanahashi, I.; Hirao, K. Ultrafast Dynamics of Nonequilibrium Electrons in a Gold Nanoparticle System. *Phys Rev B* **1998**, *57* (18), 11334–11340. https://doi.org/10.1103/PhysRevB.57.11334.

(24) Zhang, Y.; He, S.; Guo, W.; Hu, Y.; Huang, J.; Mulcahy, J. R.; Wei, W. D. Surface-Plasmon-Driven Hot Electron Photochemistry. *Chem Rev* **2018**, *118* (6), 2927–2954. https://doi.org/10.1021/acs.chemrev.7b00430.

(25) Christopher, P.; Xin, H.; Marimuthu, A.; Linic, S. Singular Characteristics and Unique Chemical Bond Activation Mechanisms of Photocatalytic Reactions on Plasmonic Nanostructures. *Nat Mater* **2012**, *11* (12), 1044–1050. https://doi.org/10.1038/nmat3454.

(26) Mukherjee, S.; Zhou, L.; Goodman, A. M.; Large, N.; Ayala-Orozco, C.; Zhang, Y.; Nordlander, P.; Halas, N. J. Hot-Electron-Induced Dissociation of H2 on Gold Nanoparticles Supported on SiO2. *J Am Chem Soc* **2014**, *136* (1), 64–67. https://doi.org/10.1021/ja411017b.

(27) Mukherjee, S.; Libisch, F.; Large, N.; Neumann, O.; Brown, L. V; Cheng, J.; Lassiter, J. B.; Carter, E. A.; Nordlander, P.; Halas, N. J. Hot Electrons Do the Impossible: Plasmon-Induced Dissociation of H2 on Au. *Nano Lett* **2013**, *13* (1), 240–247. https://doi.org/10.1021/nl303940z.

(28) Hou, J.-L.; Fischer, A.; Yang, S.-C.; Benduhn, J.; Widmer, J.; Kasemann, D.; Vandewal, K.; Leo, K. Plasmon-Induced Sub-Bandgap Photodetection with Organic Schottky Diodes. *Adv Funct Mater* **2016**, *26* (31), 5741–5747. https://doi.org/https://doi.org/10.1002/adfm.201601718.

(29) Li, M.; Bhaumik, S.; Goh, T. W.; Kumar, M. S.; Yantara, N.; Grätzel, M.; Mhaisalkar, S.; Mathews, N.; Sum, T. C. Slow Cooling and Highly Efficient Extraction of Hot Carriers in Colloidal Perovskite Nanocrystals. *Nat Commun* **2017**, *8* (1), 14350. https://doi.org/10.1038/ncomms14350.

(30) Wang, C.-W.; Liu, X.; Qiao, T.; Khurana, M.; Akimov, A. V; Son, D. H. Photoemission of the Upconverted Hot Electrons in Mn-Doped CsPbBr3 Nanocrystals. *Nano Lett* **2022**, *22* (16), 6753–6759. https://doi.org/10.1021/acs.nanolett.2c02342.

(31) Lee, H.; Park, Y.; Song, K.; Park, J. Y. Surface Plasmon-Induced Hot Carriers: Generation, Detection, and Applications. *Acc Chem Res* **2022**, *55* (24), 3727–3737. https://doi.org/10.1021/acs.accounts.2c00623.

(32) Lee, C.; Lee, Y. K.; Park, Y.; Park, J. Y. Polarization Effect of Hot Electrons in Tandem-Structured Plasmonic Nanodiode. *ACS Photonics* **2018**, *5* (9), 3499–3506. https://doi.org/10.1021/acsphotonics.8b00717.

(33) Cui, L.; Zhu, Y.; Abbasi, M.; Ahmadivand, A.; Gerislioglu, B.; Nordlander, P.; Natelson, D. Electrically Driven Hot-Carrier Generation and Above-Threshold Light Emission in Plasmonic Tunnel Junctions. *Nano Lett* **2020**, *20* (8), 6067–6075. https://doi.org/10.1021/acs.nanolett.0c02121.

(34) Nagpal, P.; Lindquist, N. C.; Oh, S.-H.; Norris, D. J. Ultrasmooth Patterned Metals for Plasmonics and Metamaterials. *Science (1979)* **2009**, *325* (5940), 594–597. https://doi.org/10.1126/science.1174655.

(35) Bozhevolnyi, S. I.; Volkov, V. S.; Devaux, E.; Laluet, J.-Y.; Ebbesen, T. W. Channel Plasmon Subwavelength Waveguide Components Including Interferometers and Ring Resonators. *Nature* **2006**, *440* (7083), 508–511. https://doi.org/10.1038/nature04594.

(36) Bozhevolnyi, S. I.; Volkov, V. S.; Devaux, E.; Ebbesen, T. W. Channel Plasmon-Polariton Guiding by Subwavelength Metal Grooves. *Phys Rev Lett* **2005**, *95* (4), 46802. https://doi.org/10.1103/PhysRevLett.95.046802.

(37) Zhang, J.; Zhang, L.; Xu, W. Surface Plasmon Polaritons: Physics and Applications. *J Phys D Appl Phys* **2012**, *45* (11), 113001. https://doi.org/10.1088/0022-3727/45/11/113001.

(38) Kawata, S.; Inouye, Y.; Verma, P. Plasmonics for Near-Field Nano-Imaging and Superlensing. *Nat Photonics* **2009**, *3* (7), 388–394. https://doi.org/10.1038/nphoton.2009.111.

(39) Fang, N.; Lee, H.; Sun, C.; Zhang, X. Sub-Diffraction-Limited Optical Imaging with a Silver Superlens. *Science (1979)* **2005**, *308* (5721), 534–537. https://doi.org/10.1126/science.1108759.

(40) Wikipedia contributors. *Surface plasmon*.

(41) Bashevoy, M. V; Jonsson, F.; Krasavin, A. V; Zheludev, N. I.; Chen, Y.; Stockman, M. I. Generation of Traveling Surface Plasmon Waves by Free-Electron Impact. *Nano Lett* **2006**, *6* (6), 1113–1115. https://doi.org/10.1021/nl060941v.

(42) Zeng, S.; Yu, X.; Law, W.-C.; Zhang, Y.; Hu, R.; Dinh, X.-Q.; Ho, H.-P.; Yong, K.-T. Size Dependence of Au NP-Enhanced Surface Plasmon Resonance Based on Differential Phase Measurement. *Sens Actuators B Chem* **2013**, *176*, 1128–1133. https://doi.org/https://doi.org/10.1016/j.snb.2012.09.073.

(43) Zayats, A. V; Smolyaninov, I. I.; Maradudin, A. A. Nano-Optics of Surface Plasmon Polaritons. *Phys Rep* **2005**, *408* (3), 131–314. https://doi.org/https://doi.org/10.1016/j.physrep.2004.11.001.

(44) Zayats, A. V; Smolyaninov, I. I. Near-Field Photonics: Surface Plasmon Polaritons and Localized Surface. *Journal of Optics A: Pure and Applied Optics* **2003**, *5* (4), S16. https://doi.org/10.1088/1464-4258/5/4/353.

(45) Homola, J.; Yee, S. S.; Gauglitz, G. Surface Plasmon Resonance Sensors: Review. *Sens Actuators B Chem* **1999**, *54* (1), 3–15. https://doi.org/https://doi.org/10.1016/S0925-4005(98)00321-9.

(46) Sharma, A. K.; Jha, R.; Gupta, B. D. Fiber-Optic Sensors Based on Surface Plasmon Resonance: A Comprehensive Review. *IEEE Sens J* **2007**, *7* (8), 1118–1129. https://doi.org/10.1109/JSEN.2007.897946.

(47) Kashyap, R.; Nemova, G. Surface Plasmon Resonance-Based Fiber and Planar Waveguide Sensors. *J Sens* **2009**, *2009* (1), 645162. https://doi.org/https://doi.org/10.1155/2009/645162.

(48) Kryukov, A. E.; Kim, Y.-K.; Ketterson, J. B. Surface Plasmon Scanning Near-Field Optical Microscopy. *J Appl Phys* **1997**, *82* (11), 5411–5415. https://doi.org/10.1063/1.365568.

(49) Kim, Y.; Lundquist, P. M.; Helfrich, J. A.; Mikrut, J. M.; Wong, G. K.; Auvil, P. R.; Ketterson, J. B. Scanning Plasmon Optical Microscope. *Appl Phys Lett* **1995**, *66* (25), 3407–3409. https://doi.org/10.1063/1.113369.

(50) Ebbesen, T. W.; Lezec, H. J.; Ghaemi, H. F.; Thio, T.; Wolff, P. A. Extraordinary Optical Transmission through Sub-Wavelength Hole Arrays. *Nature* **1998**, *391* (6668), 667–669. https://doi.org/10.1038/35570.

(51) Raether, H. *Surface Plasmons on Smooth and Rough Surfaces and on Gratings / Heinz Raether.*, 1st ed. 1988.; Springer Tracts in Modern Physics ; Volume 111; Springer-Verlag: Berlin, Heidelberg, 1988. https://doi.org/10.1007/BFb0048317.

(52) RAMAN, C. V; KRISHNAN, K. S. A New Type of Secondary Radiation. *Nature* **1928**, *121* (3048), 501–502. https://doi.org/10.1038/121501c0.

(53) Efremov, E. V; Ariese, F.; Gooijer, C. Achievements in Resonance Raman Spectroscopy: Review of a Technique with a Distinct Analytical Chemistry

Potential. *Anal Chim Acta* **2008**, *606* (2), 119–134. https://doi.org/https://doi.org/10.1016/j.aca.2007.11.006.

(54) Clark, R. J. H.; Dines, T. J. Resonance Raman Spectroscopy, and Its Application to Inorganic Chemistry. New Analytical Methods (27). *Angewandte Chemie International Edition in English* **1986**, *25* (2), 131–158. https://doi.org/https://doi.org/10.1002/anie.198601311.

(55) Pence, I.; Mahadevan-Jansen, A. Clinical Instrumentation and Applications of Raman Spectroscopy. *Chem Soc Rev* **2016**, *45* (7), 1958–1979. https://doi.org/10.1039/C5CS00581G.

(56) Tu, Q.; Chang, C. Diagnostic Applications of Raman Spectroscopy. *Nanomedicine* **2012**, *8* (5), 545–558. https://doi.org/https://doi.org/10.1016/j.nano.2011.09.013.

(57) Das, R. S.; Agrawal, Y. K. Raman Spectroscopy: Recent Advancements, Techniques and Applications. *Vib Spectrosc* **2011**, *57* (2), 163–176. https://doi.org/https://doi.org/10.1016/j.vibspec.2011.08.003.

(58) Kudelski, A. Analytical Applications of Raman Spectroscopy. *Talanta* **2008**, *76* (1), 1–8. https://doi.org/https://doi.org/10.1016/j.talanta.2008.02.042.

(59) Fleischmann, M.; Hendra, P. J.; McQuillan, A. J. Raman Spectra of Pyridine Adsorbed at a Silver Electrode. *Chem Phys Lett* **1974**, *26* (2), 163–166. https://doi.org/https://doi.org/10.1016/0009-2614(74)85388-1.

(60) Schlücker, S. Surface-Enhanced Raman Spectroscopy: Concepts and Chemical Applications. *Angewandte Chemie International Edition* **2014**, *53* (19), 4756–4795. https://doi.org/https://doi.org/10.1002/anie.201205748.

(61) Moskovits, M. Surface-Enhanced Raman Spectroscopy: A Brief Retrospective. *Journal of Raman Spectroscopy* **2005**, *36* (6–7), 485–496. https://doi.org/https://doi.org/10.1002/jrs.1362.

(62) Stiles, P. L.; Dieringer, J. A.; Shah, N. C.; Van Duyne, R. P. Surface-Enhanced Raman Spectroscopy. *Annual Review of Analytical Chemistry* **2008**, *1* (1), 601–626. https://doi.org/10.1146/annurev.anchem.1.031207.112814.

(63) Wikipedia. *Raman spectroscopy*. The Free Encyclopedia. Wikipedia.

(64) Pilot, R.; Signorini, R.; Durante, C.; Orian, L.; Bhamidipati, M.; Fabris, L. A Review on Surface-Enhanced Raman Scattering. *Biosensors (Basel)* **2019**, *9* (2). https://doi.org/10.3390/bios9020057.

(65) Le Ru, Eric. *Principles of Surface-Enhanced Raman Spectroscopy : And Related Plasmonic Effects.*; Elsevier Science & Technology,: Oxford :, 2008.

(66) Pilot, R.; Signorini, R.; Fabris, L. Surface-Enhanced Raman Spectroscopy: Principles, Substrates, and Applications. In *Metal Nanoparticles and Clusters: Advances in Synthesis, Properties and Applications*; Deepak, F. L., Ed.; Springer International Publishing: Cham, 2018; pp 89–164. https://doi.org/10.1007/978-3-319-68053-8_4.

(67) Long, D. A. *The Raman Effect:A Unified Treatment of the Theory of Raman Scattering by Molecules*; Wiley, 2002. https://doi.org/10.1002/0470845767.

(68) Lombardi, J. R.; Birke, R. L.; Lu, T.; Xu, J. Charge-transfer Theory of Surface Enhanced Raman Spectroscopy: Herzberg–Teller Contributions. *J Chem Phys* **1986**, *84* (8), 4174–4180. https://doi.org/10.1063/1.450037.

(69) Lombardi, J. R.; Birke, R. L. A Unified Approach to Surface-Enhanced Raman Spectroscopy. *The Journal of Physical Chemistry C* **2008**, *112* (14), 5605–5617. https://doi.org/10.1021/jp800167v.

(70) Xia, L.; Chen, M.; Zhao, X.; Zhang, Z.; Xia, J.; Xu, H.; Sun, M. Visualized Method of Chemical Enhancement Mechanism on SERS and TERS. *Journal of Raman Spectroscopy* **2014**, *45* (7), 533–540. https://doi.org/https://doi.org/10.1002/jrs.4504.

(71) Aroca, Ri. Chemical Effects and the SERS Spectrum. In *Surface-Enhanced Vibrational Spectroscopy*; John Wiley & Sons, Ltd, 2006; pp 107–132. https://doi.org/https://doi.org/10.1002/9780470035641.ch4.

(72) Zhu, Y.; Natelson, D.; Cui, L. Probing Energy Dissipation in Molecular-Scale Junctions via Surface Enhanced Raman Spectroscopy: Vibrational Pumping and Hot Carrier Enhanced Light Emission. *Journal of Physics: Condensed Matter* **2021**, *33* (13), 134001. https://doi.org/10.1088/1361-648X/abda7b.

(73) Talley, C. E.; Jackson, J. B.; Oubre, C.; Grady, N. K.; Hollars, C. W.; Lane, S. M.; Huser, T. R.; Nordlander, P.; Halas, N. J. Surface-Enhanced Raman Scattering from Individual Au Nanoparticles and Nanoparticle Dimer Substrates. *Nano Lett* **2005**, *5* (8), 1569–1574. https://doi.org/10.1021/nl050928v.

(74) Jensen, T. R.; Malinsky, M. D.; Haynes, C. L.; Van Duyne, R. P. Nanosphere Lithography: Tunable Localized Surface Plasmon Resonance Spectra of Silver Nanoparticles. *J Phys Chem B* **2000**, *104* (45), 10549–10556. https://doi.org/10.1021/jp002435e.

(75) Pettinger, B.; Picardi, G.; Schuster, R.; Ertl, G. Surface-Enhanced and STM-Tip-Enhanced Raman Spectroscopy at Metal Surfaces. *Single Molecules* **2002**, *3* (5–6), 285–294. https://doi.org/https://doi.org/10.1002/1438-5171(200211)3:5/6<285::AID-SIMO285>3.0.CO;2-X.

(76) Blackie, E. J.; Le Ru, E. C.; Etchegoin, P. G. Single-Molecule Surface-Enhanced Raman Spectroscopy of Nonresonant Molecules. *J Am Chem Soc* **2009**, *131* (40), 14466–14472. https://doi.org/10.1021/ja905319w.

(77) Dieringer, J. A.; Lettan, R. B.; Scheidt, K. A.; Van Duyne, R. P. A Frequency Domain Existence Proof of Single-Molecule Surface-Enhanced Raman Spectroscopy. *J Am Chem Soc* **2007**, *129* (51), 16249–16256. https://doi.org/10.1021/ja077243c.

(78) Le Ru, E. C.; Etchegoin, P. G. Single-Molecule Surface-Enhanced Raman Spectroscopy. *Annu Rev Phys Chem* **2012**, *63* (1), 65–87. https://doi.org/10.1146/annurev-physchem-032511-143757.

(79) Huh, Y. S.; Chung, A. J.; Erickson, D. Surface Enhanced Raman Spectroscopy and Its Application to Molecular and Cellular Analysis. *Microfluid Nanofluidics* **2009**, *6* (3), 285–297. https://doi.org/10.1007/s10404-008-0392-3.

(80) Cotton, T. M.; Kim, J.-H.; Chumanov, G. D. Application of Surface-Enhanced Raman Spectroscopy to Biological Systems. *Journal of Raman Spectroscopy* **1991**, *22* (12), 729–742. https://doi.org/https://doi.org/10.1002/jrs.1250221203.

(81) Xie, W.; Herrmann, C.; Kömpe, K.; Haase, M.; Schlücker, S. Synthesis of Bifunctional Au/Pt/Au Core/Shell Nanoraspberries for in Situ SERS Monitoring of Platinum-Catalyzed Reactions. *J Am Chem Soc* **2011**, *133* (48), 19302–19305. https://doi.org/10.1021/ja208298q.

(82) Zebarjadi, M. Electronic Cooling Using Thermoelectric Devices. *Appl Phys Lett* **2015**, *106* (20), 203506. https://doi.org/10.1063/1.4921457.

(83) Minnich, A. J.; Dresselhaus, M. S.; Ren, Z. F.; Chen, G. Bulk Nanostructured Thermoelectric Materials: Current Research and Future Prospects. *Energy Environ Sci* **2009**, *2* (5), 466–479. https://doi.org/10.1039/B822664B.

(84) Wood, C. Materials for Thermoelectric Energy Conversion. *Reports on Progress in Physics* **1988**, *51* (4), 459. https://doi.org/10.1088/0034-4885/51/4/001.

(85) Baeyens, J. Waste Energy Harvesting: Mechanical and Thermal Energies. *Energy technology (Weinheim, Germany)*. WILEY-VCH Verlag: Weinheim 2015, p 790. https://doi.org/10.1002/ente.201500113.

(86) Cutler, M.; Mott, N. F. Observation of Anderson Localization in an Electron Gas. *Physical Review* **1969**, *181* (3), 1336–1340. https://doi.org/10.1103/PhysRev.181.1336.

(87) Van Hove, L. The Occurrence of Singularities in the Elastic Frequency Distribution of a Crystal. *Physical Review* **1953**, *89* (6), 1189–1193. https://doi.org/10.1103/PhysRev.89.1189.

(88) Goldsmid, H. J. *Introduction to Thermoelectricity*, 2nd ed. 2016.; Springer Series in Materials Science, 121; Springer Berlin Heidelberg: Berlin, Heidelberg, 2016. https://doi.org/10.1007/978-3-662-49256-7.

(89) Komatsu, N. Thermoelectric and Electronic Transport Studies of Ultrahigh-Conductivity Carbon Nanotube Fibers, Rice University, Houston, 2022.

(90) Pant, M.; Singh, R.; Negi, P.; Tiwari, K.; Singh, Y. A Comprehensive Review on Carbon Nano-Tube Synthesis Using Chemical Vapor Deposition. *Mater Today Proc* **2021**, *46*, 11250–11253. https://doi.org/https://doi.org/10.1016/j.matpr.2021.02.646.

(91) Liu, Y.; and Kumar, S. Recent Progress in Fabrication, Structure, and Properties of Carbon Fibers. *Polymer Reviews* **2012**, *52* (3), 234–258. https://doi.org/10.1080/15583724.2012.705410.

(92) Rathinavel, S.; Priyadharshini, K.; Panda, D. A Review on Carbon Nanotube: An Overview of Synthesis, Properties, Functionalization, Characterization, and the Application. *Materials Science and Engineering: B* **2021**, *268*, 115095. https://doi.org/https://doi.org/10.1016/j.mseb.2021.115095.

(93) Hughes, K. J.; Iyer, K. A.; Bird, R. E.; Ivanov, J.; Banerjee, S.; Georges, G.; Zhou, Q. A. Review of Carbon Nanotube Research and Development: Materials and Emerging Applications. *ACS Appl Nano Mater* **2024**, *7* (16), 18695–18713. https://doi.org/10.1021/acsanm.4c02721.

(94) Dresselhaus, M. S.; Dresselhaus, Gene.; Avouris, Phaedon. *Carbon Nanotubes : Synthesis, Structure, Properties, and Applications / Edited by Mildred S. Dresselhaus, Gene Dresselhaus, Phaedon Avouris.*, 1st ed. 2001.; Topics in Applied Physics, 80; Springer Berlin Heidelberg: Berlin, Heidelberg, 2001. https://doi.org/10.1007/3-540-39947-X.

(95) Zhang, R.; Zhang, Y.; Zhang, Q.; Xie, H.; Qian, W.; Wei, F. Growth of Half-Meter Long Carbon Nanotubes Based on Schulz–Flory Distribution. *ACS Nano* **2013**, *7* (7), 6156–6161. https://doi.org/10.1021/nn401995z.

(96) Sugime, H.; Sato, T.; Nakagawa, R.; Hayashi, T.; Inoue, Y.; Noda, S. Ultra-Long Carbon Nanotube Forest via in Situ Supplements of Iron and Aluminum Vapor Sources. *Carbon N Y* **2021**, *172*, 772–780. https://doi.org/https://doi.org/10.1016/j.carbon.2020.10.066.

(97) Vajtai, R. *Springer Handbook of Nanomaterials / Robert Vajtai (Ed.).*; Springer: Berlin, 2013.

(98) Kane, C. L.; Mele, E. J. Size, Shape, and Low Energy Electronic Structure of Carbon Nanotubes. *Phys Rev Lett* **1997**, *78* (10), 1932–1935. https://doi.org/10.1103/PhysRevLett.78.1932.

(99) Hamada, N.; Sawada, S.; Oshiyama, A. New One-Dimensional Conductors: Graphitic Microtubules. *Phys Rev Lett* **1992**, *68* (10), 1579–1581. https://doi.org/10.1103/PhysRevLett.68.1579.

(100) Nanot, S.; Hároz, E. H.; Kim, J.-H.; Hauge, R. H.; Kono, J. Optoelectronic Properties of Single-Wall Carbon Nanotubes. *Advanced Materials* **2012**, *24* (36), 4977–4994. https://doi.org/https://doi.org/10.1002/adma.201201751.

(101) Li, K.; Ni, X.; Wu, Q.; Yuan, C.; Li, C.; Li, D.; Chen, H.; Lv, Y.; Ju, A. Carbon-Based Fibers: Fabrication, Characterization and Application. *Advanced Fiber Materials* **2022**, *4* (4), 631–682. https://doi.org/10.1007/s42765-022-00134-x.

(102) Lee, S.-H.; Park, J. H.; Kim, S. M. Synthesis, Property, and Application of Carbon Nanotube Fiber. *Journal of the Korean Ceramic Society* **2021**, *58* (2), 148–159. https://doi.org/10.1007/s43207-020-00106-0.

(103) Janas, D.; Koziol, K. K. Carbon Nanotube Fibers and Films: Synthesis, Applications and Perspectives of the Direct-Spinning Method. *Nanoscale* **2016**, *8* (47), 19475–19490. https://doi.org/10.1039/C6NR07549E.

(104) Lu, W.; Zu, M.; Byun, J.-H.; Kim, B.-S.; Chou, T.-W. State of the Art of Carbon Nanotube Fibers: Opportunities and Challenges. *Advanced Materials* **2012**, *24* (14), 1805–1833. https://doi.org/https://doi.org/10.1002/adma.201104672.

(105) Zhang, Y.; Zhang, Q.; Chen, G. Carbon and Carbon Composites for Thermoelectric Applications. *Carbon Energy* **2020**, *2* (3), 408–436. https://doi.org/https://doi.org/10.1002/cey2.68.

(106) Blackburn, J. L.; Ferguson, A. J.; Cho, C.; Grunlan, J. C. Carbon-Nanotube-Based Thermoelectric Materials and Devices. *Advanced Materials* **2018**, *30* (11), 1704386. https://doi.org/https://doi.org/10.1002/adma.201704386.

(107) Taylor, L. W.; Dewey, O. S.; Headrick, R. J.; Komatsu, N.; Peraca, N. M.; Wehmeyer, G.; Kono, J.; Pasquali, M. Improved Properties, Increased Production, and the Path to Broad Adoption of Carbon Nanotube Fibers.

Carbon N Y **2021**, *171*, 689–694. https://doi.org/https://doi.org/10.1016/j.carbon.2020.07.058.

(108) Evans, C. I.; Yang, R.; Gan, L. T.; Abbasi, M.; Wang, X.; Traylor, R.; Fan, J. A.; Natelson, D. Thermoelectric Response from Grain Boundaries and Lattice Distortions in Crystalline Gold Devices. *Proceedings of the National Academy of Sciences* **2020**, *117* (38), 23350–23355. https://doi.org/10.1073/pnas.2002284117.

(109) Evans, C. I.; Gan, L. T.; Yang, R.; Abbasi, M.; Wang, X.; Traylor, R.; Fan, J. A.; Natelson, D. Detection of Trace Impurity Gradients in Noble Metals by the Photothermoelectric Effect. *The Journal of Physical Chemistry C* **2021**, *125* (31), 17509–17517. https://doi.org/10.1021/acs.jpcc.1c04927.

(110) Abbasi, M.; Evans, C. I.; Chen, L.; Natelson, D. Single Metal Photodetectors Using Plasmonically-Active Asymmetric Gold Nanostructures. *ACS Nano* **2020**, *14* (12), 17535–17542. https://doi.org/10.1021/acsnano.0c08035.

(111) Zolotavin, P.; Alabastri, A.; Nordlander, P.; Natelson, D. Plasmonic Heating in Au Nanowires at Low Temperatures: The Role of Thermal Boundary Resistance. *ACS Nano* **2016**, *10* (7), 6972–6979. https://doi.org/10.1021/acsnano.6b02911.

(112) Ssennyimba, K.; Liao, S.; Zhu, Y.; Legvold, T.; Lowder, D.; Pagadala, K.; Boltasseva, A.; Shalaev, V.; Natelosn, D. Plasmonic Heating, Thermoelectric

Response, and Thermal Emission in Titanium Nitride Nanowires. *under review*.

(113) Park, H.; Lim, A. K. L.; Alivisatos, A. P.; Park, J.; McEuen, P. L. Fabrication of Metallic Electrodes with Nanometer Separation by Electromigration. *Appl Phys Lett* **1999**, *75* (2), 301–303. https://doi.org/10.1063/1.124354.

(114) Ward, D. R.; Corley, D. A.; Tour, J. M.; Natelson, D. Vibrational and Electronic Heating in Nanoscale Junctions. *Nat Nanotechnol* **2011**, *6* (1), 33–38. https://doi.org/10.1038/nnano.2010.240.

(115) Ward, D. R.; Grady, N. K.; Levin, C. S.; Halas, N. J.; Wu, Y.; Nordlander, P.; Natelson, D. Electromigrated Nanoscale Gaps for Surface-Enhanced Raman Spectroscopy. *Nano Lett* **2007**, *7* (5), 1396–1400. https://doi.org/10.1021/nl070625w.

(116) García-Martín, A.; Ward, D. R.; Natelson, D.; Cuevas, J. C. Field Enhancement in Subnanometer Metallic Gaps. *Phys Rev B* **2011**, *83* (19), 193404. https://doi.org/10.1103/PhysRevB.83.193404.

(117) Zolotavin, P.; Evans, C.; Natelson, D. Photothermoelectric Effects and Large Photovoltages in Plasmonic Au Nanowires with Nanogaps. *J Phys Chem Lett* **2017**, *8* (8), 1739–1744. https://doi.org/10.1021/acs.jpclett.7b00507.

(118) Kornbluth, M.; Nitzan, A.; Seideman, T. Light-Induced Electronic Non-Equilibrium in Plasmonic Particles. *J Chem Phys* **2013**, *138* (17), 174707. https://doi.org/10.1063/1.4802000.

(119) Abbasi, M.; Liao, S.; Zhu, Y.; Natelson, D. Engineering the Directionality of Hot Carrier Tunneling in Plasmonic Tunneling Structures. *Appl Phys Lett* **2023**, *122* (23), 231103. https://doi.org/10.1063/5.0150891.

(120) Zhu, Y.; Yelishala, S.; Liao, S.; Shropshire, J.; Natelson, D.; Cui, L. Single-Crystal Plasmonic Optoelectronics for Efficient Hot Carrier Collection and Photovoltage Detection. *under review*.

(121) Huang, W.; Qian, W.; El-Sayed, M. A.; Ding, Y.; Wang, Z. L. Effect of the Lattice Crystallinity on the Electron−Phonon Relaxation Rates in Gold Nanoparticles. *The Journal of Physical Chemistry C* **2007**, *111* (29), 10751–10757. https://doi.org/10.1021/jp0738917.

(122) Lambe, J.; McCarthy, S. L. Light Emission from Inelastic Electron Tunneling. *Phys Rev Lett* **1976**, *37* (14), 923–925. https://doi.org/10.1103/PhysRevLett.37.923.

(123) Downes, A.; Dumas, Ph.; Welland, M. E. Measurement of High Electron Temperatures in Single Atom Metal Point Contacts by Light Emission. *Appl Phys Lett* **2002**, *81* (7), 1252–1254. https://doi.org/10.1063/1.1497188.

(124) Hoffmann, G.; Berndt, R.; Johansson, P. Two-Electron Photon Emission from Metallic Quantum Wells. *Phys Rev Lett* **2003**, *90* (4), 46803. https://doi.org/10.1103/PhysRevLett.90.046803.

(125) Pechou, R.; Coratger, R.; Ajustron, F.; Beauvillain, J. Cutoff Anomalies in Light Emitted from the Tunneling Junction of a Scanning Tunneling Microscope in Air. *Appl Phys Lett* **1998**, *72* (6), 671–673. https://doi.org/10.1063/1.120841.

(126) Buret, M.; Uskov, A. V; Dellinger, J.; Cazier, N.; Mennemanteuil, M.-M.; Berthelot, J.; Smetanin, I. V; Protsenko, I. E.; Colas-des-Francs, G.; Bouhelier, A. Spontaneous Hot-Electron Light Emission from Electron-Fed Optical Antennas. *Nano Lett* **2015**, *15* (9), 5811–5818. https://doi.org/10.1021/acs.nanolett.5b01861.

(127) Peters, P.-J.; Xu, F.; Kaasbjerg, K.; Rastelli, G.; Belzig, W.; Berndt, R. Quantum Coherent Multielectron Processes in an Atomic Scale Contact. *Phys Rev Lett* **2017**, *119* (6), 66803. https://doi.org/10.1103/PhysRevLett.119.066803.

(128) Schull, G.; Néel, N.; Johansson, P.; Berndt, R. Electron-Plasmon and Electron-Electron Interactions at a Single Atom Contact. *Phys Rev Lett* **2009**, *102* (5), 57401. https://doi.org/10.1103/PhysRevLett.102.057401.

(129) Kalathingal, V.; Dawson, P.; Mitra, J. Scanning Tunnelling Microscope Light Emission: Finite Temperature Current Noise and over Cut-off Emission. *Sci Rep* **2017**, *7* (1), 3530. https://doi.org/10.1038/s41598-017-03766-x.

(130) Zhu, Y.; Cui, L.; Natelson, D. Hot-Carrier Enhanced Light Emission: The Origin of above-Threshold Photons from Electrically Driven Plasmonic Tunnel Junctions. *J Appl Phys* **2020**, *128* (23), 233105. https://doi.org/10.1063/5.0024392.

(131) Zhu, Y. Electrically Driven Plasmonic Processes: Hot Carriers and Strong Coupling. PhD Diss., Rice University, 2023.

(132) Cui, L.; Zhu, Y.; Nordlander, P.; Di Ventra, M.; Natelson, D. Thousand-Fold Increase in Plasmonic Light Emission via Combined Electronic and Optical Excitations. *Nano Lett* **2021**, *21* (6), 2658–2665. https://doi.org/10.1021/acs.nanolett.1c00503.

(133) Zhu, Y.; Cui, L.; Abbasi, M.; Natelson, D. Tuning Light Emission Crossovers in Atomic-Scale Aluminum Plasmonic Tunnel Junctions. *Nano Lett* **2022**, *22* (20), 8068–8075. https://doi.org/10.1021/acs.nanolett.2c02013.

(134) Zhu, Y.; Yang, J.; Abad-Arredondo, J.; Fernández-Domínguez, A. I.; Garcia-Vidal, F. J.; Natelson, D. Electroluminescence as a Probe of Strong Exciton–Plasmon Coupling in Few-Layer WSe2. *Nano Lett* **2024**, *24* (1), 525–532. https://doi.org/10.1021/acs.nanolett.3c04684.

(135) Liao, S.; Zhu, Y.; Ye, Q.; Sanders, S.; Yang, J.; Alabastri, A.; Natelson, D. Quantifying Efficiency of Remote Excitation for Surface-Enhanced Raman

Spectroscopy in Molecular Junctions. *J Phys Chem Lett* **2023**, *14* (33), 7574–7580. https://doi.org/10.1021/acs.jpclett.3c01948.

(136) Song, H.; Kim, Y.; Jang, Y. H.; Jeong, H.; Reed, M. A.; Lee, T. Observation of Molecular Orbital Gating. *Nature* **2009**, *462* (7276), 1039–1043. https://doi.org/10.1038/nature08639.

(137) Song, H.; Kim, Y.; Ku, J.; Jang, Y. H.; Jeong, H.; Lee, T. Vibrational Spectra of Metal-Molecule-Metal Junctions in Electromigrated Nanogap Electrodes by Inelastic Electron Tunneling. *Appl Phys Lett* **2009**, *94* (10). https://doi.org/10.1063/1.3097217.

(138) Hutchison, J. A.; Centeno, S. P.; Odaka, H.; Fukumura, H.; Hofkens, J.; Uji-i, H. Subdiffraction Limited, Remote Excitation of Surface Enhanced Raman Scattering. *Nano Lett* **2009**, *9* (3), 995–1001. https://doi.org/10.1021/nl8030696.

(139) Ma, X.; Zhu, Y.; Yu, N.; Kim, S.; Liu, Q.; Apontti, L.; Xu, D.; Yan, R.; Liu, M. Toward High-Contrast Atomic Force Microscopy-Tip-Enhanced Raman Spectroscopy Imaging: Nanoantenna-Mediated Remote-Excitation on Sharp-Tip Silver Nanowire Probes. *Nano Lett* **2019**, *19* (1), 100–107. https://doi.org/10.1021/acs.nanolett.8b03399.

(140) Evans, C. I.; Zolotavin, P.; Alabastri, A.; Yang, J.; Nordlander, P.; Natelson, D. Quantifying Remote Heating from Propagating Surface Plasmon Polaritons.

Nano Lett **2017**, *17* (9), 5646–5652. https://doi.org/10.1021/acs.nanolett.7b02524.

(141) Evans, C. I.; Natelson, D. Remote Excitation of Hot Electrons via Propagating Surface Plasmons. *Journal of Physical Chemistry C* **2019**, *123* (15), 10057–10064. https://doi.org/10.1021/acs.jpcc.9b01174.

(142) Lee, Y. J.; Jeon, I. C.; Paik, W.; Kim, K. Self-Assembly of 1,2-Benzenedithiol on Gold and Silver: Fourier Transform Infrared Spectroscopy and Quartz Crystal Microbalance Study. *Langmuir* **1996**, *12* (24), 5830–5837. https://doi.org/10.1021/la9603131.

(143) Love, J. C.; Estroff, L. A.; Kriebel, J. K.; Nuzzo, R. G.; Whitesides, G. M. Self-Assembled Monolayers of Thiolates on Metals as a Form of Nanotechnology. *Chem Rev* **2005**, *105* (4), 1103–1170. https://doi.org/10.1021/cr0300789.

(144) Joo, S. W.; Han, S. W.; Kim, K. Adsorption of 1,4-Benzenedithiol on Gold and Silver Surfaces: Surface-Enhanced Raman Scattering Study. *J Colloid Interface Sci* **2001**, *240* (2), 391–399. https://doi.org/10.1006/jcis.2001.7692.

(145) Cho, S. H.; Han, H. S.; Jang, D.; Kim, K.; Kim, M. S. Raman Spectroscopic Study of 1 , 4-Benzenedithiol Adsorbed. **1995**, 10594–10599.

(146) Suzuki, S.; Kaneko, S.; Fujii, S.; Marqués-González, S.; Nishino, T.; Kiguchi, M. Effect of the Molecule-Metal Interface on the Surface-Enhanced Raman

Scattering of 1,4-Benzenedithiol. *Journal of Physical Chemistry C* **2016**, *120* (2), 1038–1042. https://doi.org/10.1021/acs.jpcc.5b10385.

(147) Lombardi, A.; Schmidt, M. K.; Weller, L.; Deacon, W. M.; Benz, F.; de Nijs, B.; Aizpurua, J.; Baumberg, J. J. Pulsed Molecular Optomechanics in Plasmonic Nanocavities: From Nonlinear Vibrational Instabilities to Bond-Breaking. *Phys Rev X* **2018**, *8* (1), 11016. https://doi.org/10.1103/PhysRevX.8.011016.

(148) Benner, D.; Boneberg, J.; Nürnberger, P.; Waitz, R.; Leiderer, P.; Scheer, E. Lateral and Temporal Dependence of the Transport through an Atomic Gold Contact under Light Irradiation: Signature of Propagating Surface Plasmon Polaritons. *Nano Lett* **2014**, *14* (9), 5218–5223. https://doi.org/10.1021/nl502165y.

(149) Viets, C.; Hill, W. Laser Power Effects in SERS Spectroscopy at Thin Metal Films. *J Phys Chem B* **2001**, *105* (27), 6330–6336. https://doi.org/10.1021/jp004315c.

(150) Xu, H.; Bjerneld, E. J.; Käll, M.; Börjesson, L. Spectroscopy of Single Hemoglobin Molecules by Surface Enhanced Raman Scattering. *Phys Rev Lett* **1999**, *83* (21), 4357–4360. https://doi.org/10.1103/PhysRevLett.83.4357.

(151) Wang, Z.; Rothberg, L. J. Origins of Blinking in Single-Molecule Raman Spectroscopy. *J Phys Chem B* **2005**, *109* (8), 3387–3391. https://doi.org/10.1021/jp0460947.

(152) Itoh, T.; Iga, M.; Tamaru, H.; Yoshida, K.; Biju, V.; Ishikawa, M. Quantitative Evaluation of Blinking in Surface Enhanced Resonance Raman Scattering and Fluorescence by Electromagnetic Mechanism. *J Chem Phys* **2012**, *136* (2), 024703. https://doi.org/10.1063/1.3675567.

(153) Konishi, T.; Kiguchi, M.; Takase, M.; Nagasawa, F.; Nabika, H.; Ikeda, K.; Uosaki, K.; Ueno, K.; Misawa, H.; Murakoshi, K. Single Molecule Dynamics at a Mechanically Controllable Break Junction in Solution at Room Temperature. *J Am Chem Soc* **2013**, *135* (3), 1009–1014. https://doi.org/10.1021/ja307821u.

(154) González-Díaz, J. B.; Sepúlveda, B.; García-Martín, A.; Armelles, G. Cobalt Dependence of the Magneto-Optical Response in Magnetoplasmonic Nanodisks. *Appl Phys Lett* **2010**, *97* (4), 043114. https://doi.org/10.1063/1.3474617.

(155) Armelles, G.; Cebollada, A.; García-Martín, A.; González, M. U. Magnetoplasmonics: Combining Magnetic and Plasmonic Functionalities. *Adv Opt Mater* **2013**, *1* (1), 10–35. https://doi.org/https://doi.org/10.1002/adom.201200011.

(156) Sepúlveda, B.; González-Díaz, J. B.; García-Martín, A.; Lechuga, L. M.; Armelles, G. Plasmon-Induced Magneto-Optical Activity in Nanosized Gold Disks. *Phys Rev Lett* **2010**, *104* (14), 147401. https://doi.org/10.1103/PhysRevLett.104.147401.

(157) Weick, G.; Weinmann, D. Lifetime of the Surface Magnetoplasmons in Metallic Nanoparticles. *Phys Rev B* **2011**, *83* (12), 125405. https://doi.org/10.1103/PhysRevB.83.125405.

(158) Yu, Z.; Veronis, G.; Wang, Z.; Fan, S. One-Way Electromagnetic Waveguide Formed at the Interface between a Plasmonic Metal under a Static Magnetic Field and a Photonic Crystal. *Phys Rev Lett* **2008**, *100* (2), 23902. https://doi.org/10.1103/PhysRevLett.100.023902.

(159) Johnson, P. B.; Christy, R. W. Optical Constants of the Noble Metals. *Phys Rev B* **1972**, *6* (12), 4370–4379. https://doi.org/10.1103/PhysRevB.6.4370.

(160) Xia, T. K.; Hui, P. M.; Stroud, D. Theory of Faraday Rotation in Granular Magnetic Materials. *J Appl Phys* **1990**, *67* (6), 2736–2741. https://doi.org/10.1063/1.345438.

(161) Stern, E. A.; McGroddy, J. C.; Harte, W. E. Polar Reflection Faraday Effect in Metals. *Physical Review* **1964**, *135* (5A), A1306–A1314. https://doi.org/10.1103/PhysRev.135.A1306.

(162) Petta, J. R.; Ralph, D. C. Studies of Spin-Orbit Scattering in Noble-Metal Nanoparticles Using Energy-Level Tunneling Spectroscopy. *Phys Rev Lett* **2001**, *87* (26), 266801. https://doi.org/10.1103/PhysRevLett.87.266801.

(163) Wang, X.; Tang, Z. Circular Dichroism Studies on Plasmonic Nanostructures. *Small* **2017**, *13* (1), 1601115. https://doi.org/https://doi.org/10.1002/smll.201601115.

(164) Fan, Z.; Govorov, A. O. Plasmonic Circular Dichroism of Chiral Metal Nanoparticle Assemblies. *Nano Lett* **2010**, *10* (7), 2580–2587. https://doi.org/10.1021/nl101231b.

(165) Govorov, A. O.; Fan, Z.; Hernandez, P.; Slocik, J. M.; Naik, R. R. Theory of Circular Dichroism of Nanomaterials Comprising Chiral Molecules and Nanocrystals: Plasmon Enhancement, Dipole Interactions, and Dielectric Effects. *Nano Lett* **2010**, *10* (4), 1374–1382. https://doi.org/10.1021/nl100010v.

(166) Zhang, Q.; Hernandez, T.; Smith, K. W.; Hosseini Jebeli, S. A.; Dai, A. X.; Warning, L.; Baiyasi, R.; McCarthy, L. A.; Guo, H.; Chen, D.-H.; Dionne, J. A.; Landes, C. F.; Link, S. Unraveling the Origin of Chirality from Plasmonic Nanoparticle-Protein Complexes. *Science (1979)* **2019**, *365* (6460), 1475–1478. https://doi.org/10.1126/science.aax5415.

(167) Liao, S.; Song, Y.; Yu, S.; Taylor, L. W.; Dewey, O. S.; Pasquali, M.; Kono, J.; Wehmeyer, G.; Natelson, D. Understanding the Local Seebeck Coefficient of Carbon Nanotube Fibers Using the Photothermoelectric Effect. *ACS Appl Electron Mater* **2024**, *6* (11), 8000–8007. https://doi.org/10.1021/acsaelm.4c01343.

(168) Komatsu, N.; Ichinose, Y.; Dewey, O. S.; Taylor, L. W.; Trafford, M. A.; Yomogida, Y.; Wehmeyer, G.; Pasquali, M.; Yanagi, K.; Kono, J. Macroscopic Weavable Fibers of Carbon Nanotubes with Giant Thermoelectric Power Factor. *Nat Commun* **2021**, *12* (1), 4931. https://doi.org/10.1038/s41467-021-25208-z.

(169) Duan, J.; Wang, X.; Lai, X.; Li, G.; Watanabe, K.; Taniguchi, T.; Zebarjadi, M.; Andrei, E. Y. High Thermoelectricpower Factor in Graphene/HBN Devices. *Proceedings of the National Academy of Sciences* **2016**, *113* (50), 14272–14276. https://doi.org/10.1073/pnas.1615913113.

(170) Shimizu, S.; Shiogai, J.; Takemori, N.; Sakai, S.; Ikeda, H.; Arita, R.; Nojima, T.; Tsukazaki, A.; Iwasa, Y. Giant Thermoelectric Power Factor in Ultrathin FeSe Superconductor. *Nat Commun* **2019**, *10* (1), 825. https://doi.org/10.1038/s41467-019-08784-z.

(171) Mikhalchan, A.; Banas, A. M.; Banas, K.; Borkowska, A. M.; Nowakowski, M.; Breese, M. B. H.; Kwiatek, W. M.; Paluszkiewicz, C.; Tay, T. E. Revealing Chemical Heterogeneity of CNT Fiber Nanocomposites via Nanoscale Chemical Imaging. *Chemistry of Materials* **2018**, *30* (6), 1856–1864. https://doi.org/10.1021/acs.chemmater.7b04065.

(172) Wood, C. D.; Palmeri, M. J.; Putz, K. W.; Ho, G.; Barto, R.; Catherine Brinson, L. Nanoscale Structure and Local Mechanical Properties of Fiber-Reinforced Composites Containing MWCNT-Grafted Hybrid Glass Fibers. *Compos Sci*

Technol **2012**, *72* (14), 1705–1710. https://doi.org/https://doi.org/10.1016/j.compscitech.2012.06.008.

(173) St-Antoine, B. C.; Ménard, D.; Martel, R. Position Sensitive Photothermoelectric Effect in Suspended Single-Walled Carbon Nanotube Films. *Nano Lett* **2009**, *9* (10), 3503–3508. https://doi.org/10.1021/nl901696j.

(174) Xu, S.; Zobeiri, H.; Hunter, N.; Zhang, H.; Eres, G.; Wang, X. Photocurrent in Carbon Nanotube Bundle: Graded Seebeck Coefficient Phenomenon. *Nano Energy* **2021**, *86*, 106054. https://doi.org/https://doi.org/10.1016/j.nanoen.2021.106054.

(175) He, X.; Wang, X.; Nanot, S.; Cong, K.; Jiang, Q.; Kane, A. A.; Goldsmith, J. E. M.; Hauge, R. H.; Léonard, F.; Kono, J. Photothermoelectric p–n Junction Photodetector with Intrinsic Broadband Polarimetry Based on Macroscopic Carbon Nanotube Films. *ACS Nano* **2013**, *7* (8), 7271–7277. https://doi.org/10.1021/nn402679u.

(176) Erikson, K. J.; He, X.; Talin, A. A.; Mills, B.; Hauge, R. H.; Iguchi, T.; Fujimura, N.; Kawano, Y.; Kono, J.; Léonard, F. Figure of Merit for Carbon Nanotube Photothermoelectric Detectors. *ACS Nano* **2015**, *9* (12), 11618–11627. https://doi.org/10.1021/acsnano.5b06160.

(177) Zubair, A.; Wang, X.; Mirri, F.; Tsentalovich, D. E.; Fujimura, N.; Suzuki, D.; Soundarapandian, K. P.; Kawano, Y.; Pasquali, M.; Kono, J. Carbon Nanotube

Woven Textile Photodetector. *Phys Rev Mater* **2018**, *2* (1), 15201. https://doi.org/10.1103/PhysRevMaterials.2.015201.

(178) Tsentalovich, D. E.; Ma, A. W. K.; Lee, J. A.; Behabtu, N.; Bengio, E. A.; Choi, A.; Hao, J.; Luo, Y.; Headrick, R. J.; Green, M. J.; Talmon, Y.; Pasquali, M. Relationship of Extensional Viscosity and Liquid Crystalline Transition to Length Distribution in Carbon Nanotube Solutions. *Macromolecules* **2016**, *49* (2), 681–689. https://doi.org/10.1021/acs.macromol.5b02054.

(179) Behabtu, N.; Young, C. C.; Tsentalovich, D. E.; Kleinerman, O.; Wang, X.; Ma, A. W. K.; Bengio, E. A.; ter Waarbeek, R. F.; de Jong, J. J.; Hoogerwerf, R. E.; Fairchild, S. B.; Ferguson, J. B.; Maruyama, B.; Kono, J.; Talmon, Y.; Cohen, Y.; Otto, M. J.; Pasquali, M. Strong, Light, Multifunctional Fibers of Carbon Nanotubes with Ultrahigh Conductivity. *Science (1979)* **2013**, *339* (6116), 182–186. https://doi.org/10.1126/science.1228061.

(180) Tsentalovich, D. E.; Headrick, R. J.; Mirri, F.; Hao, J.; Behabtu, N.; Young, C. C.; Pasquali, M. Influence of Carbon Nanotube Characteristics on Macroscopic Fiber Properties. *ACS Appl Mater Interfaces* **2017**, *9* (41), 36189–36198. https://doi.org/10.1021/acsami.7b10968.

(181) Maultzsch, J.; Telg, H.; Reich, S.; Thomsen, C. Radial Breathing Mode of Single-Walled Carbon Nanotubes: Optical Transition Energies and Chiral-Index Assignment. *Phys Rev B* **2005**, *72* (20), 205438. https://doi.org/10.1103/PhysRevB.72.205438.

(182) Liu, Y.; Hu, Q.; Cao, Y.; Wang, P.; Wei, J.; Wu, W.; Wang, J.; Huang, F.; Sun, J.-L. High-Performance Ultrabroadband Photodetector Based on Photothermoelectric Effect. *ACS Appl Mater Interfaces* **2022**, *14* (25), 29077–29086. https://doi.org/10.1021/acsami.2c03925.

(183) Freitag, M.; Martin, Y.; Misewich, J. A.; Martel, R.; Avouris, Ph. Photoconductivity of Single Carbon Nanotubes. *Nano Lett* **2003**, *3* (8), 1067–1071. https://doi.org/10.1021/nl034313e.

(184) Nanot, S.; Cummings, A. W.; Pint, C. L.; Ikeuchi, A.; Akiho, T.; Sueoka, K.; Hauge, R. H.; Léonard, F.; Kono, J. Broadband, Polarization-Sensitive Photodetector Based on Optically-Thick Films of Macroscopically Long, Dense and Aligned Carbon Nanotubes. *Sci Rep* **2013**, *3* (1), 1335. https://doi.org/10.1038/srep01335.

(185) Tristant, D.; Zubair, A.; Puech, P.; Neumayer, F.; Moyano, S.; Headrick, R. J.; Tsentalovich, D. E.; Young, C. C.; Gerber, I. C.; Pasquali, M.; Kono, J.; Leotin, J. Enlightening the Ultrahigh Electrical Conductivities of Doped Double-Wall Carbon Nanotube Fibers by Raman Spectroscopy and First-Principles Calculations. *Nanoscale* **2016**, *8* (47), 19668–19676. https://doi.org/10.1039/C6NR04647A.

(186) Si, C.; Sun, Z.; Liu, F. Strain Engineering of Graphene: A Review. *Nanoscale* **2016**, *8* (6), 3207–3217. https://doi.org/10.1039/C5NR07755A.

(187) Mohr, M.; Maultzsch, J.; Thomsen, C. Splitting of the Raman $2D$ Band of Graphene Subjected to Strain. *Phys Rev B* **2010**, *82* (20), 201409. https://doi.org/10.1103/PhysRevB.82.201409.

(188) Reich, S.; Jantoljak, H.; Thomsen, C. Shear Strain in Carbon Nanotubes under Hydrostatic Pressure. *Phys Rev B* **2000**, *61* (20), R13389–R13392. https://doi.org/10.1103/PhysRevB.61.R13389.

(189) Costa, S. D.; Fantini, C.; Righi, A.; Bachmatiuk, A.; Rümmeli, M. H.; Saito, R.; Pimenta, M. A. Resonant Raman Spectroscopy on Enriched 13C Carbon Nanotubes. *Carbon N Y* **2011**, *49* (14), 4719–4723. https://doi.org/https://doi.org/10.1016/j.carbon.2011.06.076.

(190) Das, A.; Sood, A. K.; Govindaraj, A.; Saitta, A. M.; Lazzeri, M.; Mauri, F.; Rao, C. N. R. Doping in Carbon Nanotubes Probed by Raman and Transport Measurements. *Phys Rev Lett* **2007**, *99* (13), 136803. https://doi.org/10.1103/PhysRevLett.99.136803.

(191) Brown, S. D. M.; Jorio, A.; Corio, P.; Dresselhaus, M. S.; Dresselhaus, G.; Saito, R.; Kneipp, K. Origin of the Breit-Wigner-Fano Lineshape of the Tangential G-Band Feature of Metallic Carbon Nanotubes. *Phys Rev B* **2001**, *63* (15), 155414. https://doi.org/10.1103/PhysRevB.63.155414.

(192) Jorio, A.; Saito, R. Raman Spectroscopy for Carbon Nanotube Applications. *J Appl Phys* **2021**, *129* (2), 021102. https://doi.org/10.1063/5.0030809.

(193) Das, A.; Pisana, S.; Chakraborty, B.; Piscanec, S.; Saha, S. K.; Waghmare, U. V; Novoselov, K. S.; Krishnamurthy, H. R.; Geim, A. K.; Ferrari, A. C.; Sood, A. K. Monitoring Dopants by Raman Scattering in an Electrochemically Top-Gated Graphene Transistor. *Nat Nanotechnol* **2008**, *3* (4), 210–215. https://doi.org/10.1038/nnano.2008.67.

(194) Sasaki, K.; Saito, R.; Dresselhaus, G.; Dresselhaus, M. S.; Farhat, H.; Kong, J. Curvature-Induced Optical Phonon Frequency Shift in Metallic Carbon Nanotubes. *Phys Rev B* **2008**, *77* (24), 245441. https://doi.org/10.1103/PhysRevB.77.245441.

(195) Hároz, E. H.; Duque, J. G.; Rice, W. D.; Densmore, C. G.; Kono, J.; Doorn, S. K. Resonant Raman Spectroscopy of Armchair Carbon Nanotubes: Absence of Broad ${G}^{\ensuremath{-}}$ Feature. *Phys Rev B* **2011**, *84* (12), 121403. https://doi.org/10.1103/PhysRevB.84.121403.

(196) Hu, S.; Liu, B.-J.; Feng, J.-M.; Zong, C.; Lin, K.-Q.; Wang, X.; Wu, D.-Y.; Ren, B. Quantifying Surface Temperature of Thermoplasmonic Nanostructures. *J Am Chem Soc* **2018**, *140* (42), 13680–13686. https://doi.org/10.1021/jacs.8b06083.

(197) Ngo, D. N.; Ho, V. T. T. X.; Kim, G.; Song, M. S.; Kim, M. R.; Choo, J.; Joo, S.-W.; Lee, S. Y. Raman Thermometry Nanopipettes in Cancer Photothermal Therapy. *Anal Chem* **2022**, *94* (17), 6463–6472. https://doi.org/10.1021/acs.analchem.1c04452.

(198) Qiu, L.; Wang, X.; Tang, D.; Zheng, X.; Norris, P. M.; Wen, D.; Zhao, J.; Zhang, X.; Li, Q. Functionalization and Densification of Inter-Bundle Interfaces for Improvement in Electrical and Thermal Transport of Carbon Nanotube Fibers. *Carbon N Y* **2016**, *105*, 248–259. https://doi.org/https://doi.org/10.1016/j.carbon.2016.04.043.

(199) Moon, J.; Weaver, K.; Feng, B.; Gi Chae, H.; Kumar, S.; Baek, J.-B.; Peterson, G. P. Note: Thermal Conductivity Measurement of Individual Poly(Ether Ketone)/Carbon Nanotube Fibers Using a Steady-State Dc Thermal Bridge Method. *Review of Scientific Instruments* **2012**, *83* (1), 016103. https://doi.org/10.1063/1.3676650.

(200) Dames, C.; Chen, G. 1ω,2ω, and 3ω Methods for Measurements of Thermal Properties. *Review of Scientific Instruments* **2005**, *76* (12), 124902. https://doi.org/10.1063/1.2130718.

(201) Martin, J. J.; Sidles, P. H.; Danielson, G. C. Thermal Diffusivity of Platinum from 300° to 1200°K. *J Appl Phys* **1967**, *38* (8), 3075–3078. https://doi.org/10.1063/1.1710065.

(202) Li, M.; Xu, S.; Chen, Q.; Zheng, L.-R. Thermoelectric-Generator-Based DC–DC Conversion Networks for Automotive Applications. *J Electron Mater* **2011**, *40* (5), 1136–1143. https://doi.org/10.1007/s11664-011-1557-5.

(203) Parzefall, M. Optical Antennas Driven by Quantum Tunneling, ETH, Zurich, 2017. https://doi.org/10.3929/ethz-a-010868934 (accessed 2025-09-16).

(204) Abad-Arredondo, J. Light-Matter Interactions at the Nanoscale. Non-Linearities, Electrons and Exciton Polaritons, Universidad Autónoma de Madrid, Madrid, 2025. http://hdl.handle.net/10486/719994 (accessed 2025-09-16).

(205) Abad-Arredondo, J.; Fernández-Domínguez, A. I. Electron-Assisted Probing of Polaritonic Light–Matter States. *Nanophotonics* **2024**, *13* (11), 2015–2027. https://doi.org/10.1515/nanoph-2023-0907.

(206) Novotny, L.; Hecht, B. *Principles of Nano-Optics*; 2009. https://doi.org/10.1017/CBO9780511794193.

(207) Fan, L.; Zang, W.; Yang, X.; Zhan, P.; Chen, Z.; Wang, Z.; Schuller, J. A.; Barnard, E. S.; Cai, W.; Jun, Y. C.; White, J. S.; Brongersma, M. L.; Maier, A.; Halas, N. J.; Nordlander, P.; Giessen, H.; Chong, C. T.; Kim, S.; Jin, J.; Kim, Y. J.; Park, I. Y.; Kim, Y.; Kim, S. W.; Nijs, de; Benz, F.; Barrow, S. J.; Scherman, O. A.; Rosta, E.; Demetriadou, A.; Fox, P.; Hess, O.; Baumberg, J. J.; Aouani, H.; Rahmani, M.; Navarro-Cía, M.; Maier, S. A.; Sundaramurthy, A.; Crozier, K. B.; Kino, G. S.; Fromm, D. P.; Schuck, P. J.; Moerner, W. E.; Ciracì, C.; Hill, R. T.; Mock, J. J.; Urzhumov, Y.; Fernández-Domínguez, A. I.; Pendry, J. B.; Chilkoti, A.; Smith, D. R.; Park, H. Second Harmonic Generation Enhancement from a Nonlinear Nanocrystal Integrated Hyperbolic Metamaterial Cavity. *Optics Express, Vol.*

25, Issue 18, pp. 21342-21348 **2017**, *25* (18), 21342–21348. https://doi.org/10.1364/OE.25.021342.

(208) Ciracì, C.; Della Sala, F. Quantum Hydrodynamic Theory for Plasmonics: Impact of the Electron Density Tail. *Phys Rev B* **2016**, *93* (20), 205405. https://doi.org/10.1103/PhysRevB.93.205405.

(209) Toscano, G.; Straubel, J.; Kwiatkowski, A.; Rockstuhl, C.; Evers, F.; Xu, H.; Asger Mortensen, N.; Wubs, M. Resonance Shifts and Spill-out Effects in Self-Consistent Hydrodynamic Nanoplasmonics. *Nat Commun* **2015**, *6* (1), 7132. https://doi.org/10.1038/ncomms8132.

(210) Johnson, P. B.; Christy, R. W. Optical Constants of the Noble Metals. *Phys Rev B* **1972**, *6* (12), 4370–4379. https://doi.org/10.1103/PhysRevB.6.4370.

Appendix A

Calculation about SPPs in Vacuum-Au-SiO_2 system

The electric and magnetic field in the three regions (mentioned in the main text Chapter 3) can be calculated:[1]

Region 3:

$$H_y = Ae^{i\beta x}e^{-k_3 z}$$

$$E_x = iA\frac{1}{\omega\varepsilon_0\varepsilon_3}k_3 e^{i\beta x}e^{-k_3 z}$$

$$E_z = -A\frac{\beta}{\omega\varepsilon_0\varepsilon_3}e^{i\beta x}e^{-k_3 z}$$

Region 1:

$$H_y = Ce^{i\beta x}e^{k_1 z} + De^{i\beta x}e^{-k_1 z}$$

$$E_x = -iC\frac{1}{\omega\varepsilon_0\varepsilon_1}k_1 e^{i\beta x}e^{k_1 z} + iD\frac{1}{\omega\varepsilon_0\varepsilon_1}k_1 e^{i\beta x}e^{-k_1 z}$$

$$E_z = C\frac{\beta}{\omega\varepsilon_0\varepsilon_1}e^{i\beta x}e^{k_1 z} + D\frac{\beta}{\omega\varepsilon_0\varepsilon_1}e^{i\beta x}e^{-k_1 z}$$

Region 2:

$$H_y = Be^{i\beta x}e^{k_2 z}$$

$$E_x = -iB\frac{1}{\omega\varepsilon_0\varepsilon_2}k_2 e^{i\beta x}e^{k_2 z}$$

$$E_z = -B\frac{\beta}{\omega\varepsilon_0\varepsilon_2}e^{i\beta x}e^{k_2 z}$$

where k_1, k_2, k_3 are the wave vectors in region 1, 2, 3 in z direction respectively. β is the wave vector in SPPs propagation direction. ε_1, ε_2, ε_3 are the dielectric function in region 1, 2, 3 respectively. ω is the frequency of the input light.

Consider the continuity of H_y and E_x, we have:

$$Ae^{-k_3 a} = Ce^{k_1 a} + De^{-k_1 a}$$

$$\frac{A}{\varepsilon_3}k_3 e^{-k_3 a} = -\frac{C}{\varepsilon_1}k_1 e^{k_1 a} + \frac{D}{\varepsilon_1}k_1 e^{-k_1 a}$$

$$Be^{-k_2 a} = Ce^{-k_1 a} + De^{k_1 a}$$

$$-\frac{B}{\varepsilon_2}k_2 e^{-k_2 a} = -\frac{C}{\varepsilon_1}k_1 e^{-k_1 a} + \frac{D}{\varepsilon_1}k_1 e^{k_1 a}$$

$2a = 30\ nm$ is the thickness of Au. Then we get the dispersion relation:

$$e^{-4k_1 a} = \frac{{k_1}/{\varepsilon_1} + {k_2}/{\varepsilon_2}}{{k_1}/{\varepsilon_1} - {k_2}/{\varepsilon_2}} \cdot \frac{{k_1}/{\varepsilon_1} + {k_3}/{\varepsilon_3}}{{k_1}/{\varepsilon_1} - {k_3}/{\varepsilon_3}} \quad (A-1)$$

The wave equation for TM modes is:

$$\frac{\partial^2 H_y}{\partial z^2} + (k_0^2\varepsilon - \beta^2)H_y = 0$$

We have:

$$k_i^2 = \beta^2 - k_0^2 \varepsilon_i \quad i = 1, 2, 3 \quad (A-2)$$

k_0 is the wave vector of the input laser. The value of dielectric functions are determined by the material: $\varepsilon_1 = -20.669 + 1.4246i$, $\varepsilon_2 = 2.113$, $\varepsilon_3 = 1$. By solving equations (1) and (2), we get every wave vector in this system:

$$k_1 = 3.858 \times 10^7 + 1.139 \times 10^6 i$$

$$k_2 = 5.25 \times 10^6 + 3.256 \times 10^5 i$$

$$k_3 = 9.94 \times 10^6 + 1.720 \times 10^5 i$$

$$\beta = 1.276 \times 10^7 + 1.339 \times 10^5 i$$

Appendix B

COMSOL model for direct and remote excitation

Finite elements method (FEM) simulation is done using COMSOL Multiphysics 6.1. The geometry of the model (Figure A1) is defined as the description in the main text of the article. To simplify the model, we only consider the grating at one side. The model is surrounded by perfect match layers (PML). The simulation is performed in wave optics module electromagnetic wave frequency domain (ewfd) section with two steps: the first step defines the background Gaussian beam input laser, and the second step calculates the scattering electric field.

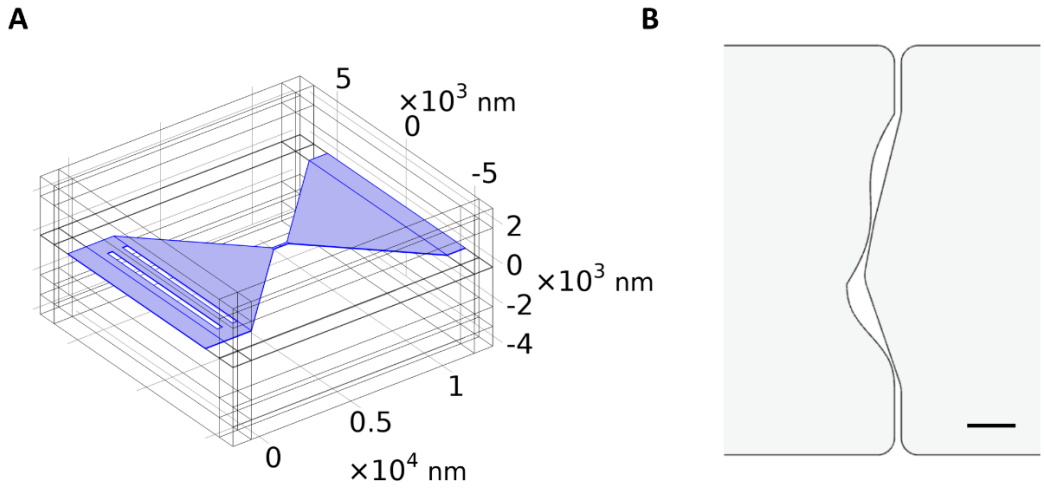

Figure A1: (A) Geometry of the whole model. The Au layer is colored in blue. (B) The geometry of the junction gap. Scale bar is 15 nm.

Simulated energy flow

The energy flow from the grating to the junction (Figure A2) is calculated by integrating the Poynting vector along x (propagation) direction over an area in the y-z plane, as shown in Figure A2. The rectangular area contains the whole Au wire in y direction. In the z direction, the height is set to be 130 nm to include the 30 nm Au and 50 nm in both vacuum and SiO_2. The 50 nm is chosen to include most part of the SPPs as well as exclude light reflected by the gold layer. The absorption under direct excitation is calculated by integrating the Joule heat (ewfd2.Qh) over the nanowire.

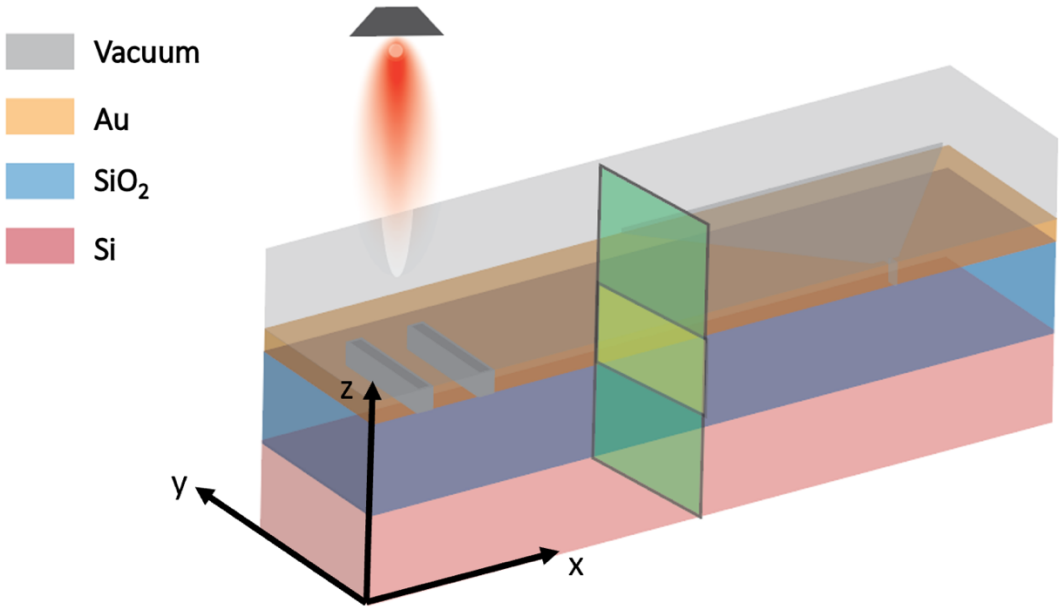

Figure A2: Scheme of energy flow calculation. The x component of the Poynting vector is integrated over the area indicated by the yellow rectangular in y-z plane.

Appendix C

Details of Derivation of PTE temperature profile

As described in the main text Chapter 5, we consider 1D steady-state heat conduction in the axial x direction of the CNTF due to point source heating from a laser beam. To justify the steady-state approximation, we refer to Figure 5-4B in the main text, which shows that the measured PTE voltage approaches a chopper-frequency independent value for chopper time periods > 20 ms. Because this heating period is substantially larger than thermal time constant, transient heat conduction effects are negligible, and the steady-state model is appropriate to describe the amplitude of the temperature rise in response to the square wave heating; to use the model in describing the experiment, we further account for the fact that the lock-in signal selects out the rms component of the voltage at the fundamental harmonic. The dwell time at a given beam location is also substantially longer than the heating period in all cases, as required for lock-in detection. The 1D model is appropriate because the fiber diameter (17.5 μm) is small compared to the length of the fiber (> 1 mm) and small compared to the lengthscale of the axial temperature gradient in the fiber as discussed below.

Figure 5-5A illustrates the experimental setup for the PTE measurements, which are performed in ambient air for a fiber supported on a silicon substrate with 2 μm thick SiO_2. The 1D governing energy equation including radiation, convection

and thermal contact resistance that is used to find the steady-state temperature profile $T(x)$ is

$$\frac{\mathrm{d}^2T}{\mathrm{d}x^2} = m^2(T - T_0) \quad (C-1)$$

where $m^2 \equiv \frac{1}{kA}\left(\pi Dh + \frac{1}{R_{\mathrm{contact}}}\right)$ describes the effects of the losses to the surroundings, k is the fiber axial thermal conductivity, A is the fiber cross-sectional area, D is the fiber diameter, h is the heat transfer coefficient describing the combined effects of convection to the nearby air and radiation to the surroundings, R_{contact} is the thermal contact resistance for a unit length between the CNTF and the silicon substrate (units of K. m/W), and T_0 is the ambient temperature (i.e., far-field temperature of the silicon substrate, air near the fiber, and the surroundings). For a fiber of length L, the non-dimensional fin parameter mL describes the relative importance of radiative, convective and contact losses as compared to axial conduction; the temperature profile is spatially extended over the length of the fiber if $mL \ll 1$, and the temperature profile is localized near the heat source if $mL \gg 1$. We directly measure m in a separate Joule heating/resistance thermometry experiment described in the next part.

The laser beam impinges on the sample at a location $x = x_0$ with an absorbed laser power P (Figure 5-5A). We determine the incident laser power at the sample location using a power meter, and assume that the CNTF fully absorbs the incident power. To simplify the equations, different from the main text, we suppose the origin

is at the center of the CNTF. We divide the solution of the equation into a left regime $T_{\text{left}}(x)$ defined over a range from $[-\frac{L}{2}, x_0)$ and a right regime $T_{\text{right}}(x)$ defined over a range from $(x_0, \frac{L}{2}]$. The regions of the CNTF at $x = -\frac{L}{2}$ and $x = \frac{L}{2}$ are connected the large silver paste electrodes and are assumed to be isothermal at the ambient temperature T_0. The boundary conditions are

$$T_{\text{left}}\left(x = -\frac{L}{2}\right) = T_0$$

$$T_{\text{right}}\left(x = \frac{L}{2}\right) = T_0$$

$$T_{\text{left}}(x = x_0) = T_{\text{right}}(x = x_0)$$

$$-kA\frac{dT_{\text{left}}}{dx}\Big|_{x=x_0} + kA\frac{dT_{\text{right}}}{dx}\Big|_{x=x_0} = P$$

The last two boundary conditions represent temperature continuity and heat flow conservation, respectively, at the laser heating location. Solving Eq. (C-**Error! Reference source not found.** by applying the boundary conditions, the position-dependent temperature rise $\Delta T(x) \equiv T(x) - T_0$ is

$$\Delta T_{\text{left}}(x) = C_1 \exp(mx) + C_2 \exp(-mx) \quad (C-2)$$

$$\Delta T_{\text{right}}(x) = C_3 \exp(mx) + C_4 \exp(-mx) \quad (C-3)$$

where the constants are:

$$C_1 = \frac{P(\exp(mL - mx_0) - \exp(mx_0))}{4kAm\sinh(mL)}$$

$$C_2 = \frac{-P(-\exp(-mL + mx_0) + \exp(-mx_0))}{4kAm\sinh(mL)}$$

$$C_3 = \frac{-P}{2kAm}\exp(-mx_0) + C_1$$

$$C_4 = -C_3 \exp(mL)$$

Characterization of fin parameter mL in the PTE experiment

As discussed in Chapter 5 and the last part, the temperature profile along the CNTF in the PTE experiment depends on the fin parameter m. This parameter captures the effects of radiation, convection, axial heat conduction along the fiber, and heat conduction across the fiber-substrate contact. We measure this fin parameter using the four-probe electrothermal experiment shown in Figure 5-5B.

We apply a DC current (Keithley 2400 SourceMeter) through the outer two electrodes ($I^+$and I^-in Figure 5-5B) to volumetrically Joule heat the CNTF, and we measure the voltage drop at the inner two electrodes ($V^+$and V^-) to extract the averaged temperature rise using resistance thermometry. We use a similar as-spun CNTF mounted on a silicon wafer as in the PTE experiment and perform the measurement in air to ensure h and R_{contact} are similar between this calibration measurement and the PTE experiment. This section derives the relation between the measured spatially averaged temperature rise and the fin parameter.

The 1D steady-state governing energy equation in this scenario is:

$$\frac{\mathrm{d}^2T(x)}{\mathrm{d}x^2} + \frac{\dot{q}}{k} = m^2(T(x) - T_0) \quad (C-4)$$

where $\dot{q} \equiv \frac{IV}{AL}$ is the position-independent volumetric energy generation rate due to local Joule heating. The regions at the inner two electrodes (V^+ and V^-) are considered to be isothermal at the ambient temperature T_0, because the large silver paste electrodes act as heat sinks. Due to the symmetry of the temperature profile, the boundary conditions are:

$$T\left(x = \frac{L}{2}\right) = T_0$$

$$\frac{dT}{dx}(x = 0) = 0$$

Using the boundary conditions along with the general solution for Eq. (C-4), we can obtain the position-dependent temperature rise $\Delta T(x) \equiv T(x) - T_0$ as

$$\Delta T(x) = \frac{\dot{q}}{km^2}\left(1 - \frac{\cosh(mx)}{\cosh\left(\frac{mL}{2}\right)}\right) \quad (C-5)$$

The resistance thermometry method measures the spatially averaged temperature rise along CNTF, and the mean temperature rise $\overline{\Delta T}$ is obtained as:

$$\overline{\Delta T} = \frac{1}{L}\int_{-\frac{L}{2}}^{\frac{L}{2}} \Delta T(x)\, dx = \frac{\dot{q}}{km^2}\left(1 - \frac{2}{mL}\tanh\left(\frac{mL}{2}\right)\right) \quad (C-6)$$

The electrical resistance of CNTFs is linearly related to the mean temperature rise $\overline{\Delta T}$ as:

$$\frac{\Delta R}{R_0} = \beta \overline{\Delta T} \quad (C-7)$$

where ΔR is the resistance increase, R_0 is the resistance of CNTF at ambient temperature T_0, and β is the temperature coefficient of resistance. The temperature coefficient β is calibrated by using the temperature controller (LakeShore 340) to isothermally heat the silicon substrate by <5 K while recording the CNTF resistance and substrate temperature. We use small temperature rises in the calibration to ensure that no additional annealing/de-doping occurs. The measured data of during heating and cooling process are consistent, which validates the quasi-steady assumption that the CNTFs and the substrate are at the same temperature. The value of β for the CNTF used in this calibration is 2300 parts per million (ppm)/K.

Combining Eq. (C-6) and Eq. (C-7), the relative electrical resistance is related to the input Joule heating power IV as

$$\frac{\Delta R}{R_0} = \frac{\beta IV}{ALkm^2}\left(1 - \frac{2}{mL}\tanh\left(\frac{mL}{2}\right)\right) \quad (C-8)$$

We use Eq. (C-8) to quantify the fin parameter m once the temperature coefficient β and the thermal conductivity are known (see the next part below). We apply a small range of bias current (-3 to +3 mA) and determine the zero-current resistance R_0 via the linear fit of the $I-V$ curve. Then, we apply a larger current range from -90 to +90 mA to the sample while recording the voltage drop. The larger current range causes a non-negligible temperature rise $\overline{\Delta T}$ and resulting resistance increase $\frac{\Delta R}{R_0} \equiv (\frac{V}{I} - R_0)/R_0$, which is linear in the Joule heating power.

Figure C-1 shows the fit of Eq. (C-8) to the experimental data, resulting in a slope of $1.99\,\frac{1}{\mathrm{W}}$. According to Eq. (C-8), the slope between Joule-heating power $P = IV$ and resistance increase $\frac{\Delta R}{R_0}$ is:

$$\text{Slope} = \frac{\beta}{ALkm^2}\left(1 - \frac{2}{mL}\tanh\left(\frac{mL}{2}\right)\right) \quad (C-9)$$

Using the known A, L, k and β of the CNTF sample, we obtained the final value of m, which we use in our modeling to determine the combined effects of convection, radiation, and substrate conduction losses in the PTE measurements. We find that the measured m of the as-spun (before annealing) and 423 K (150 °C) annealed CNTFs are $2.5 \pm 0.2 \times 10^3\ \mathrm{m}^{-1}$ and $3.0 \pm 0.2 \times 10^3\ \mathrm{m}^{-1}$ respectively, as indicated in Table 5-1.

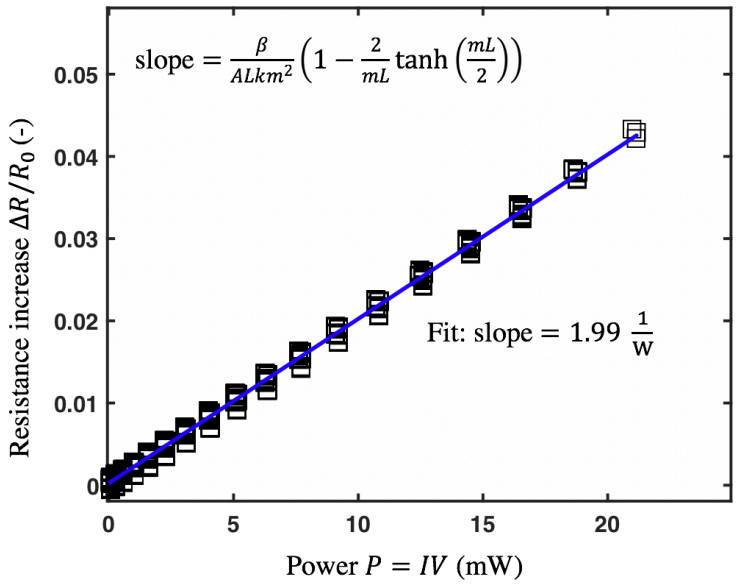

Figure C-1: Fin parameter measurement for CNTF on substrate in air showing the resistance increase $\frac{\Delta R}{R_0}$ as a function of the Joule heating power $P = IV$. The slope in Eq. (E-9) is obtained by fitting Eq. (E-8) the data, here resulting in slope = 1.99 $\frac{1}{W}$.

Thermal conductivity measurements

Figure 5-5C shows the four-probe setup for the steady-state Joule heating and the 3ω measurements to characterize the thermal conductivity of CNTF samples. In these thermal conductivity measurements, the sample is suspended over the inner two electrodes, and the measurements are performed in the vacuum chamber to eliminate losses from the sample (i.e., ensuring $mL \ll 1$ due to the vacuum condition)[198]. We performed a validation measurement on a platinum wire (Alfa

Aesar) of diameter $D = 25$ μm using both the steady-state Joule heating and 3ω methods which are extensively described by other researchers[199,200]. The validation measurement thermal conductivity $k_{\mathrm{Pt}} = 75 \pm 8 \frac{\mathrm{W}}{\mathrm{m.K}}$ (steady-state method), $k_{\mathrm{Pt}} = 80 \pm 12 \frac{\mathrm{W}}{\mathrm{m.K}}$ (3ω method) and thermal diffusivity $\alpha_{\mathrm{Pt}} = 26 \pm 4\ \mathrm{mm}^2/\mathrm{s}$ are in good agreement with the handbook values of platinum, which are 71 W/m.K and 24 mm^2/s.[201] We used the focused ion beam scanning electron microscope (Helios DualBeam FIB SEM) to obtain the cross-sectional area A of the CNTF samples. We find that the measured thermal conductivity of the as-spun (before annealing) and 423 K (150 °C) annealed CNTFs are $240 \pm 20 \frac{\mathrm{W}}{\mathrm{m.K}}$ and $290 \pm 30 \frac{\mathrm{W}}{\mathrm{m.K}}$ respectively, as indicated in Table 5-1.

With the thermal conductivity, the fin parameter m can be calculated. Then the temperature profile can be obtained, as shown in Figure 5-7A. With the temperature profile, the temperature gradient profile can be obtained analytically, as shown in Figure 5-7B.

Average Seebeck coefficient measurement

Figure 5-6 illustrates the setup used to measure the average Seebeck coefficient S_{ave} of the CNTF. The CNTF is suspended between two copper electrodes mounted on heat-sunk Peltier modules (TEC1-12706, Geebat) for temperature control. Thermal paste (ARCTIC-MX4, Arctic) is applied to all interfaces. K-type

thermocouples are placed on the upper surfaces of the electrodes, and the thermocouples are covered by a thin copper tape to prevent convection losses. Silver paste electrodes connect the two ends of CNTF to each copper bar, and we measure the open circuit voltage drop arising from the imposed temperature difference at the two ends of CNTF using a digital multimeter (Keithley DMM6500). At the beginning of the measurements under isothermal conditions, the two thermocouples are calibrated by waiting until the readings are stable and consistent with each other within the error of 0.1 ℃ (preventing unintentional offset errors). One of the Peltier module is then heated to a high temperature T_h by applying a DC current (Keithley 2200 SourceMeter), and the other one is left at ambient temperature T_c. In our experiment, the current ranges from 0.2 to 0.8 A which leads to a temperature difference from 0 to 35 K. The voltage drop is recorded after the thermocouple reading becomes stable.

Figure C-2 shows that the magnitude of the measured open-circuit voltage V_{open} scales linearly with the temperature difference $\Delta T \equiv T_h - T_c$ for as-spun (blue diamonds) and 423 K annealed (yellow squares) CNTFs. Both samples are p-type. We used a linear fit to the experimental data to obtain the average Seebeck coefficient, which is the slope in Figure S5B. The offset voltage at isothermal conditions is a relatively small value of order of magnitude 10^{-2} mV, as desired. The measured average Seebeck coefficients are 17.2 ± 0.9 μV/K for as-spun CNTF and 21.0 ± 0.3 μV/K for 423 K annealed CNTF; these reported values have been properly corrected by subtracting the Seebeck coefficients of the copper wire lead electrode, which is 1.5

μV/K at room temperature.[202] The measured Seebeck values of the as-spun CNTFs have a good agreement with previous measurements on similar CNTFs[168] that found 21.5 ± 0.2 μV/K. The thermal model parameters and the average Seebeck coefficient for both the as-spun and annealed CNTFs are shown in Table 5-1.

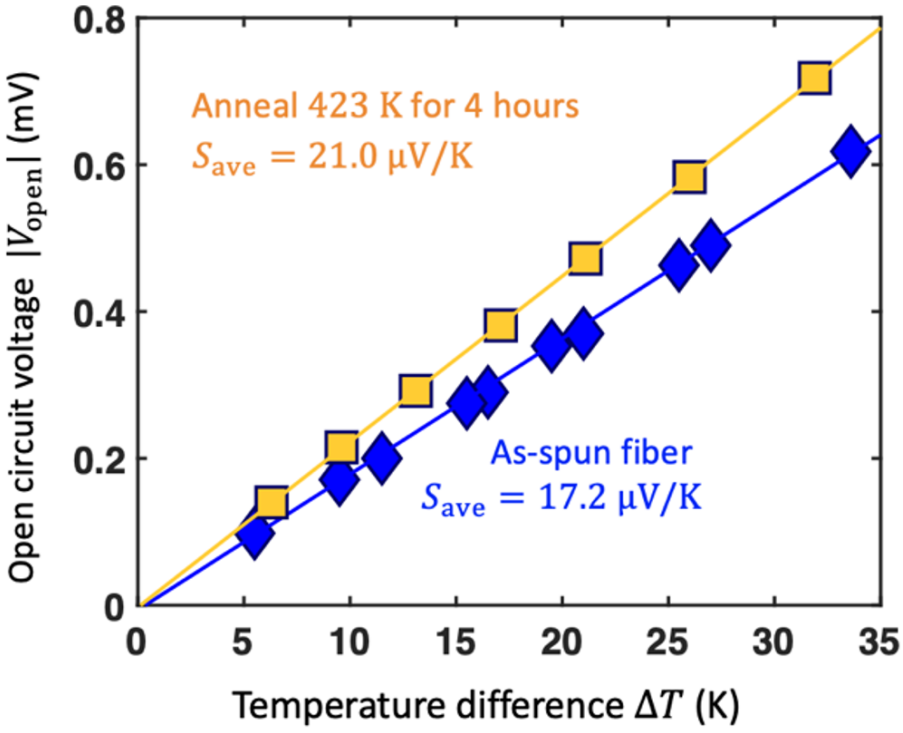

Figure C-2: The measured open circuit voltage scales linearly with the temperature difference. The average Seebeck coefficient is 17.2 ± 0.9 μV/K for as-spun CNTF and 21.0 ± 0.3 μV/K for 423 K annealed CNTF.

Appendix D

The robustness of the extraction of the Seebeck coefficient

As discussed in Chapter 5, in extracting the Seebeck coefficients used throughout this work, we use the smoothed data instead of the raw data of V. The smoothing is performed by the Matlab function smooth() with 'rloess' method using 8% of the total data to preserve the features of the PTE voltage.

We repeat the same photovoltage map measurement on the same sample three times consecutively, and the Seebeck coefficient retrieved from the three measurements is almost the same, as shown in Figure D-1. In the three measurements, the PTE voltage as a function of position is not exactly the same (Figure D-1A, C, and E) because of the hysteresis of the step motors used in the map measurements and because the laser spot positions can shift between different measurements. However, the overall shapes and the smooth curves are almost identical. As a result, the calculated Seebeck coefficient from these measurements (Figure D-1B, D, and F) has the same fluctuation features and trends. This proves our calculated Seebeck coefficient is robust upon repeated measurements of the same sample.

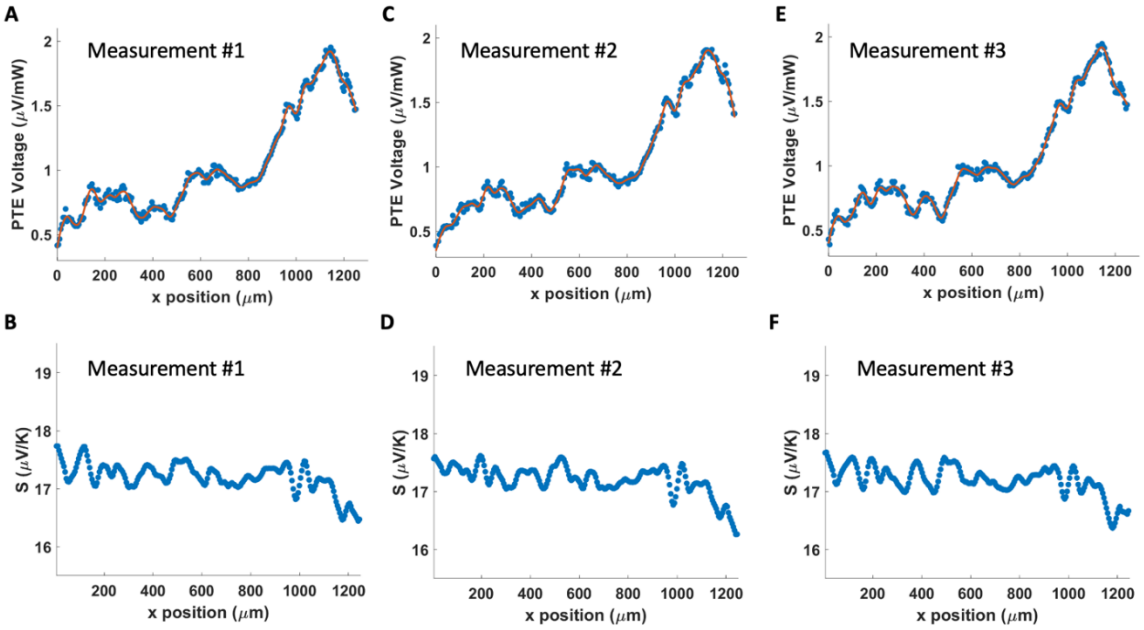

Figure D-1: The PTE voltage and the extracted Seebeck coefficient of same sample in different measurements. (A), (C) and (E) The PTE voltage as a function of position of the fiber in three different measurements performed sequentially. The PTE voltage is not exactly the same, but the smooth curves (dashed lines) have the same trend. (B), (D) and (F) The Seebeck coefficient obtained from the PTE voltage in (A), (C) and (E). The calculated Seebeck coefficient from the three measurements has the same fluctuation features and trends.

We also investigate the robustness of the calculated Seebeck coefficient against uncertainties in the thermal model. As described in **Appendix C**, the fin parameter $m = 2.5 \pm 0.2 \times 10^3$ m^{-1}, and we want to observe how uncertainties in m

propagate through the thermal model to influence the measured Seebeck coefficients. We can calculate the Seebeck coefficient based on one single PTE voltage measurement but use different m values of 2.5×10^3, 2.3×10^3 and 2.7×10^3 m^{-1}, as shown in Figure D-2. The temperature rise is slightly larger for smaller m (Figure D-2A). For the PTE measurement shown in Figure D-2A, we can solve the Seebeck coefficient using different m values, as shown in Figure D-2B. The Seebeck coefficient solved from different m in Figure D-2B almost overlaps each other, indicating that typical levels of uncertainties in the thermal model do not lead to major uncertainties in the extracted Seebeck coefficient.

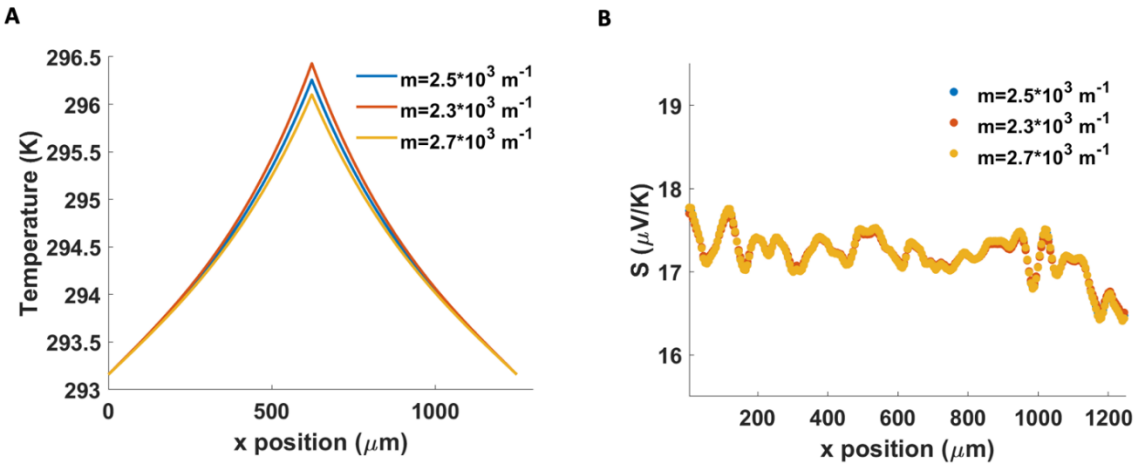

Figure D-2. The robustness of the calculated Seebeck coefficient against typical uncertainties in the thermal model. (A) Temperature profile when a 1 mW laser is shone at the center of the fiber with different fin parameter m. (B) The calculated Seebeck coefficient with different m based on the temperature in (A) shows that similar values of S are found for all cases.

We also show the robustness of the calculated Seebeck coefficient against the possible non-uniformity of the other parameters in the thermal model. Here, we consider the thermal conductivity k as an example. We note that the CNTF thermal conductivity is dominated by phonons in this temperature range, and significant local variations in k are not expected. We consider the CNTF with uniform k=240 W/(m·K) and random k ranging from 240 ± 20 W/(m·K) along the fiber. The values are taken based on Table 5-1. The temperature profiles are obtained using the finite element method simulation in COMSOL Multiphysics. Figure D-3 shows the temperature profiles of CNTF with uniform and random k excited by 1 mW laser at the center. The temperature profiles are almost the same. Considering the Eq. (5-1) and (5-2) are independent from k explicitly, with identical photovoltage V, the same temperature profile should result in the same obtained Seebeck coefficient. The non-uniformity of the other parameters (such as the diameter of the CNTF) along the fiber can be written as mathematically equivalent to the case of a nonuniform thermal conductivity. Therefore, our inferred Seebeck coefficient is robust against non-uniformity of the other parameters in the thermal model.

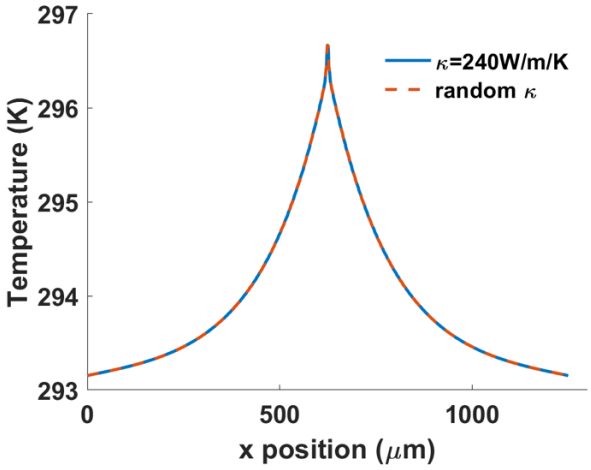

Figure D-3: The robustness of the calculated Seebeck coefficient against the non-uniformity of the thermal conductivity *k*. The temperature profiles of CNTF with uniform *k* (blue solid curve) and random *k* from 240 ± 20 W/(m·K) (orange dashed curve) are simulated. The two curves are almost identical, which means the temperature profile is robust against the non-uniformity of the thermal conductivity *k*.

From the Seebeck coefficient as a function of position x, we can numerically obtain the derivative of S, dS/dx. On the other hand, the photovoltage can be written as:

$$V(x_0) = -\int_0^L S(x)\nabla T(x,x_0)dx = S(0)T(0) - S(L)T(L) + \int_0^L \frac{dS}{dx}T(x,x_0)dx$$

$$= \int_0^L \frac{dS}{dx}T(x,x_0)dx \quad (D-1)$$

Similarly, we can solve dS/dx from the measured V and T obtained from the thermal model. dS/dx calculated by the above two methods for the laser annealed sample is shown in Figure D-4. The high degree of consistency between the two methods further proves the methodology of our Seebeck coefficient calculation.

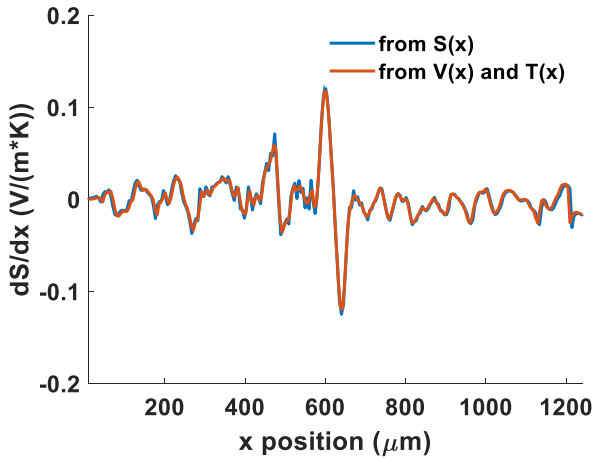

Figure D-4. dS/dx calculated by taking the derivative of $S(x)$ (blue curve) and dS/dx calculated from PTE voltage and thermal model (orange curve) for the laser annealed sample. The two curves overlap each other, validating our methodology.

Appendix E

Simulated temperature profile during the laser annealing

For the laser annealing, the temperature profile cannot be obtained by the thermal model described in Chapter 5 and Appendix C, because the temperature profile largely depends on the laser spot size, which is not considered in our thermal model, when the laser power is high. The temperature profile is obtained by finite element method simulation in COMSOL Multiphysics 6.1. The Si wafer and the silver paste are included and the convection and contact resistance are considered. The simulated temperature is shown in Figure 5-8D. We can see an additional temperature increase near the position of laser spot ($x = 620\ \mu m$) due to the finite laser spot size, as shown in Figure E-1. We want to emphasize that when the laser power is small (in the PTE measurement), the temperature obtained by the thermal model in Chapter 5 and Appendix C is appropriate since the additional peak is small.

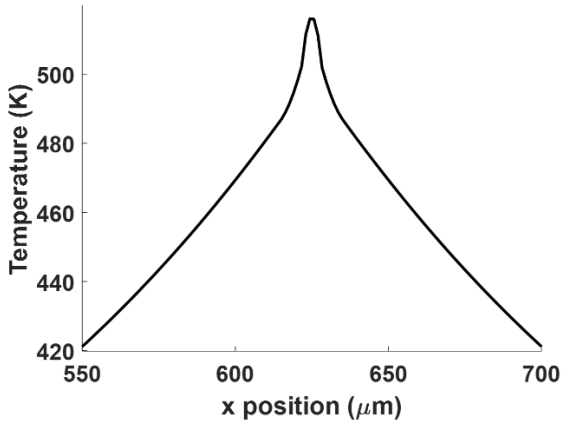

Figure E-1. Simulated temperature profile near the center of the fiber (laser spot) during laser annealing. An additional localized temperature increase near the heating position arises due to the finite laser spot size.

Appendix F

This Appendix describe the optical setups in Natelson lab for a reference for future users.

785 nm setup:

The 785 nm setup is located at the optics room in B11. It shares the optical table with the 1060 nm setup. It is based on a home-build Raman system. The sample is placed in a Montana instrument cryostat with low temperature ability and optical and electrical accessibility. A top view sketch of the 785 nm optical setup is shown in Figure F-1.

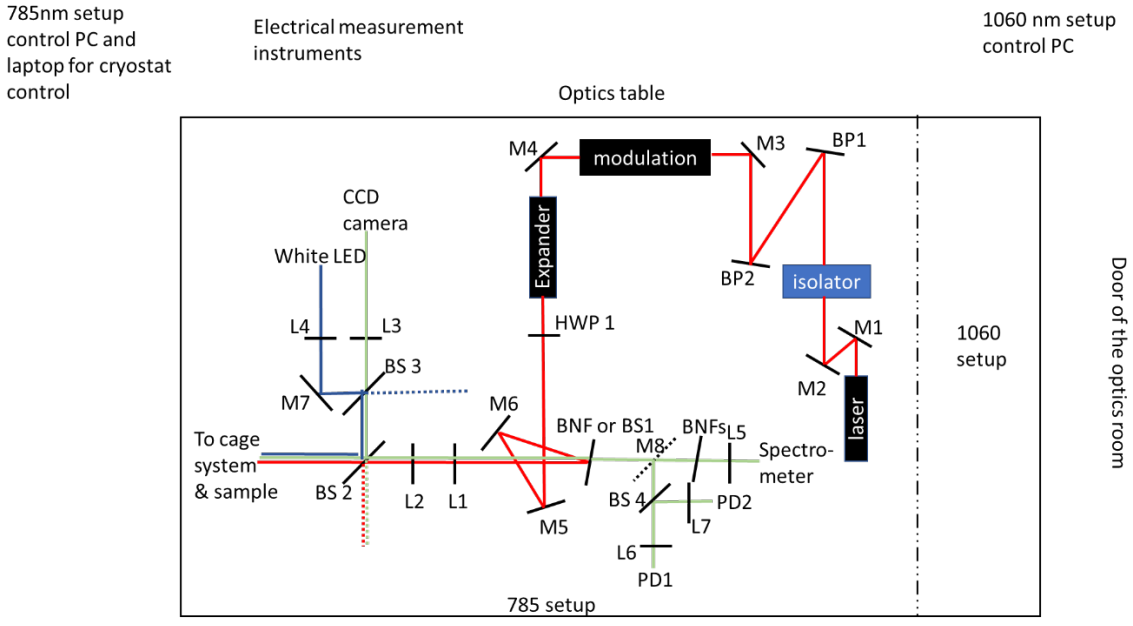

Figure F-1: Top view sketch of the 785 nm optical setup. It shows the relative position of the optical elements.

In Figure F-1, M means mirror; BP means band pass filter; HWP means half wave plate; BNF means Bragg Notch filter; BS means beam splitter; L means lens; PD means photon detector. The red lines are laser beam; the blue lines are white light; the green lines are the outcoming light from the sample. The dashed lines are the beams not used when they are split by BSs.

The laser comes out from a Toptica 785 nm diode laser with output power to be 120 mW. The beam is reflected by M1 and M2, and then goes through the isolator which prevent the back-propagation light entering the laser. The laser is then filtered by BP1 and BP2. For a reference, the laser power after BP2 is about 90 mW if the angles of the BPs are correct. More details about the BPs can be found at: https://optigrate.com/braggrate-bandpass-filter/. Then laser power is controlled in the modulation part, which includes ND filters, optical chopper, HWP and linear polarizer. The polarization of the laser after the modulation is fixed to be perpendicular to the optics table. The laser is expanded by the beam expander and then it can be approximated to be a parallel (collimated) beam. The polarization of the laser is controlled by the following HWP1. The laser is reflected by M6 and M7 and impinge on the BNF or BS1, depending on the needs of the experiments. The laser then goes through L1 and L2. L1 is placed on a 2-axis piezo stage which controls the movement of L1 in the plane perpendicular to the wave vector. The combination of L1 and L2 controls the laser spot position on the sample in the map measurements. If map function is not needed in the measurements (like EL), L1 and L2 can be removed. A white light LED is collimated by L4 and can overlap the laser by adjusting BS2 and

BS3. The laser and the white light enter the cage system and are focused by an objective to the sample. The white light illuminates the sample can help adjust the focus. The outcoming light is split into two parts. One part is focused to the CCD camera, so we can see the image of the sample in real time. Another part back propagates to BNF or BS1. For Raman measurements, we use BNF to block the red laser beam and the rest of the outcoming photons can pass, and there are a set of 3 BNFs in front of the spectrometer to further remove the laser line. More details of the BNF can be found at: https://optigrate.com/braggrate-notch-filter/. In other measurements where laser is needed, we can use either of them. In EL measurements, we use BS1 to make sure the spectra we take is full. In EL measurements, we can even remove BS1 once the alignment is completed and the laser spot position on the sample is known. The outcoming photons then are focused to the spectrometer by L5 for spectrum measurements. We can also measure photon statistics of the light source by placing M8 in the path. Then the photons are split by BS4 and focused to PDs for photon counting measurements.

In sum, EL, PL, Raman (direct and remote), OCPV, plasmonic heating, photon counting measurements can be done using the 785 nm setup. The fundamental electrical measurement, including electromigration, R vs. T and I-V curve, can be done as well considering the electric accessibility of the cryostat and the electrical measurement instruments.

1060 nm setup:

The 1060 nm setup is much simpler and is almost used for the PTE measurements. It can be understood as a simplified version of the 785 setup without spectrum acquisition ability. The sample chamber is in ambient condition with optical and electrical accessibility. The optical setup is shown in Figure F-2.

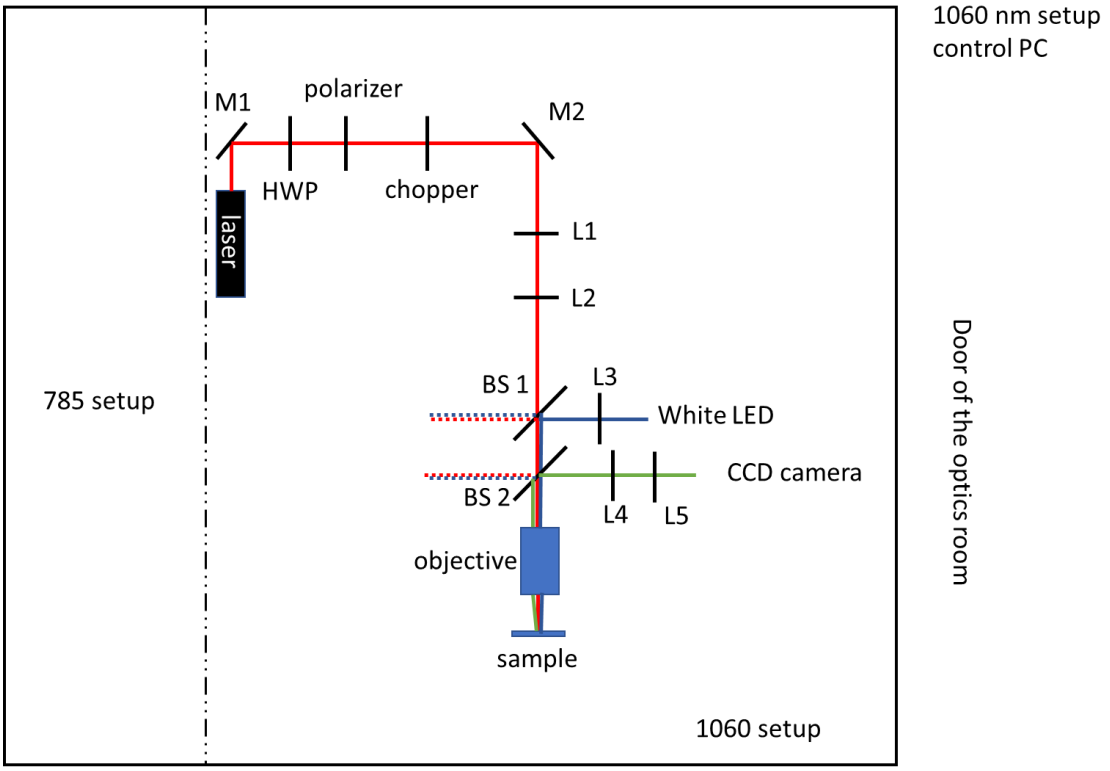

Figure F-2: Top view sketch of the 1060 nm optical setup. It shows the relative position of the optical elements.

The light source is a Newport 1060 nm diode laser with an output power of 100 mW. As described in Chapter 5. The power and polarization of the laser is controlled by a HWP and a polarizer. The laser is then modulated by a chopper. The alignment of the beam is controlled by M1 and M2. L1 and L2 expand the beam and control the collimation. Similar to the 785 nm setup, we have white LED and CCD camera to illuminate the sample and obtain the real-time image of the sample to focusing. The white light and the laser are focused to the sample by an objective. The sample chamber can move in the x, y, and z directions using 3 stepper motors (Figure 5-3).

633 nm setup:

In terms of optical functions, 633 nm setup is a duplicate of the 785 nm setup. The only difference is the excitation wave length, and the 633 nm setup has no photon counting ability. A sketch of the setup is shown in Figure F-3. The modulation part, like the 785 nm setup, includes ND filters, chopper, HWPs and polarizers for power and polarization control. Similarly, L1 and L2 are used for map scans. L1 is placed on a home-build 3-axis stage with stepper motors. BNFs in front of the spectrometer is needed for Raman measurements, and can be removed for other measurements.

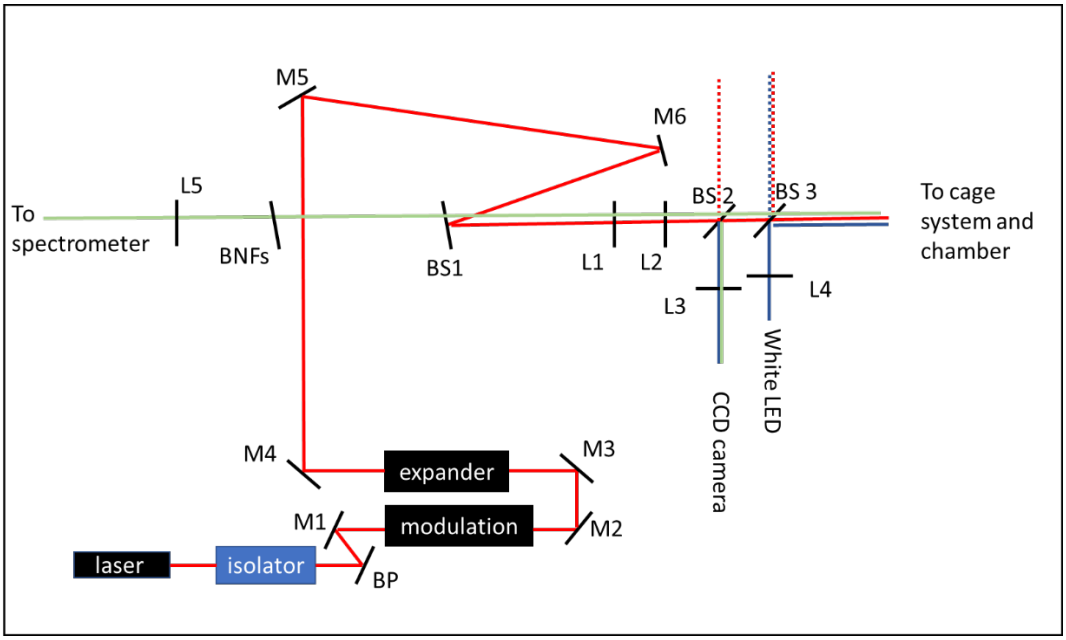

Figure F-3: Top view sketch of the 633 nm optical setup. It shows the relative position of the optical elements.

Appendix G

Transition dipole calculations and extra theoretical discussion

In this section we provide some theory backing the calculation of the transition dipole moments in the main text and give details about the implementation of the quantum calculations used to obtain the transition dipole moments for electron tunneling between electrodes. In what follows, we employ the transfer Hamiltonian formalism applied to the calculation of inelastic tunneling processes[203] (tunneling through photon emission), together with an extension of Macroscopic Quantum Electrodynamics (MQED) developed to describe interactions between arbitrary electronic eigenstates[204,205]. Consider the system under study, in which we have two distinct metallic electrodes. In the transfer Hamiltonian formalism, one considers the separately the electronic eigenstates of each electrode. The transition rate between an eigenstate $\phi_i(\boldsymbol{r})$ on the left electrode and the eigenstate $\phi_j(\boldsymbol{r})$ of the right electrode through emission of a photon of energy $\hbar\omega$ is given by Fermi's Golden rule as

$$\gamma_{i\to j} = \frac{2\pi}{\hbar}\left|\langle j, 1_\omega|\widehat{H}_I|i, 0\rangle\right|^2 \delta\left(\omega - \omega_i + \omega_j\right), \quad (G1)$$

where from the MQED formalism, the light-matter interaction Hamiltonian describing the interaction between some continuum light mode and an electronic transition is given by

$$\hat{H}_I = \hbar \sum_{jk} \int d\omega \, g_{jk}(\omega)[\hat{a}(\omega) + \hat{a}^\dagger(\omega)]\hat{\sigma}_{jk}, \quad (G2)$$

where $\hat{\sigma}_{jk} = \hat{c}_j^\dagger \hat{c}_k$ represents an electronic jump operator between states $k \to j$, and g_{jk} is the light-matter interaction strength between the electronic transition and the light-mode, which can be written as

$$g_{ji}(\omega) = \frac{e}{m}\sqrt{\frac{\hbar\mu_0}{\pi}} \sqrt{\iint d\boldsymbol{r}\, d\boldsymbol{r}' \boldsymbol{d}_{ji}(\boldsymbol{r}) \cdot Im\{\boldsymbol{G}(\boldsymbol{r}, \boldsymbol{r}', \omega)\} \cdot \boldsymbol{d}_{ji}^*(\boldsymbol{r}')}, \quad (G3a)$$

$$d_{ji}(r) = \phi_j^*(r)\nabla\phi_i(r), \quad (G3b)$$

which depends on the Green's Function Dyadic (GF) (containing the optical LDOS) and the transition dipole density, $d_{ji}(r)$, which describes how the electronic transition couples to the optical fields. For transitions localized in scales much smaller than that the variation scale of the fields, the GF can be approximated as constant over the extent of the electronic wavefunctions, and thus the couplings may be simplified to

$$g_{ji}(\omega) = \frac{e}{m}\sqrt{\frac{\hbar\mu_0}{\pi}} \sqrt{\boldsymbol{d}_{ji} \cdot Im\{\boldsymbol{G}(r_0, r_0, \omega)\} \cdot \boldsymbol{d}_{ji}^*}, \quad (G4a)$$

$$\boldsymbol{d}_{ji} = \int d\boldsymbol{r}\, \phi_j^*(\boldsymbol{r})\nabla\phi_i(\boldsymbol{r}), \quad (G4b)$$

which is now very similar to the usual light-matter coupling strength between a point dipole and an optical mode. With this, the rate of inelastic tunneling between states $i \to j$ reads

$$\gamma_{i\to j} = \frac{2e^2\hbar^2\mu_0}{m^2} \int d\omega \left|\boldsymbol{d}_{ji} \cdot Im\{\boldsymbol{G}(r_0, r_0, \omega)\} \cdot \boldsymbol{d}_{ji}^*\right| \delta\left(\omega - \omega_i + \omega_j\right). \quad (G5)$$

This can be cast as the inelastic rate per unit energy as

$$\frac{1}{\hbar}\frac{d\gamma_{i\to j}}{d\omega} = \frac{2e^2\hbar\,\mu_0}{m^2}\left|\boldsymbol{d}_{ji}\cdot Im\{\boldsymbol{G}(r_0,r_0,\omega)\}\cdot\boldsymbol{d}_{ji}^*\right|\delta\left(\omega-\omega_i+\omega_j\right).$$

Finally, to obtain the total inelastic rate per unit energy, we sum over all possible initial and final states by considering their occupation:

$$\frac{1}{\hbar}\frac{d\Gamma}{d\omega} = \frac{\pi\omega}{3\epsilon_0\hbar^2}\sum_{ij}\left|d_{ji}\right|^2\rho_{\boldsymbol{d}_{ji}}(r_0,\omega)\,f(E_i)\left(1-f\left(E_j\right)\right)\delta\left(\omega-\omega_i+\omega_j\right), \qquad (G6)$$

where we have introduced the Fermi factors for the initial and final electrodes, and more importantly, we have defined the partial LDOS in analogy with the case of an ideal point dipole. In our case, this partial LDOS reads:

$$\rho_{\boldsymbol{d}_{ji}}(r_0,\omega) \equiv \frac{6e^2\hbar^3}{\pi\omega\,c^2m^2}\left|\frac{\boldsymbol{d}_{ji}}{\left|d_{ji}\right|}\cdot Im\{\boldsymbol{G}(r_0,r_0,\omega)\}\cdot\frac{\boldsymbol{d}_{ji}^*}{\left|d_{ji}\right|}\right|. \qquad (G7)$$

Note that in the case of only considering a single transition in an isolated quantum emitter, it can be shown that the usual transition dipole moment, $\boldsymbol{\mu}_{ji} \equiv -e\,\langle j|\hat{r}|i\rangle$, can be connected with $\boldsymbol{d}_{ji}$ as[205]: $\boldsymbol{\mu}_{ji} = -\frac{e\hbar}{m\omega_0}\boldsymbol{d}_{ji}$, and then Eq. G6 returns the typical expression for the total decay rate of a quantum emitter of natural frequency ω_0 in presence of some arbitrary LDOS[206].

Eq. G6 represents the main theoretical result of this section. From this expression and relatively simple arguments, one can get an intuition of where the experimentally observed phenomenology originates. Eq. G6 has three main

components: the Fermi factors, describing the electron population of the different eigenstates, the transition dipole amplitudes, and the partial LDOS. On the one hand, the normalization analysis shows that the extracted effective temperature is mostly independent of the applied magnetic field, which rules out the occupation of states and hot electron generation processes as the driving mechanism behind the magnetic field dependence of the EL. On the other hand, as stated in the main text, bulk magneto-optical effects in Au are too small to significantly alter the present optical modes (and the macroscopic Green's function), though nanoscale and quantum contributions cannot be fully excluded. Since similar effects can be measured in aluminum junctions, we can assume that the physics studied here should be well represented within the free electron gas metallic description. To the best of our knowledge, non-local descriptions[207–209] of the optical response of metals have not reported any enhancement of magneto-optic response, and therefore we believe that a better description (within a TDDFT formalism, for instance), wouldn't provide qualitatively different conclusion than our simple classical local modelling.

This points to the role of the transition dipoles as the main mechanism by which the magnetic field may affect the EL signal coming from the system. This can happen in two distinct ways: either by simply modifying the amplitude of the transition dipole moments, or by modifying their direction (or linear/circular character), and thus the projection of the LDOS in the partial LDOS.

In order to explore this, we implement 2d eigenfunction calculations using the Schrödinger equation module included in COMSOL Multiphysics to simulate transition dipole moments in a toy-system modeled after the experimental geometry. In Figure G1a we show examples of different geometries used in these calculations. We generate different tunneling spots with gaps of the order of 1 nm and different degrees of symmetry. The areas used to obtain the eigenstates were chosen to strike a balance between computational time and having enough bound states to describe the tunneling processes. For each geometry, we perform two isolated eigenstate calculations. First, we assign a zero potential to the left electrode, and assign a potential given by the sum of Fermi Energy (E_F) and work function (Φ) to the rest of the simulation domain, which in the case of gold we approximate by 10 eVs. Since the system is biased with a voltage V, we proceed to look for eigenstates, $\phi^{(l)}(\boldsymbol{r})$, that are found around energies of $E_F + eV/2$. In the next step, we assign a zero potential to the right electrode and assign the potential of $E_F + \Phi$ to the rest of the domain. In this case, we look for eigenstates, $\phi^{(r)}(\boldsymbol{r})$, around energies of $E_F - eV/2$. In both cases, to introduce the out of plane magnetic field we include a vector potential that enters the Hamiltonian through the canonical momentum term $\widehat{H} = \left(-i\hbar\nabla - q\vec{A}\right)^2/2m$. In these two simulations, we obtain 500 eigenfunctions for each electrode, which we then use to calculate $2.5 \cdot 10^5$ distinct transition dipoles by following Eq. G4b as $\boldsymbol{d_{ji}} = \int d\boldsymbol{r}\, \left(\phi_j^{(r)}(\boldsymbol{r})\right)^* \nabla\phi_i^{(l)}(\boldsymbol{r})$. Once the transition dipoles are obtained and by expressing them as introduced in the main text $\boldsymbol{d_{ij}} = \left|d_{ij}\right|(\hat{u}_d + i\epsilon_s\, \hat{u}_\perp)/\sqrt{1+\epsilon_s^2}$, we can

characterize them in terms of only two parameters: their transition amplitude, and the ellipticity. Each of these parameters will point at either one of the mechanisms introduced before to explain the magnetic-field dependent EL, i.e. the modification of the transition dipole amplitude, or a modification of the partial LDOS.

In Figure G1b we show the histogram measuring the distribution of dipole moment amplitude in presence and absence of externally applied magnetic field. For all simulated structures, the histograms are identical for positive and negative magnetic field and thus are presented as their average. Interestingly, one can see how for highly symmetric structures, there are a large number of dark transitions (with very small dipole moment) which can be understood as coming from symmetry-derived selection rules. As the magnetic field is introduced, it breaks these symmetries and the transitions become bright. As the system is made more locally-asymmetric, this effect is relaxed, and while one can observe a large shift of the dipole moment statistics in the high symmetry case of Figure G1b1, the distribution barely changes in Figure G1b3. This indicates that in the experimental devices, where metallic boundaries are formed stochastically, there will be few symmetries that the magnetic field can break, and thus the dipole moment statistics are not expected to be greatly modified. Furthermore, as stated above, the distributions for positive and negative magnetic fields are nearly identical, and thus the overall change in dipole moment amplitudes wouldn't explain the difference in measured EL for positive and negative applied magnetic field.

This suggests that the most likely mechanism to explain the modification of the measured EL is a modification of the partial LDOS. To explore this possibility, we construct the histograms introduced in the main text, $C_\mu(B)$, which count the number of transition dipoles with a certain dipole moment and ellipticity. In Figure G1c we show $S = (C_\mu(6\text{ T}) + C_\mu(-6\text{ T}))/2$, which provides a general view of the dipole moment distribution in presence of a magnetic field. We note that although not shown, all transition dipoles calculated in absence of magnetic field are linearly polarized ($\epsilon_s = 0$). This already indicates that while the dipole moment distribution may not be changing dramatically due to the presence of the magnetic field, the transitions involved are acquiring ellipticity, and therefore the projection that is being selected in the partial LDOS is also being modified. Furthermore, in Figure G1d we show $D = (C_\mu(6\text{ T}) - C_\mu(-6\text{ T}))/2$, normalized to S, which shows that the ellipticity distribution of the transition dipoles is not symmetric, and that it is influenced by the external magnetic field. In particular, one may see that for all the different structures, a positive magnetic field leads to more transitions having positive ellipticity, while a negative magnetic field leads to generally more negative ellipticity in the transitions.

These observations, together with the expected presence of a relevant chiral density of optical states in the experimental asymmetric junctions, indicate that (as introduced in the Chapter 4) the role of the magnetic field is to modify the way that the tunneling currents excite the optical modes present in the system by introducing a degree of chirality in the excitation. This effect is then subsequently amplified by

the chiral density of optical states in the asymmetric nanogaps, as shown in Figure 4-17d.

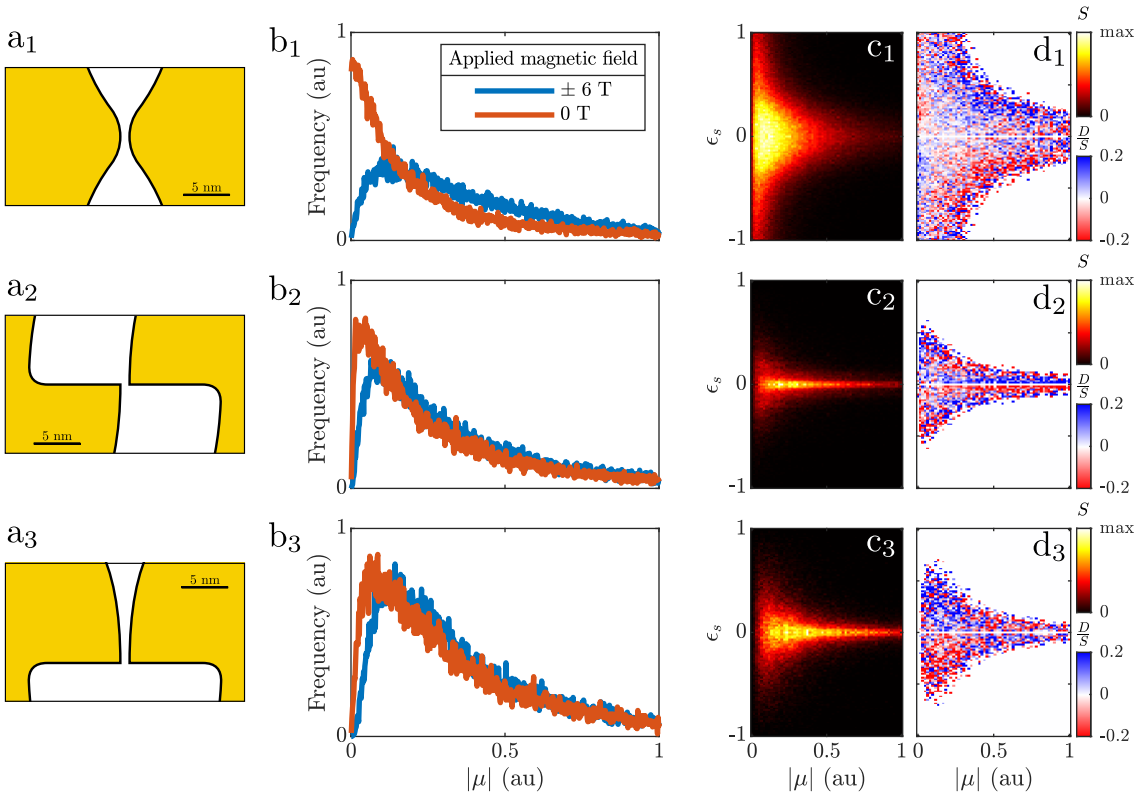

Figure G1: Statistical analysis of transition dipole moments obtained from single particle eigenfunctions. Subindex numbers indicate the particular structure for which quantities are calculated, which we label as fully symmetric (1), fully asymmetric (2) and symmetry broken (3). a Geometries mimicking different tunneling spots in the experimental devices used to calculate the relevant eigenfunctions. Yellow areas indicate the gold sections and white indicate vacuum. b Histogram of the transition dipole moment amplitude in presence and absence of magnetic field. The histograms for magnetic fields of +6 T and -6 T are virtually identical and are presented as their average. c

Average of histograms of the number of dipole moments with certain ellipticity and dipole moment for an externally applied magnetic field of +6 T and -6 T. d Difference of histograms of the number of dipole moments with certain ellipticity and dipole moment for an externally applied magnetic field of +6 T and -6 T, normalized to their average, S.

Appendix H

Full-wave simulation implementation.

In this section we give more details about the implementation of the simulations employed to obtain Figure 4-17d and Figure 4-18. In particular, we use the wave optics module included with COMSOL Multiphysics based on a finite element method frequency domain solver. The geometry under study follows the nominal dimensions of the experimental devices. In Figure H1a we show a 3d view of the geometry employed: a 30 nm thick gold layer (described in our simulations using experimental permittivity measurements[210]) that is lithographically defined into a 120 nm wide and 650 nm long strip that then fans out (at 45º in our simulations) into larger gold contacts. Mimicking the experimental samples, we introduce the break junction at a lateral offset of 190 nm from the strip center, breaking the symmetry of the system. The whole simulation domain is then defined as a 700 nm radius sphere centered at the middle spot of the nanogap, which is set up with a scattering boundary condition. All space surrounding the junction is modelled as vacuum. To simulate the EL process, we introduce irregularities in the junction that mimic the tunneling spots, leaving a minimum distance between the gold surfaces of 14 nm, in accordance with the observed features of the SEM images of the experimental junctions shown in Figure 4-1. The nanogap geometries employed can be observed in Figure H1a, panels b and c, where we show a top-view of the asymmetric and symmetric junctions respectively. Simulating the tunneling current, we introduce point dipoles between

these protrusions in the gap. Instead of exploring every possible dipole orientation and polarization, we exploit the linearity of the fields to determine the power radiated by an arbitrary dipole. To do so, for each geometry, we simulate the fields radiated by a unit linear dipole oscillating in the $\hat{x}$ direction (along the strip), and along the $\hat{y}$ direction. From these fields, $E^{(x)}, H^{(x)}, E^{(y)}$ and $H^{(y)}$(where the superscript denotes the dipole orientation in the simulations) one may then construct the fields radiated by arbitrary point dipoles as

$$\boldsymbol{E} = \mu_x \boldsymbol{E}^{(x)} + \mu_y \boldsymbol{E}^{(y)}, \qquad (H1a)$$

$$\boldsymbol{H} = \mu_x \boldsymbol{H}^{(x)} + \mu_y \boldsymbol{H}^{(y)}, \qquad (H2b)$$

where μ_x and μ_y are the components of the dipole of interest. From this, the radiated powerflow becomes

$$\boldsymbol{S} = \frac{1}{2} Re[\boldsymbol{E} \times \boldsymbol{H}^*] = Re\left[|\mu_x|^2 \boldsymbol{S}_{xx} + \left|\mu_y\right|^2 \boldsymbol{S}_{yy} + \mu_x \mu_y^* \boldsymbol{S}_{xy} + \mu_y \mu_x^* \boldsymbol{S}_{yx}\right], \qquad (H3)$$

where we have introduced the cross-term power flow $\boldsymbol{S}_{ij} \equiv \frac{1}{2}\left[\boldsymbol{E}^{(i)} \times \boldsymbol{H}^{(j)^*}\right]$. By integrating these quantities over some measurement surface (in our simulations, a spherical cap that covers up to 40 degrees from the vertical direction), from two spectra, one may obtain the radiated power for arbitrary in-plane dipoles. In our case, we parametrize these dipoles as introduced in the main text:

$$\boldsymbol{\mu} = |\mu| \frac{(\hat{u}_\mu + i\epsilon_s \hat{u}_\perp)}{\sqrt{1+\epsilon_s^2}}, \qquad (H1a)$$

where in this expression, $\hat{u}_\mu \equiv \cos(\theta)\,\hat{x} + \sin(\theta)\,\hat{y}$ gives the dipole orientation in the linear limit ($\epsilon_s = 0$), and $\hat{u}_\perp \equiv -\sin(\theta)\,\hat{x} + \cos(\theta)\,\hat{y}$ introduces the ellipticity in the local orthogonal axis.

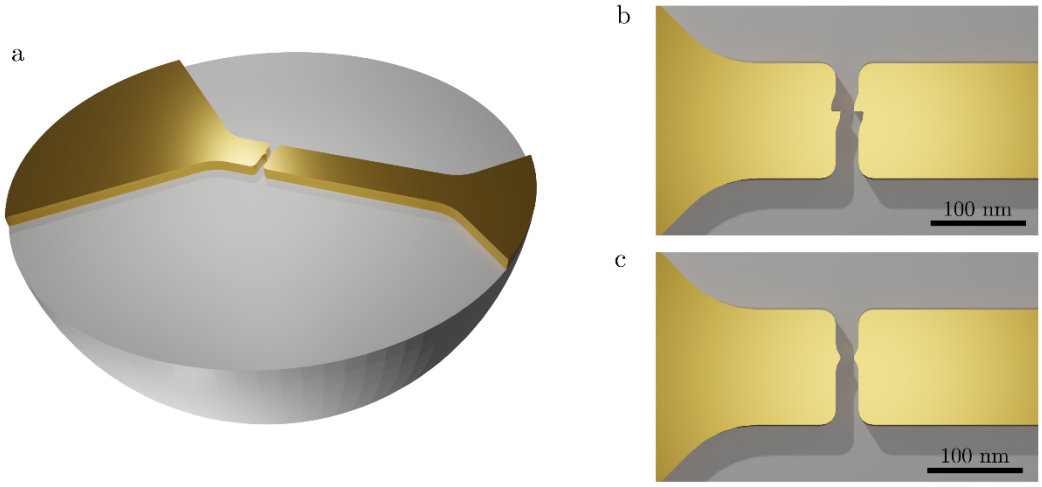

Figure H1. Rendering of the geometry employed in the full-wave numerical simulations. a, 3d view of the simulation domain including the gold junction and the air substrate. The top air half-space has been removed for visualization purposes. b, close-up of the asymmetric junction used to obtain Figure 4-17d in the main text. c, close-up of the symmetric junction employed to obtain the results in Figure 4-18.